ABSTRACT

Title of Dissertation:	MODIFYING DNA CRYSTALS FOR NANOTECHNOLOGICAL APPLICATIONS
	Diana Zhang, Doctor of Philosophy, 2018.
Dissertation Directed By:	Dr. Paul Paukstelis, Associate Professor, Department of Chemistry and Biochemistry.

DNA's programmable nature and ability to self-assemble provides a powerful tool for the construction of complex nanostructures. The initial goal of the field was to use DNA to construct a continuous 3D DNA periodic lattice or crystal. The ultimate aim of the lattice structure would be to act as scaffold for the strategic placement of guest molecules such as macromolecules for structure determination using X-ray. Since that initial vision, the incorporation of guest molecules in DNA nanostructures has expanded to other applications such as cellular imaging, light-harvesting and drug delivery. However, there are several limitations to utilizing DNA crystals for these types of applications. They require relatively high cation concentrations to crystallize and often have low thermal stability. Additionally, crystals generally take on only one shape, or morphology, which can limit their uses in applications.

Our laboratory studies a 13-mer DNA oligonucleotide that self-assembles into crystals upon the addition of magnesium. I demonstrated that by treating these DNA crystals with a chemical crosslinker and depositing polydopamine on the crystal surface,

we increased the overall durability of the crystals. Additionally, we modulated the morphology of the crystal without changing the underlying framework by designing crystal habit modifiers based on the known crystal structure and were able to predictably control the morphology of the overall crystal. This enhanced durability has allowed us to begin testing new applications for DNA crystals. I have explored the incorporation of doxorubicin into the stabilized DNA crystals as a potential form of a new drug delivery device. Together, this work significantly advanced several key areas necessary to diversify the capability of DNA crystals for nanotechnological applications.

MODIFYING DNA CRYSTALS FOR NANOTECHNOLOGICAL APPLICATIONS

by

Diana Zhang

Dissertation submitted to the Faculty of the Graduate School of the
University of Maryland, College Park, in partial fulfillment
of the requirements for the degree of
Doctor of Philosophy
2018

Advisory Committee:
Professor Paul Paukstelis, Chair
Professor Kwaku Dayie
Professor Jason Kahn
Professor Nicole LaRonde-LeBlanc
Professor Isabel Lloyd, Dean's representative

© Copyright by
Diana Zhang
2018

Dedication

I dedicate my thesis to my loving and supporting husband William for always providing me mental stability, and to my developing, unborn child who has kept me company the most through my dissertation process. I would also like to dedicate my thesis to my family who has supported me through my education.

Acknowledgements

I wish to thank Dr. Paul Paukstelis for his mentorship and time. I would not have progressed as much as I would have without your advice and dedication to my work. I also wish to thank my committee members, Dr. Jason Kahn, Dr. Nichole LaRonde-LeBlanc and Dr. Kwaku Dayie and Dean's representative, Isabel Lloyd, for their guidance and time. Additionally, I wish to thank Dr. Kahn, Dr. LaRonde-LeBlanc, Dr. Dayie, Dr. Fushman, Dr. Beaven, Dr. Davis, Dr. Isaacs and their labs for providing support with my research. Lastly, I wish to thank my classmates, and past and present lab members, Sitara, Hyeyeon, Dulith, Adam, Bill, Mello, Maithili, Katherine, Alessandra, Ron, and Betty for making graduate school an enjoyable experience.

The work presented in this document is adapted from the following research articles:

- Enhancing DNA Crystal Durability through Chemical Crosslinking.
  Diana Zhang & Paul J. Paukstelis
  ChemBioChem. 2016 June 16. doi:1002/cbic.201500610.
- Designed DNA Crystal Habit Modifiers.
  Diana Zhang & Paul J. Paukstelis
  Journal of the American Chemical Society. 2017 February 8.
  doi:10.1021/jacs.6b12528.

Table of Contents

Dedication ii
Acknowledgements iii
Table of Contents iv
List of Figures vii
List of Abbreviations ix
Chapter 1: Introduction 1
Chapter 2: Enhancing Durability of Three Dimensional Crystals Using Chemical Crosslinker 7
Chapter 2.1: Introduction 7
Chapter 2.2: Results and Discussion 9
Chapter 2.2.1: Nornitrogen mustard forms interstrand crosslinks within the DNA crystal 9
Chapter 2.2.2: Crosslinking enhances crystal thermal stability 11
Chapter 2.2.3: Crosslinking decreases cation dependence 13
Chapter 2.2.4: Crosslinking provides resistance to DNase I and enhances stability in cell culture media 15
Chapter 2.2.5: G13 is involved in the formation of dimeric crosslinked species 17
Chapter 2.2.6: G13 enhances crystal crosslinking and is required for increased thermal stability. 20
Chapter 2.3: Conclusion 22
Chapter 2.4: Materials and Methods 22
Chapter 2.4.1: Oligonucleotide synthesis, purification and crystallization 22
Chapter 2.4.2: Crosslinking and gel analysis 23
Chapter 2.4.3: Crystal stability measurements 23
Chapter 2.4.4: Piperidine cleavage 24
Chapter 2.4.5: Gel purification of crosslinked species 25
Chapter 3: Enhancing Durability of Three Dimensional Crystals Using Polydopamine 26
Chapter 3.1: Introduction 26
Chapter 3.2: Results and Discussion 29
Chapter 3.2.1: Evaluating polydopamine formation 29
Chapter 3.2.2: Polydopamine coat formation on 13mer crystal. 31
Chapter 3.2.3: Stability of polydaopmine-coated crystals at low magnesium concentration 33
Chapter 3.2.4: Thermal stability of polydopamine-coated crystals 36
Chapter 3.3: Conclusion 37

Chapter 3.4: Materials and Methods 38
Chapter 3.4.1: Oligonucleotide synthesis and purification 38
Chapter 3.4.2: Crystallization 38
Chapter 3.4.3: Polydopamine formation 38
Chapter 3.4.4: Polydopamine deposition on crystals 38
Chapter 3.4.5: Crystal stability measurements 39
Chapter 4: Incorporation of Doxorubicin in 3D DNA Crystals 41
Chapter 4.1: Introduction 41
Chapter 4.2: Results and Discussion 43
Chapter 4.2.1: Incorporation of doxorubicin into 13mer crystals at room temperature 43
Chapter 4.2.2: Incorporation of DOX into 13mer crystals at 4˚C 45
Chapter 4.2.3: Effect of magnesium on doxorubicin in corporation 48
Chapter 4.2.4: Loading capacity and retention of doxorubicin inside 13-mer crystal 50
Chapter 4.2.5: Layer-by-layer assembly on doxorubicin-incorporated crystals 55
Chapter 4.4: Materials and Methods 59
Chapter 4.4.1: Oligonucleotide synthesis and purification 59
Chapter 4.4.2: Crystallization 59
Chapter 4.4.3: Incorporation of DOX 60
Chapter 4.4.4: Layer-by-layer assembly 60
Chapter 4.4.5: Dopamine Polymerization on DOX crystals 60
Chapter 4.4.6: Visualization and measurements 60
Chapter 4.4.7: Fluorimeter measurements 61
Chapter 5: Designed DNA Crystal Habit Modifiers 62
Chapter 5.1: Introduction 62
Chapter 5.2: Results and Discussion 64
Chapter 5.2.1: Crystallization of 13-mer with poison oligomers 64
Chapter 5.2.2: X-ray diffraction showed poison oligomers are only habit modifiers 71
Chapter 5.2.3: Incorporation of poison oligomers 72
Chapter 5.2.4: Thermal stability of poison crystals 75
Chapter 5.2.5: Layer-by-layer assembly with poison oligomers 77
Chapter 5.4: Materials and Methods 81
Chapter: 5.4.1: Oligonucleotide synthesis and purification 81

Chapter 5.4.2: Crystallization 81
Chapter 5.4.3: Macroseed layer growth 81
Chapter 5.4.4: Visualization and measurements 82
Chapter 5.4.5: Crystal radiolabeling 82
Chapter 6: Conclusion and Future Work 83
Bibliography 87

List of Figures

Figure 1.1. A model 3D DNA crystal. 3
Figure 2.1. Nornitrogen chemical crosslinking mechanism between two guanines. 7
Figure 2.2. Incomplete nornitrogen bialkylation 8
Figure 2.3. Polyacrylamide gel analysis of crosslinked crystals 10
Figure 2.4. Electron density of NOR-treated crystals 11
Figure 2.5. NOR-treatment enhances crystal thermal stability. 12
Figure 2.6. Crystal dissolution at elevated temperature 13
Figure 2.7. Crosslinking decreases divalent cation requirements 14
Figure 2.8. NOR-treatment enhances nuclease resistance and longevity in tissue culture medium. 16
Figure 2.9. Comparison of treated and untreated crystals in FBS + 10 mM Mg^{2+} 17
Figure 2.10. G13 is a primary site for NOR-crosslinking 19
Figure 2.11. Dimeric crosslinked species is intact prior to piperidine cleavage 20
Figure 2.12. G13 is necessary for efficient crosslinking and enhanced thermal stability. 21
Figure 3.1. Pathways for dopamine polymerization. 27
Figure 3.2. Schematic of metal complexations between catechol and group two metals 28
Figure 3.3. Polydopamine (PDA) formation measured at OD 600 31
Figure 3.4. Polydopamine (PDA) coat on 13-mer crystal 32
Figure 3.5. Acrylamide gel of PDA-coated 13-mer crystals 32
Figure 3.6. Stability of PDA-coated crystals in 10 mM magnesium formate 34
Figure 3.7. Stability of crystals with PDA coat formation at 22˚C incubated at 30˚C. 34
Figure 3.8. Stability of PDA-coated crystals at 37˚C 35
Figure 4.1. Structure of doxorubicin and anthraquinone 44
Figure 4.2. Light microscope images of crystals soaked in DOX at room temperature 44
Figure 4.3. Light microscope images of crystals soaked in DOX at 4˚C 47
Figure 4.4. Light microscope images of gel and non-gel crystals 48
Figure 4.5. Effect of magnesium on formation of gel crystals 49
Figure 4.6. Confocal microscopy images of non-gel crystals 51

Figure 4.7. Confocal microscopy of DOX diffusion of non-gel crystals 52
Figure 4.8. Confocal microscopy images (Z-stack) of NOR-treated gel crystals 53
Figure 4.9. Fluorimeter measurement of DOX-incorporated crystals. 53
Figure 4.10. Measurement of DOX diffusion out of ~25 gel crystals over time 55
Figure 4.11. Layer-by-layer assembly on non-gel crystals 56
Figure 4.12. Layer-by-layer assembly on gel crystals. 57
Figure 4.13. Retention of DOX in PDA coated crystals over time 58
Figure 5.1. Sequences of oligonucleotides used. 63
Figure 5.2. Relative orientations of the duplexes segments and noncanonical base pairs in the 13-mer crystal. 63
Figure 5.3. Poison oligomers as crystal habit modifiers 66
Figure 5.4. Light microscope images of 13-mer crystals grown in the presence of both Δ5' and Δ3' 67
Figure 5.5. Light microscope images of 13-mer crystallized in the presence of 13-mer-G1A and 13-mer-G1C 67
Figure 5.6. Habit modification and cross-reactivity of poison oligomers 69
Figure 5.7. Light microscope images of 13-mer crystallized with 11-mer 71
Figure 5.8. Diffraction images 72
Figure 5.9. Polyacrylamide gel analysis of B7 poison crystals 73
Figure 5.10. Polyacrylamide gel analysis of B6 poison crystals 74
Figure 5.11. Polyacrylamide gel analysis of non-poison hexagonal unipyramid crystals soaked in poison oligomers 74
Figure 5.12. Thermal stability poison of B7 and B6 poison tabular and acicular crystals at 33˚C. 76
Figure 5.13. Theoretical crystal volumes (V), surface area (SA) and SA to Volume ratio 77
Figure 5.14. Poison oligmers function as habit modifiers during crystal growth. 13-mer crystal macroseeds were grown in the absence of habit modifiers 78
Figure 5.15. Light microscope images of crystals layered in the presence of Δ3' 79
Figure 5.16 Habit-modified crystals as macroseeds. 80

List of Abbreviations

Δ5’	Truncated 5’ end
Δ3’	Truncated 3’ end
CL	Crosslinking
FBS	Fetal bovine serum
DHI	5,6-dihydroxyindole
DMEM	Dulbecco's Modified Eagle Medium
DMS	Dimethyl sulfide
DOPA	3,4-dihydroxy-L-phenylalanine
DOX	Doxorubicin
LbL	Layer-by-Layer
NaCaCo	Sodium Cacodylate
NOR	Nornitrogen mustard
PDA	Polymerized dopamine

Chapter 1: Introduction

DNA has become one of the most widely used biomolecules for programmed self-assembly at the nanoscale[1]. The features that make DNA an ideal template for genetic storage make it suitable as a building material for the construction of nanostructures. First, the B-form DNA duplex has consistent structural features with a diameter of 2 nm, a helical pitch of 3.4 nm, and a persistence length of 50 nm or ~150 bp[2]. Second, the hydrogen bonds that contribute to the formation and maintenance of the DNA duplex in vivo allow DNA to self-assemble in vitro. Lastly, the predictable G-C and A-T base pair that encodes the hereditary information is a valuable feature in designing and predicting DNA nanostructures. The ability for self-complementary DNAs to base pair into predictable structures have allowed the creation of a wide variety of nanoscale DNA objects in two and three dimensions[3–17].

The field of DNA nanotechnology proliferated due to the favorable self-complementary features of DNA, and the low cost and facile synthesis of DNA oligomers[18]. As a result, there was a surge in the quantity and diversity of DNA nanostructures generated. The structures ranged from discrete 2D and 3D dimensional structures to continuous, periodic DNA arrays. The general classes of DNA nanostructures include: 2D DNA tile arrays assembled from crossovers and sticky ends[5] , discrete 3D structures utilizes sticky ends for branching[3], DNA origami assembled by folding a kilobase size strand using small staple stands[7] , DNA bricks self-assembled using 32 nucleotide lego-like blocks [16], DNA hydrogels[19], and lastly DNA crystals[17,20]. The diverse DNA nanostructures generated have enabled potential expansion of different types of applications. DNA nanostructures are being developed as photonic networks for energy transfer [21], biosensors[22], templates for lipid bilayer formation[23], drug delivery[24,25], biocatalysts[26] and molecular sieves[27]. DNA is no longer associated purely with the field of

biology as a genetic material, but has entered into the field of material science as a nano-building block.

The earliest goal of the DNA nanotechnology field was the creation of 3D DNA crystals for use as macromolecular scaffolds[28]. The purpose was to aid in structure determination using X-ray diffraction by bypassing the time-consuming step of crystallizing the macromolecule. 3D DNA crystals would ideally be able to act as scaffolds to strategically place and align macromolecules. The macromolecules would then be held in place with limited mobility and therefore be integrated as part of the crystal lattice. To date, there are currently two main 3D DNA crystal designs that have been determined by X-ray diffraction and have been used as scaffolds for guest molecules: the non-canonical crystals[20], first described by Dr. Paukstelis, and the tensegrity triangle[17]. Both designs have solvent channels running throughout the crystals that permit the incorporation of guest molecules. Though the use of DNA crystals as molecular scaffolds for the structure determination of proteins has yet to be achieved, the tensegrity triangle has been used for the organization of fluorescent dye [29], and the non-canonical crystals have been used as macromolecular sieves for proteins [27] and as containers for enzyme catalysis [26,30].

The non-canonical DNA crystal is composed of a 13 nucleotide oligonucleotide, d($G_1G_2A_3C_4A_5G_6C_7T_8G_9G_{10}G_{11}A_{12}G_{13}$), that self-assembles in the presence of divalent cations to form hexagonal unipyramidal crystals [20,31]. Interactions between 13-mers occur in two regions of base pairing: a B-form duplex between C_4-G_9 of two strands, and a parallel-stranded noncanonical motif between G_1-A_3 and G_{10}-A_{12} of two other strands (Figure 1.1A). Previous studies suggested that the Crick-Watson pairing between C_4-G_9 occurs only upon the addition of divalent cations, and the assembly into higher molecular complexes facilitated by the noncanonical pairs also occurrs rapidly after Mg^{2+} addition[31]. G13 is the only nucleotide in the

crystal structure that does not form base pairing interactions, and it is disordered in all of the crystal structures we have solved. G13 is not necessary for crystallization, and its apparent disorder is due in part to its positioning within a series of solvent channels that run through the crystal. These solvent channels run parallel and perpendicular to the six-fold symmetry axis within the crystal, and make it possible to add additional nucleotides and other groups to the 3' end of the oligonucleotides without disrupting crystallization[31] (Figure 1.1B).

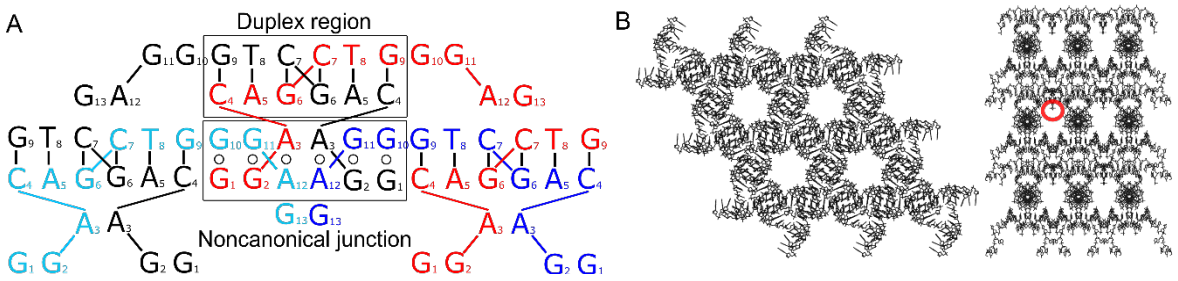

Figure 1.1. A model 3D DNA crystal. **A**. Secondary structure interactions formed from crystallographically identical DNA 13-mers. Four strands are colored differently to highlight Watson-Crick interactions in the helical region, and non-canonical base pairs in the interlayer junction region. **B.** The interactions between 13-mers results in a crystal lattice that contains solvent channels that run through the length of the crystal both parallel to (left) and perpendicular to the six-fold symmetry axis (right). The G13 phosphates from two strands are circled in red, showing that these nucleotides are adjacent to one another and oriented into the solvent channels.

The crystal lattice formed by the 13-mer is not limited to the sequence described in Figure 1.1A. Variants referred to collectively as complementary versions of the 13-mer oligonucleotide contain sequences changes made to the B-form duplex region. A screen was generated of all possible self-complementary B-form duplex sequences and some of these complementary oligonucleotides crystallized into the same crystal lattice structure as the 13-mer. The sequence changes largely play a role in crystallization speed. Different complementary oligonucleotides mixed together form a heterogeneous crystal. In order for the heterogeneous crystal to form, the B-form duplex region forms first with the proper Crick-Watson base pairing,

and then propagation of the B-form duplex regions would take place using the non-canonical region[31].

The ability of the 13-mer to propagate crystallization in the presence of divalent cations also allows these crystals to undergo layer-by-layer assembly. Crystal macroseeds are able to resume crystal growth when incubated with newly added DNA 13-mer oligonucleotides. These oligonucleotides self-assemble a new shell layer around the crystal core to create a core-shell crystal[30]. The oligonucleotides in either the core or the shell can be functionalized with a variety of molecules. The growth of a new layer on the 13-mer crystal has been shown with the incorporation of oligonucleotides functionalized with a fluorescent guest molecule, creating a fluorescent layer. The ability to incorporate oligonucleotide with different functionalization group at each layer allows opportunities for creating multifunctional biomaterials.

DNA crystals and other nucleic acid based architectures have several potential limitations for their use in nanotechnological applications. First, most DNA constructs are composed of relatively short DNA duplexes that are prone to thermal denaturation. While no studies have systematically examined thermal stability of DNA crystals, a number of studies of DNA tile and origami architectures have found that thermal denaturation in solution depends on a number of factors, including average duplex length, geometry, and crossover density[32,33]. Further, because DNA is polyanionic, most DNA crystals require relatively high concentrations of monovalent and/or divalent cations for crystallization and post-crystallization stability[17,20,31]. The high cation concentration may also limit potential applications if accessory or guest molecules are not compatible with these cation concentration. Finally, DNA crystals must be resistant to nucleases present in cellular environments or serum to be useful as delivery vehicles or for *in vivo* sensor and diagnostic applications.

Another limitation is a significant portion of the DNA crystal design field has been focused on altering and understanding properties in existing designs[29,31,34], or identifying new DNA motifs to expand structural diversity[35,36]. Inherently, these approaches interrogate the nanoscale properties of the crystals in the form of intermolecular contacts that enable crystallization. Significantly, very little has been done to control macroscopic properties of existing DNA crystals. One of the fundamental macroscopic properties of crystals are their morphologies, or crystal habits. Morphology plays an important role in nano-bio interactions; the morphology of a drug delivery device can influence distribution and uptake[37]. The ability to modulate the final morphology of crystals has the potential to diversify 3D DNA crystal applications by offering a customizable feature to the design process.

The main goal of my research had been to address limitations of DNA crystals in order to increase the viability for downstream applications. We enhanced the durability of the 13-mer crystal using nonspecific chemical cross-linkers to form inter-strand cross-links[38]. Additionally, we also improved the durability of the 13-mer crystal via the formation of polymerized dopamine (PDA)-coat on the surface of the crystal. As a result, the 13-mer's thermal stability was increased, it was stable at low magnesium concentration (<10 mM) and its half-life in a biological condition was increased. We addressed the static morphology of the 13-mer by adding "poisons" to the crystallizing conditions that hinder the growth of the crystals in specific directions. The poisons were truncated versions of the 13-mer that we designed and we were able to use them to predictably control the morphology [39]. The work that has been done to improve the 13-mer for downstream application has increased the half-life of the crystals in the presence of guest molecules such as doxorubicin (DOX). DOX is commonly used to test the efficiency of

drug delivery devices into cells or animals models. Other DNA nanostructures have incorporated doxorubicin via intercalation[40,41], and now we can add DNA crystals onto this list.

Even though the idea of DNA crystals started the DNA nanotechnology field, 3D crystals are relatively new arrivals that have not been extensively explored. My research centers on expanding the utility of 3D DNA crystals by focusing on how to improve the infrastructure through enhancing the durability and modulating the morphology. The methods utilized here can be applied to other DNA crystals or DNA nanostructures to facilitate and expand downstream applications.

Chapter 2: Enhancing Durability of Three Dimensional Crystals Using Chemical Crosslinker

*This chapter is derived from "Zhang, D. & Paukstelis, P. J. Enhancing DNA Crystal Durability through Chemical Crosslinking. *ChemBioChem* **17,** 1163–1170 (2016)."

Chapter 2.1: Introduction

The ability of a structure to maintain its stability at least until it can carry out its purpose is an important aspect of any engineering process. Data collection for macromolecular crystals is most often performed at cryogenic temperatures to minimize radiation damage, however, the initial cooling process can lead to lattice disorder that negatively impacts diffraction. Chemical crosslinking has been used as a general strategy to improve the stability of protein crystals[42,43]. In a number of cases, non-specific glutaraldehyde crosslinking has been successfully employed to generate covalent bonds between neighboring proteins that allow the crystal to resist changes in temperature or solution conditions to improve diffraction[44]. Similarly, photo-crosslinking has been used to enhance the thermal stability of DNA origami constructs[45,] while site-specific formation of DNA catenanes using specialized oligonucleotides have been successfully used to enhance the stability of DNA origami structures[46].

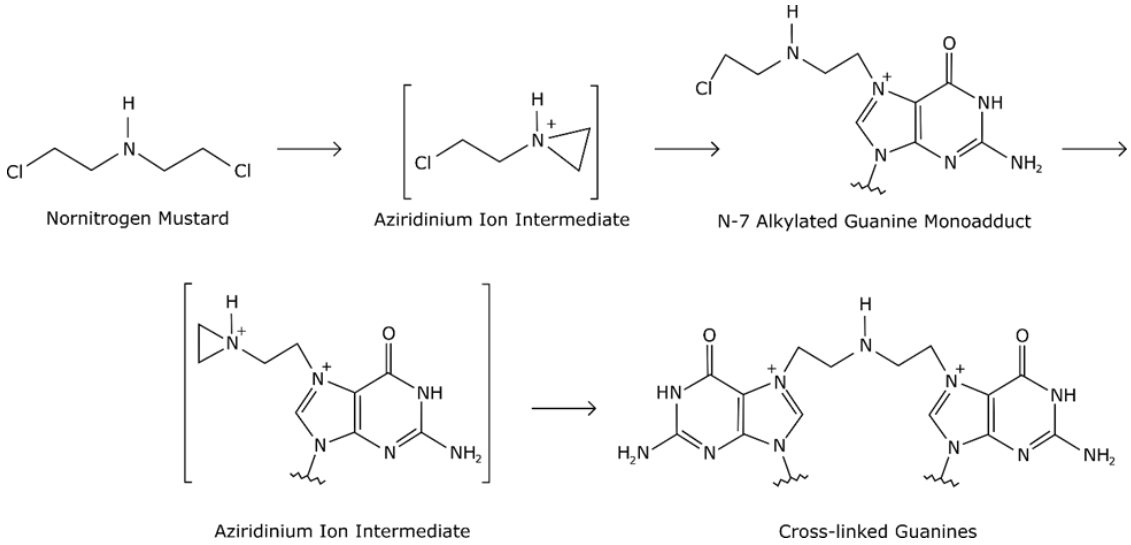

Figure 2.1. Nornitrogen mustard chemical crosslinking mechanism between two guanines.

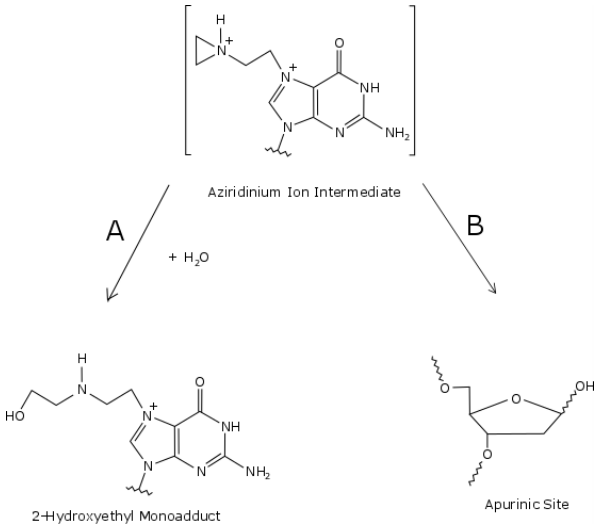

Figure 2.2. Incomplete nornitrogen bialkylation. **A.** The aziridinium intermediate reacts with water. **B.** Depurination of guanine due to instability of alkylated guanine.

Bis(2-chloroethyl)amine (nornitrogen mustard; NOR) is a DNA alkylating agent capable of interstrand crosslinking[47,48]. It is the primary active agent in cyclophosphamide, and like other nitrogen mustards, it preferentially alkylates the N7 position of purines, with guanosine having a higher crosslinking efficiency than adenosine[47,49–51]. With two functional groups capable of going through the aziridinium intermediate, NOR reactivity can result in mono- or dialkylation, with the latter potentially leading to intra- or interstrand crosslinks (Figure 2.1). NOR has a limited half-life in aqueous solution, estimated to be on the order of minutes[52], due to reactivity in water to form bis(2-hydroxyethyl)amine (Figure 2.2). To our knowledge, the interstrand crosslinking potential of NOR or other nitrogen mustards within DNA crystals has not been examined.

The 13-mer crystal was an ideal candidate to test NOR crosslinking. The parallel-stranded non-canonical motif of the (Figure 1.1 A) provides a rich source of purines in close proximity to one another to improve chances for dialkylation. Additionally, this is a region where the different helical layers interact in the crystals. G13 is an additional site that can be alkylated. It does not form any base-pair interaction within the crystal lattice and is positioned within the

solvent channel. Therefore, it is flexible and has the mobility to interact with other purines in close proximity, including another G13 nucleotide.

My work demonstrates that chemical crosslinking of these DNA crystals with NOR results in their increased thermal stability, decreased cation dependence, and reduced nuclease sensitivity. Gel electrophoresis of crosslinked crystals suggests that crosslinking can occur at several sites, leading to multiple crosslinked species. We mapped the crosslinking site in the most abundant of these species and found that the unpaired G13 residue appears to be a primary crosslinking site. We further demonstrate that higher-molecular weight crosslinks are decreased in crystals that lack G13, and that the G13 crosslinks are required for enhancing crystal thermal stability. This chemical crosslinking strategy may be broadly applicable to all types of DNA architectures.

Chapter 2.2: Results and Discussion

Chapter 2.2.1: Nornitrogen mustard forms interstrand crosslinks within the DNA crystal

Gel electrophoresis of dissolved crystals following incubation with NOR at 4 clearly demonstrated interstrand crosslinking within the crystals. This was judged by the presence of higher molecular weight bands relative to the uncrosslinked control in both radioloabeled and non-radiolabeled samples (Figure 2.3). Up to four higher molecular weight products were observed, along with one species with slightly lower electrophoretic mobility than the uncrosslinked control that is presumably the result of DNA alkylation events that do not lead to interstrand crosslinks. Furthermore, the number of higher molecular weight bands was directly correlated to the NOR concentration (Figure 2.3C). Crosslinking efficiency measured by densitometry of SYBR Gold showed up to ~60% of the product was present in the dimeric, trimeric, and tetrameric species (Figure 2.3A). Over multiple experiments we observed higher apparent crosslinking efficiency when samples were stained (Figure 2.3A) than when radiolabeled (Figure 2.3B). Though the

reason for this is not entirely clear, it is possible that crosslinks at positions near the 5' end leads to decreased labeling efficiency through inhibition of the kinase reaction, similar to observations for other 5'-protected DNAs[53]. Because of the short half-life of NOR in solution, we performed two sequential treatments to achieve the best overall crosslinking efficiency at 4°C (Figure 2.3 A, B).

Crystals that had undergone the crosslinking procedure were also subjected to x-ray diffraction, using the same cryoprotection methods as previously described[31]. The unit cell parameters, space group, and diffraction limits were nearly identical to the previously determined crystal structure. Electron density maps showed minimal differences. There was additional electron density associated with the N7 position of G9 and G10 (Figure 2.4). This may be the result of alkylation events, though the density was not sufficient to model. Importantly, these results indicated that crosslinking did not disrupt or change the overall crystal structure.

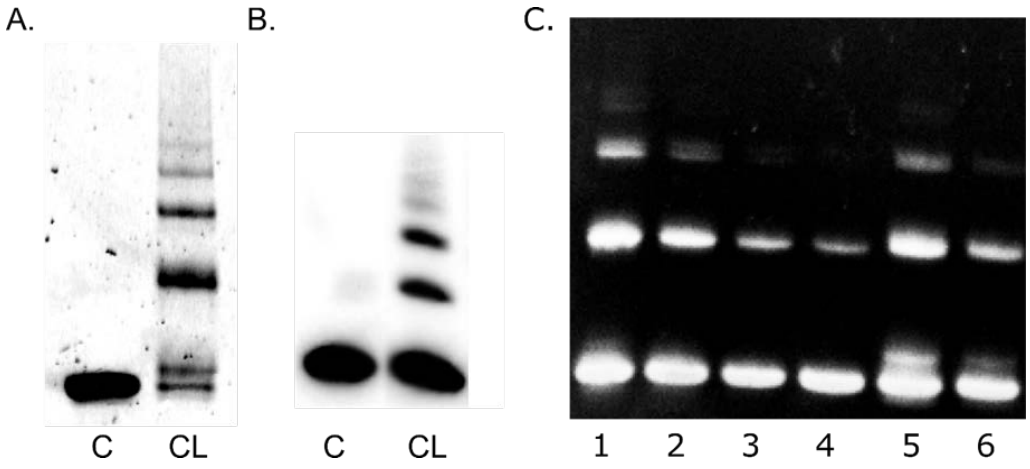

Figure 2.3. Polyacrylamide gel analysis of crosslinked crystals. Control 13-mer (C) and NOR-treated 13-mer crystal (CL) stained with **A.** SYBR Gold, or **B.** after 5' ^{32}P radiolabeling. SYBR staining consistently showed higher apparent crosslinking efficiency than radiolabeling. **C.** SYBR Gold stain of 13-mer crystal (CL) treated with Lane 1, 250 mM NOR at 4˚C; Lane 2, 100 mM NOR at 4˚C; Lane 3, 50 mM NOR at 4˚C; Lane 4, 25 mM NOR at 4˚C; Lane 5, 50 mM NOR at 22˚C; Lane 6, 25 mM NOR at 22˚C.

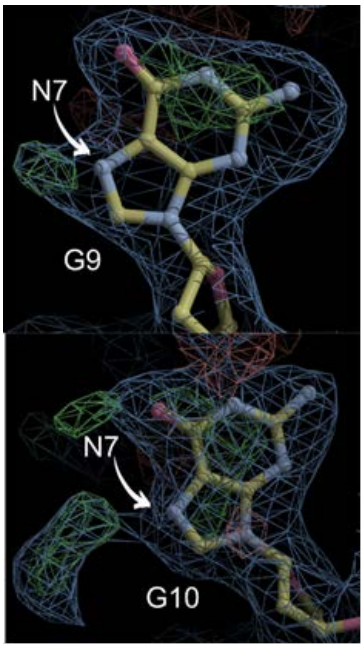

Figure 2.4. Electron density of NOR-treated crystals. Sigma-A-weighted $2F_o$-F_c (blue; 1 σ contour) and F_o-F_c (green/red; 2 σ contour) electron density associated with nucleotides G9 and G10. These were the only two nucleotide positions that showed additional electron density relative to the untreated crystals.

Chapter 2.2.2: Crosslinking enhances crystal thermal stability

We first examined how the crosslinking procedure impacted the thermal stability of the crystal by determining dissolution temperatures based on UV absorption. Each dissolution experiment used at least 15 crystals in a single cuvette to ensure sufficient signal. We confirmed that all crystals sank to the bottom of the cuvette and were out of the direct light path. The average dissolution temperature for the control samples was 41.1 °C, and the average dissolution temperature for the treated crystals was 46.4 °C, both from four independent trials (Figure 2.5A). Interestingly, the initial phase, 20˚C - ~35˚C, dissolution for the crosslinked crystals was flatter than for the control crystals. Absorption gains became apparent at ~35 °C for the crosslinked

crystals, whereas the absorption began to increase immediately for the control samples. This suggested that the crosslinked crystals remained intact over this initial temperature range.

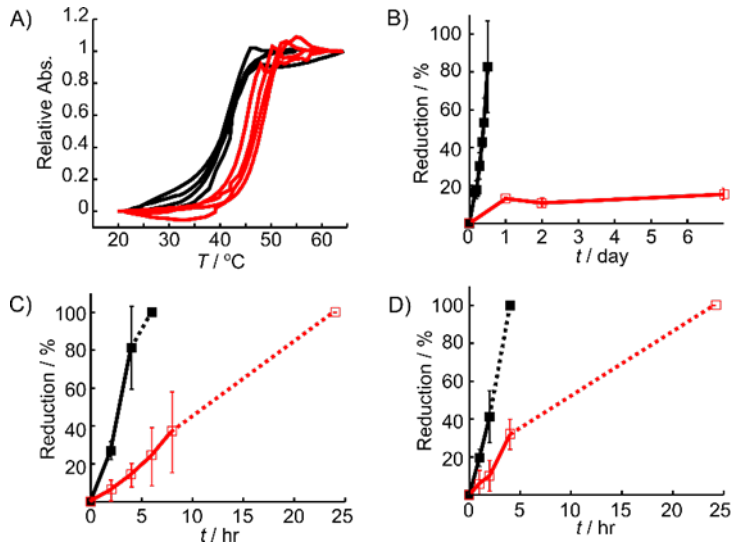

Figure 2.5. NOR-treatment enhances crystal thermal stability. **A.** Dissolution temperature determination. Control (black) or crosslinked (red) crystals were heated to determine the crystal dissolution temperatures by UV absorption. In all four independent trials the crosslinked crystals had higher dissolution temperatures as well as a more shallow initial dissolution phase. Control and crosslinked crystals were also examined at elevated isothermal temperatures: **B.** 33˚C, **C.** 35˚C, **D.** 37˚C. Dashed lines indicate that crystals dissolved between these time points. The terminal time points were not used for determining the linear reduction rates. Each time point is an average measurement from 5 crystals with error bars representing standard deviation.

To confirm that the crosslinked crystals could remain intact at higher temperatures, we made visual observations of the crystals incubated at 33, 35 and 37 °C. At all three elevated temperatures we examined, the control crystals dissolved from the exterior inward, leading to a progressive decrease in size, while initially retaining an overall hexagonal unipyrimidal morphology (Figure 2.6). In all cases the crosslinked crystals showed lower apparent linear reduction rates (Figure 2.5B-2.5D). At 33°C the control crystals had modest stability, disappearing at an observed rate of ~6.6% hr^{-1}. In contrast, the treated crystals did not dissolve at an appreciable

rate when measured in hours, with crystals remaining intact after 7 days. The overall size reduction over the 7 day period was 15.3%, consistent with flat first phase of the curve in the dissolution experiments (Figure 2.5A). At 35°C and 37°C the control crystals dissolved more quickly, with reduction rates of 20.3 and 20.6% hr^{-1}, respectively. The treated crystals also had higher dissolution rates at these temperatures, but these changes were more modest at 4.6 and 8.0% hr^{-1} at 35°C and

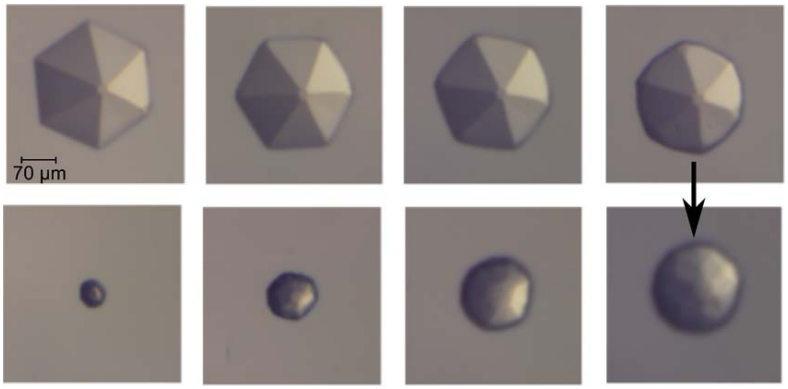

Figure 2.6. Crystal dissolution at elevated temperature. Crystals incubated at elevated temperature dissolve from the exterior toward the interior.

37°C, respectively.

Chapter 2.2.3: Crosslinking decreases cation dependence

Our previous work determined that the 13-mer crystals required divalent cation concentrations of 50-200 mM Mg^{2+} for crystal assembly and stability[31]. To determine if crosslinking impacted the cation dependence we compared crosslinked and control crystal stability by incubating them in the cations that support crystal growth (Mg^{2+} and Ca^{2+}) at various concentrations, with the lower limit chosen near the reported total blood plasma concentrations[54]. In the Mg^{2+} conditions the crosslinked crystals showed enhanced tolerance to the decreased cation concentrations, even at the lowest concentrations tested (Figure 2.7A). At 1 mM Mg^{2+} the control crystals shrank at a rate of 9.2% hr^{-1}. At the same concentration the crosslinked crystals initially showed an overall average 12.1% reduction in size after 24 hours, after which they maintained a

constant size. At 5 and 10 mM Mg^{2+} the control crystals dissolved more slowly, with an apparent half-life of ~6 days. At these concentrations the crosslinked crystals did not shrink appreciably over the course of the 8 day experiment. A similar pattern was seen in the Ca^{2+} conditions (Figure 2.7B). Over four days, the control crystals had an average overall 80% reduction in size at 3 mM, a 50% reduction at 10 mM and 10% reduction at 50 mM. The crosslinked crystals showed only

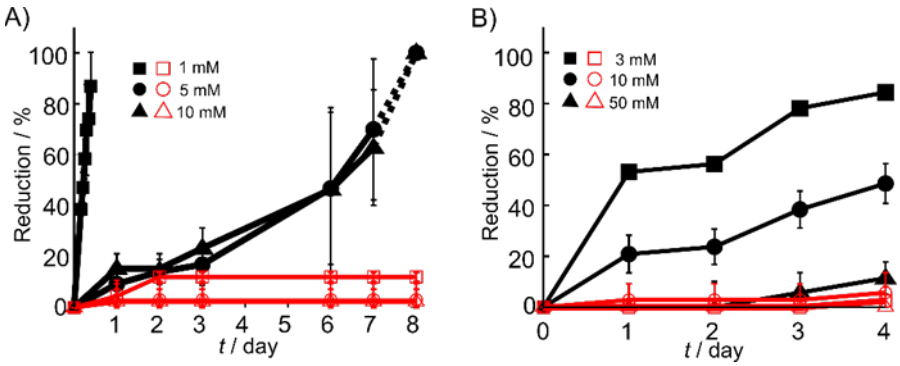

Figure 2.7. Crosslinking decreases divalent cation requirements. Control (black) and crosslinked (red) crystals were examined under three different **A.** Mg^{2+} concentrations, or **B.** Ca^{2+} concentrations at room temperature. In all cases, crosslinked crystals shower lower reduction in size, even at the lowest divalent cation concentrations. The high standard deviations for controls crystals in 5 mM Mg^{2+} and 10 mM Mg^{2+} at day 6 and 7 are the result of one or two crystals completely dissolving.

minimal reductions (maximum 5.7% overall at 10 mM) in all three conditions after 4 days.

All DNA crystals presumably require relatively high cation concentrations for stability due to the high density of negatively charged phosphate groups in the oligonucleotide backbones. These cation requirements can severely limit potential applications of DNA crystals[55]. The covalent interactions introduced by NOR crosslinking appear to sufficiently rigidify the lattice to overcome the repulsive forces associated with the decreased ionic strength and any concomitant changes in Debye length. However, we cannot rule out other factors including cation sequestration as a result of crosslinking, or the positive charge imparted on the N7 position upon alkylation as other sources for lattice stabilization.

Chapter 2.2.4: Crosslinking provides resistance to DNase I and enhances stability in cell culture media

With the growing interest of using nanoscale DNA architectures for cellular applications, there is a need for maximizing the durability of DNA constructs under conditions that mimic cellular and extracellular environments. Several studies have examined the resistance of DNA origami structures to nucleases in solution or those present in serum[32,56]. Though these assemblies were more resistant to nucleases than free plasmid DNA, they were still degraded rapidly by DNase I[32], while incubation in fetal bovine serum (FBS) also led to rapid degradation of DNA assemblies without pre-treatement of the serum to inactivate nucleases[56]. Because DNA constructs are susceptible to nucleases in these settings, we examined the impact of NOR crosslinking on DNase I degradation of the 13-mer crystals, and their survivability in tissue culture medium.

Control and crosslinked crystals were incubated with different amounts of DNase I and the change in crystal sizes were monitored (Figure 2.8A). We note that DNase I has reduced activity at elevated Mg^{2+}/Ca^{2+} conditions[57], however, performing the experiments at high divalent cation concentrations allowed us to separate the divalent cation stability and nuclease resistance between control and crosslinked crystals. The control crystals shrank linearly at rates that correlated with the amount of enzyme, with half-lives ranging from ~3 days (1 U) to ~1.5 days (10 U). Crosslinked crystals, however, showed small reductions in size, with the only visible damage being pitting on the surfaces of some crystals. No single condition resulted in more than a 20% reduction in size after 7 days (Figure 2.8A).

Next, we examined the stability of crystals incubated in DMEM tissue culture medium supplemented with 10% FBS and 10 mM Mg^{2+} (Figures 2.8B & 2.8C). Control crystals were rapidly degraded in this cell culture medium with an apparent half-life of ~20 minutes (Figure

2.8B). The crosslinked crystals showed significantly higher durability under these conditions. After 2 days the crosslinked crystals had not decreased in size, though in some cases the sharp crystal edges had begun to round. The crystals began to dissolve between 2 and 3 days and were still present after 7 days at an average of ~20% their original size.

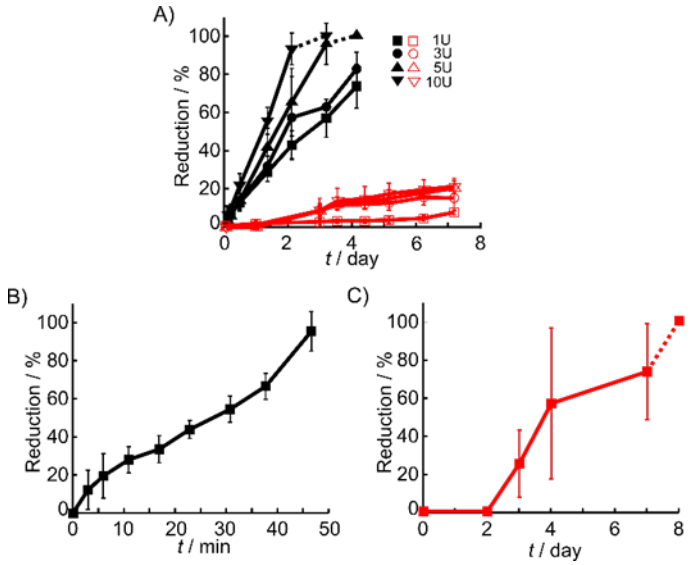

Figure 2.8. NORtreatment enhances nuclease resistance and longevity in tissue culture medium. **A.** Control (black) and crosslinked crystals (red) were incubated with varying amounts of DNase I and the crystal size was monitored over time. **B.** Size reduction of control crystals incubated in DMEM (10% FBS, 10 mM Mg^{2+})at 22˚C. **C.** Size reduction of NOR-treated crystals in the same conditions as (B). The large error associated with the measurement at day 4 was due to two of five crystals dissolving completely between day 3 and 4. The remaining three crystals were used for the day 7 measurement.

Previous studies implicated FBS as the main source of nucleases responsible for the degradation of DNA nanostructures in various culture mediums[56,58]. Therefore, we examined crystal durability in 100% FBS containing 10 mM Mg^{2+} (Figure 2.9). Control crystals degraded rapidly, though they were still visible after 7 hours. Crosslinked crystals showed little change after 20 hours. Interestingly, the greater longevity of control crystals in FBS alone than in DMEM+FBS suggests that some components in DMEM (likely the added salts) may enhance degradation of the crystals.

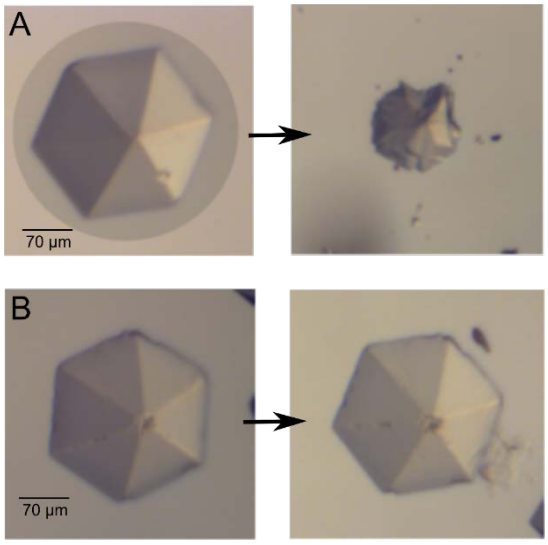

Figure 2.9. Comparison of treated and untreated crystals in FBS+10 mM Mg^{2+}. Untreated crystals at the 0 hour and 7 hour time point are shown in (**A)**, while the NOR-treated crystals at the same time points are shown in (**B)**.

Chapter 2.2.5: G13 is involved in the formation of dimeric crosslinked species

Because each DNA strand in the crystal is identical, if crosslinks occurred between identical nucleotides of two strands only dimeric higher order species would be observed. The appearance of multiple higher molecular weight species in the gel analysis (Figure 2.3) indicated that NOR could form interstrand crosslinks between at least two different nucleotides in the oligonucleotides. We took advantage of the lability of N7 alkylation in hot piperidine to attempt to determine the nucleotides involved in interstrand crosslinking. We focused on the dimeric species as we could obtain sufficient material following gel purification.

We compared piperidine cleavage patterns between dissolved crosslinked crystals, solution crosslinked oligonucleotides, and gel purified dimeric species from crosslinked crystals (Figure 2.10) with guanosine positions determined from DMS-modified 13-mers. Though the 13-mer oligonucleotide contains 7 guanosine nucleotides, we could only resolve the 6 largest radiolabeled

products, as piperidine cleavage at G2 would result in a single nucleotide monophosphate, and cleavage at G1 would remove the 5' ^{32}P label entirely. Thus, we could not interrogate crosslinking at positions G1 or G2. For each of the crosslinked samples we observed all six products, suggesting that in both solution and in the crystal, all of the guanosine nucleobases 3' of G6 were accessible to NOR alkylation. For oligos crosslinked in solution, very little of the full-length or 12 nucleotide product were present, indicating that all positions of the unstructured oligonucleotide in the absence of Mg^{2+} [31] were susceptible to NOR alkylation, and that a majority of oligonucleotides were alkylated one or more times. For the dissolved crosslinked crystals, the full-length 13-mer was the most prominent band (66.5% of quantifiable product), followed by cleavage at G9 (8 nucleotide product; 11.5%), G6 (5 nucleotide product; 5.9%), and G13 (12 nucleotide product; 8.6 %). There were no higher molecular weight products, indicating that piperidine cleavage had removed all of the crosslinked species (Figure 2.3). Interestingly, for the gel purified dimer from the crosslinked crystals, the full-length 13-mer was still the most prominent product (51.2%), followed by cleavage at G13 (19.7%). The largest difference in truncated products between the dissolved crystals, solution crosslinked 13-mer, and the purified dimer was the accumulation of this 12 nucleotide product. This suggests that G13 – which is disordered in the crystal structure – is primarily involved in interstrand crosslinking in the dimer, though we could not exclude other positions, such as G9 or G6, as additional potential crosslinking sites.

The abundance of the full-length 13-mer in the piperidine-cleaved dimer was surprising. We anticipated that the purified dimer would show little to no 13-mer product following piperidine cleavage because at least one nucleotide in each monomer would be alkylated and cleaved into fragments smaller than 13-mers. Control experiments confirmed that the dimeric band was intact following purification (Figure 2.11), suggesting that the appearance of the 13-mer was not the

result of spontaneous cleavage or crosslink reversal. A possible scenario that explains this result is that one or more of the sites responsible for interstrand crosslinking in the dimeric species is insensitive to piperidine cleavage. Piperidine-resistance has been documented for other DNA alkylating agents[59], and this has been attributed to alkylation at sites other than purine N7's, including N2 of guanosine, and N6 or N3 of adenosine. Formation of G-A and A-A intra- and interstrand crosslinks have been reported for other nitrogen mustards[50].

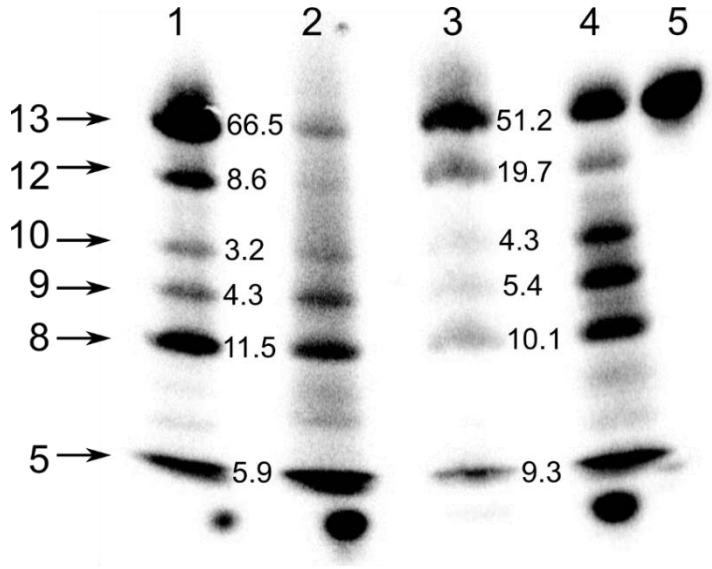

Figure 2.10. G13 is a primary site for NOR-crosslinking. Lane 1, Crosslinked 13-mer crystals treated with piperidine. Numbers on the left indicate nucleotide sizes of the final products. Numbers to the right of the bands indicate the percentage of product based on densitometry. Lane 2, piperidine cleavage of solution crosslinked 13-mer oligonucleotides; Lane 3, gel purified crosslinked dimer band from NOR-treated DNA crystals following piperidine cleavage; Lane 4, DMS-modified 13-mer piperidine cleavage products as a G-ladder control; Lane 5, control 5' labeled 13-mer. The relative amount of the 12 nt product in Lane 3 compared to Lane 1 suggests that G13 is a primary crosslinking site in the purified dimeric species.

Though it is disordered in the crystal structure, two G13's residues are in close proximity based on the strand arrangement (Figure 1.1A) and the positions of G13 phosphates in the crystal structure. Using simple modeling in which the complete G13 nucleotides of the two strands were randomly positioned, we examined positions that would be consistent with the 5 Å arm length of

the nitrogen mustards. Because of their proximity, many different conformations would bring two G13's N7 positions within this 5 Å distance. Several other positions were consistent with this distance restraint, assuming no local structural variations as a result of crosslinking. These included potential interstrand crosslinks between G13(N7)-G1(N2), G13(N7)-G2(N7), G13(N7)-A3(N3), and G13(N7)-G10(N7). Neither G6 or G9 were in a position to form interstrand crosslinks based on N7 positions.

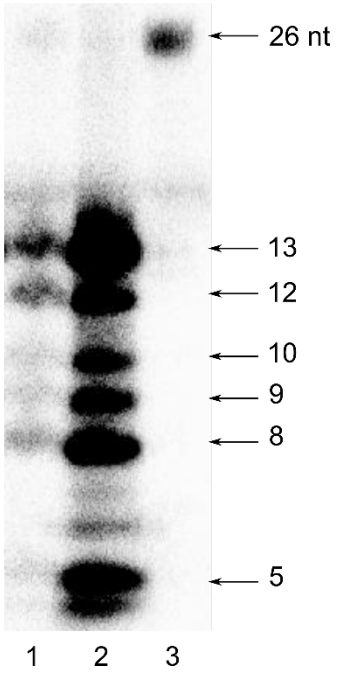

Figure 2.11. Dimeric crosslinked species is intact prior to piperidine cleavage. Lane 1, purified dimeric band from crosslinked crystals after piperidine cleavage; Lane 2, dissolved crosslinked crystals; Lane 3, purified dimeric band from crosslinked crystals without piperidine treatment. The numbers on the right show nucleotide sizes.

Chapter 2.2.6: G13 enhances crystal crosslinking and is required for increased thermal stability.

DNA oligonucleotides lacking G13 crystallize under the same conditions as the 13-mer and have identical crystal morphology. This allowed us to test the functional importance of G13 in crosslinking and crystal stability. Gel analysis following NOR treatment showed that the 12-mer crystals had reduced crosslinking efficiency as judged by the overall amount of crosslinked product

and the lack of significant higher molecular weight species beyond the dimer (Figure 2.12A). We then examined the dissolution temperatures of 12-mer crystals (Figure 2.12B). The dissolution temperature of the control 12-mer crystals (41.2 °C) was consistent with our results from the control 13-mer crystals (41.1 °C; Figure 2.5A), indicating that removing G13 did not compromise the baseline stability of the crystal lattice. Consistent with the decreased overall crosslinking in the absence of G13, there was no increase in the thermal stability of the crosslinked 12-mer crystals (Figure 2.12B), but rather a reduced dissolution temperature compared to the control. This suggests that some alkylation events may destabilize portions of the crystal lattice, and that the interstrand crosslinking afforded by G13 can overcome such destabilizing events. Together with the piperidine cleavage experiments these results show that the unpaired G13 residue is involved in interstrand crosslinks, that it is responsible for enhancing crosslinking beyond the dimer, and that those crosslinks are necessary for enhanced thermal stability.

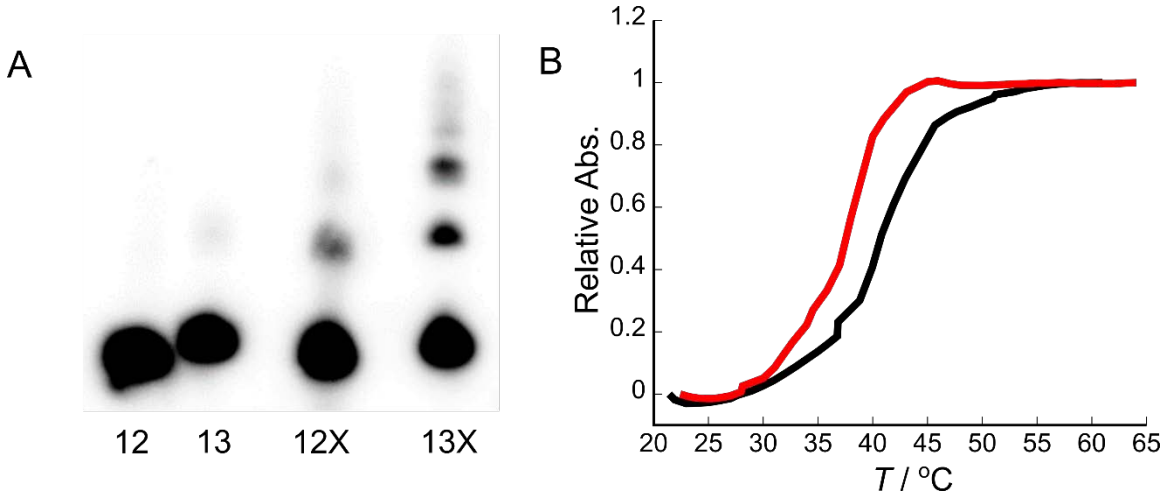

Figure 2.12. G13 is necessary for efficient crosslinking and enhanced thermal stability. **A.** Gel analysis of 12-mer crystal (lacking G13) crosslinking. 12 and 13 are labeled 12-mer and 13-mer oligonucleotides, respectively. 12X and 13X are dissolved NOR-treated crystals. The 12-mer displays lower crosslinking efficiency and fewer higher molecular weight products than the G13-containing crystals. **B.** Dissolution experiments of 12-mer crystals that are uncrosslinked (black) or NOR-treated (red).

Chapter 2.3: Conclusion

Here we have developed a simple chemical crosslinking strategy for improving the durability of 3D DNA crystals. Our results clearly demonstrate that treating crystals with nornitrogen mustard leads to increased thermal stability, decreased cation dependence, and increased nuclease resistance. The utility of DNA constructs in biological and non-biological settings is highly dependent on their versatility under different environmental conditions, and our results suggest chemical crosslinking is one method to achieve that versatility. Additionally, though we did not see enhancements in x-ray diffraction following crosslinking, it is possible that this may be useful as a technique for improving DNA crystal diffraction, similar to protein crystal crosslinking. This study has also demonstrated the importance of the unpaired G13 nucleotide for crosslinking efficiency and thermal stability in this model crystal, though it is not yet clear how general this feature would be for other DNA constructs. Overall, this technique is a simple single step treatment to form covalent linkages that improve durability without the use of costly nucleotide derivatives.

Chapter 2.4: Materials and Methods

Chapter 2.4.1: Oligonucleotide synthesis, purification and crystallization

The oligonucleotides were synthesized on an Expedite 8909 (PerSeptive Biosystems) with reagents from Glen Research (Sterling, VA) using standard phosphoramidite synthesis and deprotection. Oligonucleotides were gel purified and electroeluted as previously described[20] before dialysis against deionized water.

The oligonucleotides were crystallized by sitting drop vapor diffusion. 2 µL of DNA solution (200 µM) and 1 µL crystallization buffer (10% 2-methy-2,4-pentanediol, 120 mM magnesium formate,

50 mM lithium chloride) were incubated against 300 µL of crystallization buffer in the reservoir. Trays were incubated overnight at 22º C and provided 5-10 crystals per well.

Chapter 2.4.2: Crosslinking and gel analysis

Crystals were removed from the crystallization tray and placed in a glass soaking dish and washed with 100 µL of 120 mM magnesium formate for 5 mins to remove free DNA. The crystals were then transferred to 120 mM magnesium formate with 250 mM freshly added nornitrogen mustard (Sigma-Aldrich, St. Louis, MO) and soaked >12 hours at 4 ºC. The buffer was removed and crosslinking step was repeated a second time in freshly prepared buffer for another 12 hours at 4 ºC. Crosslinking of oligonucleotides in solution was performed by addition of 0.5 M nornitrogen mustard to 200 µM of oligonucleotide solution and incubated at 4˚C.

Interstrand crosslinks were identified by polyacrylamide gel electrophoresis. Crosslinked crystals were prepared by soaking in 100 µL water for 5 mins before being transferred to 4 µL of water that was heated to 95˚C to dissolve the crystals. Crystals to be radiolabeled were transferred to 38 µL of water and dissolved by heating prior to adding 5 µL 10X T4PNK Reaction Buffer, 2 µL T4 polynucleotide kinase (New England Biolabs), 5 µL of 50 pmol [γ-32P] ATP (PerkinElmer) and incubated at 37˚C for 30 mins. Samples were incubated for 5 mins at 95˚C prior to loading onto a 20% denaturing polyacrylamide gel (19:1).

Chapter 2.4.3: Crystal stability measurements

Dissolution profiles were obtained on a Cary100 Bio UV-VIS spectrophotometer using a 0.2°/min temperature ramp with absorbance at 260 nm recorded every minute. Overall crystal stability was measured by visual observations of crystals sizes recorded using a stereo microscope with attached CCD camera. The percent reductions over time were determined by measuring the change of

crystal diameter across the hexagonal base. For all of the stability assays, a minimum of 5 crystals were used with average values reported. To test thermal stability, crystals were soaked in 120 mM magnesium formate for 5' to remove any excess NOR and then transferred to fresh 120 mM magnesium formate solution and incubated at various temperatures. For divalent ion concentration stability, the crystals were initially transferred to drops containing 100 µL buffer solution at the final divalent ion concentration as a wash step before being transferred to a fresh 100 µl drop and incubated at 22˚C. For DNase I stability tests, crystals were soaked in 120 mM magnesium formate to remove any free oligomers and NOR before being transferred to 100 mM magnesium formate, 20 mM calcium chloride solution with the addition of varying concentrations of DNase I to a final volume of 15 µL. Crystals were incubated at 22˚C. Similarly, crystals were washed in 10% magnesium formate before being transferred into either Dulbecco Modified Eagle Medium (DMEM) (supplemented with 10% FBS and 10 mM magnesium formate) or 100% FBS (supplemented with 10 mM magnesium formate) at 22˚C.

Chapter 2.4.4: Piperidine cleavage

DMS G-ladder control was generated by incubating radiolabeled DNA in DMS reaction buffer (50 mM sodium cacodylate pH 8.0, 1 mM EDTA, 1 mM dimethyl sulfate) at room temperature for 5 mins. The reaction was terminated by addition of stop buffer (1.5 mM sodium acetate pH 7.0, 1.0 M β-mercaptoethanol). Piperidine cleavage was carried out essentially as previously described[60]. Briefly, radiolabled DNAs were incubated at 95 ˚C in the presence of 1 M piperidine for 30'. Samples were dried under vacuum before being redissolved in gel loading buffer before being resolved on 20% (19:1) PAGE.

Chapter 2.4.5: Gel purification of crosslinked species

The radiolabeled crosslinked treated crystals were separated on a 16 x 22 cm 20% polyacrylamide gel. The gel portion containing the dimeric species was identified by autoradiography, excised, minced, and soaked in water overnight at room temperature with gentle agitation. The solution was filtered and the supernatant was ethanol precipitated overnight with glycogen as a carrier. The precipitated DNA was resuspended in deionized water.

Chapter 3: Enhancing Durability of Three Dimensional Crystals Using Polydopamine

Chapter 3.1: Introduction

The deposition of polydopamine (PDA) on/into the 13-mer crystal was explored as an alternative and more passive way, relative to NOR treatment[38], to enhance the durability of the crystal lattice. The concept was derived from 3,4-dihydroxy-L-phenylalanine (DOPA) secreted from mussels[61,62]. The DOPA plays an important role in the mussels' ability to attach to almost any wet surface. The PDA derived from DOPA can deposit on a variety of surface types[63] (both inorganic and organic materials, and some polymer surfaces) and form a PDA coat. This PDA coat has primarily been utilized as a single step, solution based technique for simple layer-by-layer (LbL) assembly. Currently, this type of LbL has primarily been used to form a layer for functionalization[61,63,64] or for capsule formation[65].

Dopamine is capable of self-polymerization via the formation of the self-cyclized 5,6-dihydroxyindole (DHI) (Figure 3.1A)[66–68]. First, the hydroxyl groups on dopamine are oxidized to form dopaminequinone. Then, the dopaminequinone goes through intramolecular cyclization to become leukodopaminechrome. Oxidation and rearrangement of leukodopaminechrome forms 5,6 dihydroxyindole (DHI). DHI is the precursor for polymerization; DHI can interact with either DHI or dopamine to form polymerized dopamine coat[69]. Self-polymerization can occur either through the covalent or noncovalent pathway (Figure 3.1B). In the covalent pathway, DHI polymerizes with a second DHI forming a 2,2-linked DHI-DHI dimer. Then, the DHI-DHI dimer forms a link with dopamine between the C-4 of DHI and C-5 of dopamine. The non-covalent pathway involves DHI and dopamine stacking on top of one another via ionic, cation-pi, pi-pi, quadrupole-quadrupole or hydrogen bonding.

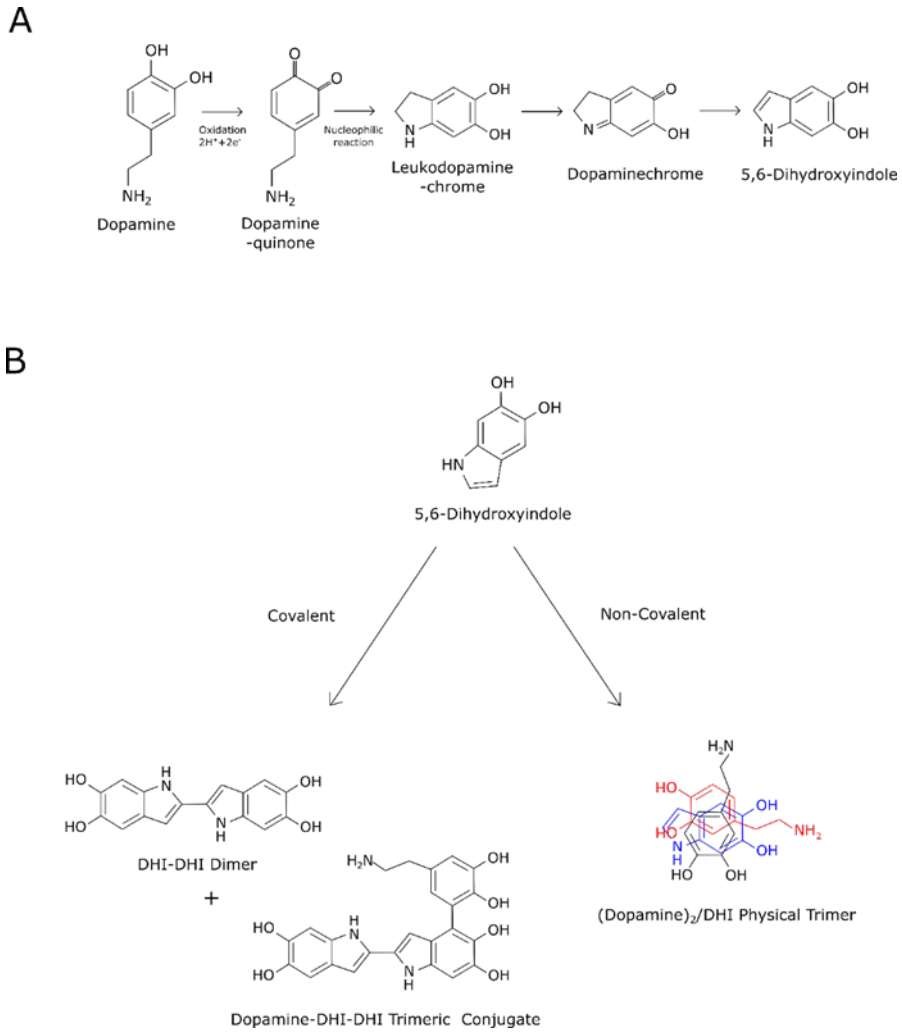

Figure 3.1. Pathways for dopamine polymerization. **A.** Self-cyclization of dopamine into 5,6-dihydroxyindole (DHI). **B.** Self-polymerization of DHI and dopamine can occur via the covalent pathway or the non-covalent pathway.

The PDA can act as a reinforcing network to hold the crystal lattice in place with several potential benefits for PDA over the method previously described (from Chapter 2). First, the PDA coat is opened for surface modification via simple catechol chemistry[61,63,64]. The purpose of the surface modification is to functionalize the core that the PDA deposited onto. In other studies, this has allowed tailoring for specific applications such as drug delivery[70] and acting as a biosensor[71,72]. Importantly, dopamine and the PDA pose no toxicity to the cell[65], which may not be the case for NOR-treated crystals. Furthermore, guanines need to be present within close

proximity of one another and be in the right orientation in order for NOR to be effective, while dopamine can be deposited on a wide variety of surfaces. Additionally, the PDA coat could enhance the durability of the crystal lattice without modifying the underlying structure. NOR provides an effective method for stabilizing 3D DNA crystal via chemical modification of the lattice structure[38], but PDA coat formation provides an alternative when chemical modification to the crystal framework is unwanted or unfavorable to the application.

The two main factors we examined that can affect dopamine polymerization and can be easily manipulated in the lab are pH and temperature. By altering the pH and/or temperature, we could modulate the extent of polymerization and therefore control the shell thickness of the PDA coat. Based the on polymerization chemistry, neutral and basic conditions are optimal for polymerization[61], while acidic conditions hinder polymerization. The alkaline environment aided in the deprotonation of the hydroxyl groups on dopamine and oxidized dopamine into dopamine-quinone, the precursor for dopamine polymerization.

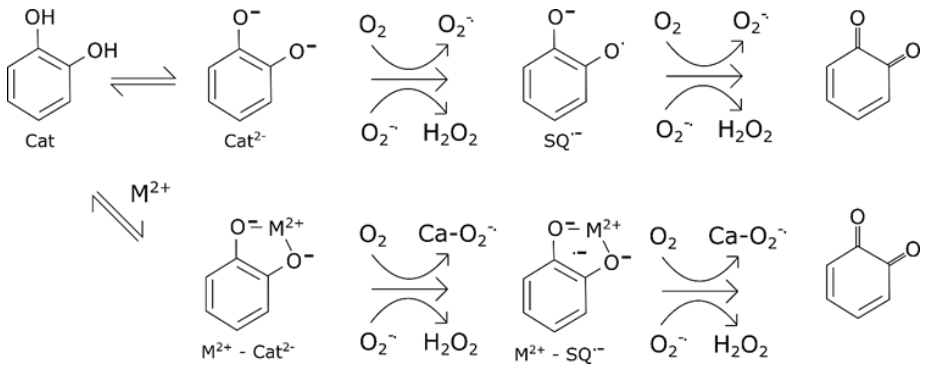

Figure 3.2. Schematic of metal complexations between catechol and group two metals.

In addition to the pH and temperature, we analyzed dopamine polymerization in the presence of high magnesium, which is normally required for the stability of DNA crystals. The catechol group in dopamine can coordinate metal ions (Figure 3.2) and play a role in the mechanical properties of DOPA in mpf-1 mussels proteins[73], while also impacting oxidation rate

[74]. Oxidation of dopamine leads to the formation of dopamine-quinone, which is an important intermediate for dopamine polymerization (Figure 3.1A). The presence of high metal ion concentration can decrease the pK_a of the hydroxyl groups, allowing deprotonation to occur at a lower pH. Once the hydroxyl group becomes fully deprotonated, there will be excess electron density on the catechol, making it more susceptible to oxidation (Figure 3.2).

My work here shows PDA deposition on the crystals can enhance overall crystal stability by increasing thermal stability and stability at low divalent cation concentrations. We applied the polymerization condition to the 13mer crystals we previously characterized[31] (Figure 1.1) and saw a direct effect between pH and temperature, and PDA coat formation. We examined the ability of the PDA coat to stabilize 13mer crystal at low magnesium concentration and at elevated high temperatures, as previously done with the NOR-treated crystals[38]. We found that the PDA coat increased the stability of the 13mer crystals in both conditions. The ability of the PDA coat to stabilize the crystal lattice is the first time PDA had been used as a framework to preserve the integrity of crystallized macromolecules.

Chapter 3.2: Results and Discussion

Chapter 3.2.1: Evaluating polydopamine formation

First, we explored PDA formation when pH and/or temperature were varied. We tested PDA formation in 120 mM magnesium formate at three temperatures (4˚C, 22˚C and 37˚C), and varied the pH between 5.5 and 8.5. Dopamine forms black-brown precipitate when polymerization has occurred, allowing for facilitated visual identification[69] and detection at OD 600. The results showed that the maximum polymerization varied across the different pH and temperature tested (Figure 3.3). At all three temperatures tested, optimal formation was at pH 7.5, followed by pH 8.5, with minimum dopamine polymerization at pH 5.5, 6.5 and no buffer

conditions. The pattern of dopamine formation at different pH showed that the high magnesium concentration did not significantly change the PDA formation from what was seen previously[63,65] at pH 8.5 where dopamine polymerization was optimal at neutral or basic pH. Additionally, dopamine formation plateaus off after 4-5 hours, consistent with previous results.

There was a general positive correlation between PDA formation and increased pH. The increased PDA formation with increasing pH agrees with previous reports that basic pH would allow greater oxidation of the hydroxyl groups, thereby increasing PDA formation as the availability of DHI becomes higher (Figure 3.1). Surprisingly though, it was expected that pH 8.5 would have been the most polymerized[63,65], we observed this at pH 7.5. There was no difference between the sodium cacodylate (NaCaCo) and the Tris HCl buffer used ruling out dependence in buffer composition. Overall, the PDA formation pattern at the different pHs was consistent across the different temperatures tested at 4˚C, 22˚C, and 37˚C. Although there was a general increase at OD 600 as the temperature was increased from 4˚C to 22˚C, and from 22˚C to 37˚C. The increased polymerization as the temperature increased may be the result of faster rate of oxidation of the hydroxyl groups which would had also increased the availability of DHI for polymerization.

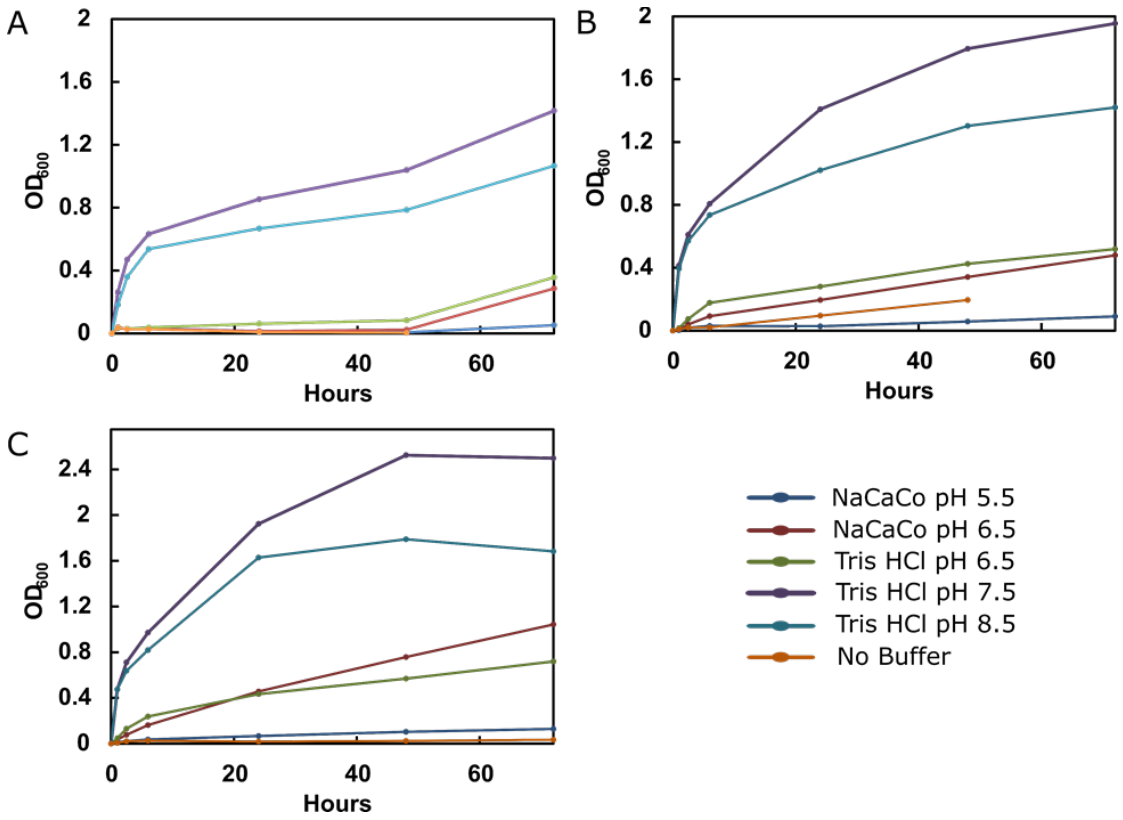

Figure 3.3. Polydopamine (PDA) formation measured at OD 600 at **(A)** 4˚C, (**B)** 22˚C and **(C)** 37˚C.

Chapter 3.2.2: Polydopamine coat formation on 13mer crystal.

Next, we treated the 13-mer crystals with dopamine from each of the previous tested PDA formation condition, pH 5.5 – 8.5, and temperatures 4˚C and 22˚C. Crystals treated in the optimal PDA formation conditions of pH 7.5 and 8.5 developed a darkly coated surface (Figure 3.4). Crystals at low pH conditions, 5.5 and 6.5, did not show a PDA coat. Moreover, the crystals treated at 22˚C clearly showed a darker PDA coat than those treated at 4˚C. The pattern of coat formation on the crystals was consistent with the PDA formation results in the absence of the crystals (Figure 3.3) indicating the maximum polymerization seen in the absence of the crystals correlated to dopamine deposition on the crystals.

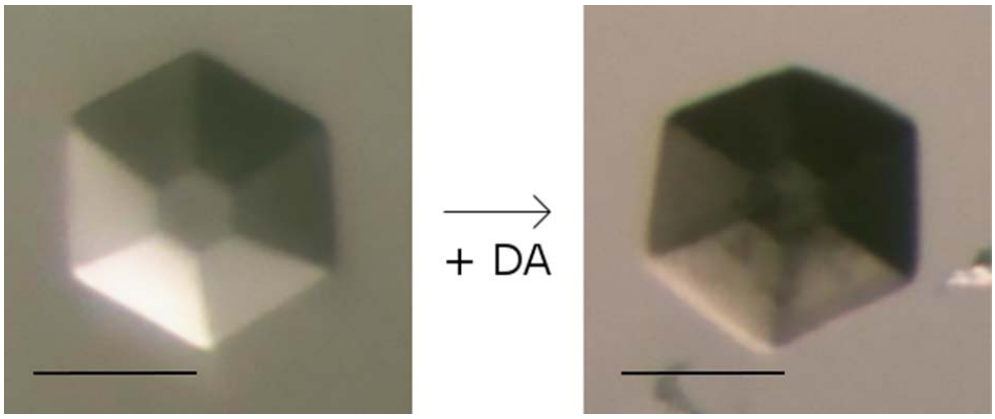

Figure 3.4. Polydopamine (PDA) coat on 13-mer crystal.

No PDA coat was formed or observed at pH 5.5, at 4˚C and 22˚C, and pH 6.5, at 4˚C. The lack of PDA coat formation did not mean that dopamine had no effect on the crystal lattice. It has been shown at acidic pH, dopamine can form adducts with guanine or adenine[75]. To test this, we dissolved the dopamine-treated crystals and ran them on a denaturing gel to assess the presence of higher molecular weight oligomers. The gel showed no higher molecular weight bands and no unusual shifts in the bands compared to the untreated control crystal (Figure 3.5). This indicated there was no observed modifications made to the oligomers of the crystal lattice at acidic pH and at the other conditions.

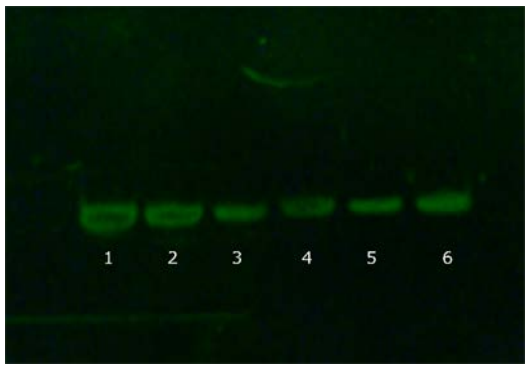

Figure 3.5. Acrylamide gel of PDA-coated 13-mer crystals. 1. 13-mer crystals alone. Crystals were treated with dopamine at 2. 10 mM NaCaCo pH 5.5; 3. 10 mM NaCaCo pH 6.5; 4. 10 mM Tris HCl pH 7.5; 5. 10 mM Tris HCl pH 8.5; and 6. No buffer. There were two crystals in each well.

Chapter 3.2.3: Stability of polydaopmine-coated crystals at low magnesium concentration

We further evaluated whether the PDA coat would enhance durability at low magnesium concentration and found that the PDA coat varied in its ability to stabilize the crystals in 10 mM magnesium formate depending on the original PDA polymerization condition (Figure 3.6). Crystals at 22°C and pH 6.5, or with no buffer were the most effective in stabilizing the crystal lattice. The crystals incubated with dopamine at pH 5.5 at both 4˚C and 22˚C dissolved by day 2. This was consistent with the low levels of polymerization seen previously indicating little to no PDA coat formation to help stabilize the crystals. Dopamine treatment of crystals at pH 5.5 actually ended up decreasing the stability of the crystal lattice: the non-treated crystals lasted longer, with an 80% reduction in diameter at day 7 (Figure 2.7A). This could be due to the effect of the low pH environment, which had been shown to cause crystal degradation. Meanwhile, the crystals from the other conditions showed varied levels of degradation; the crystals were either pitted, had decreased in diameter or both. In this case, the pH that promoted the highest PDA formation did not provide the highest level of crystal stabilization.

The highest level of stabilization was achieved at pH 6.5 and no buffer, which had lower PDA formation compared to the more basic pHs conditions (Figure 3.3). One possible explanation for this was the low PDA formation could have been the result of slower rate of formation, allowing the dopamine monomers or low molecular weight PDA to penetrate into the solvent channels before a complete PDA coat formation occurred resulting in a more extensive PDA network. Additionally, the extensive network may be more effective in chelating or trapping magnesium ions during the polymerization process resulting in a reserve of cations when the crystals were moved to lower magnesium conditions.

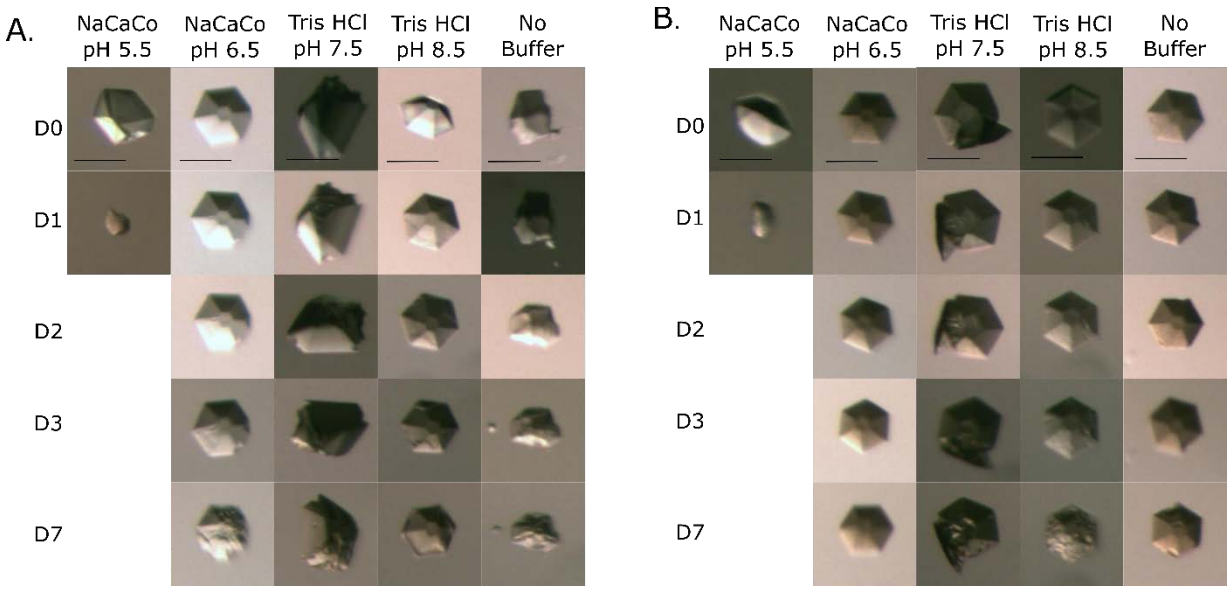

Figure 3.6. Stability of PDA-coated crystals in 10 mM magnesium formate. PDA coat formation on crystals at **A.** 4˚C and **B.** 22˚C. Above the columns are the pH conditions for PDA deposition onto the crystals, and to the left of the columns are days the images were taken. Scale bars, 70 µm.

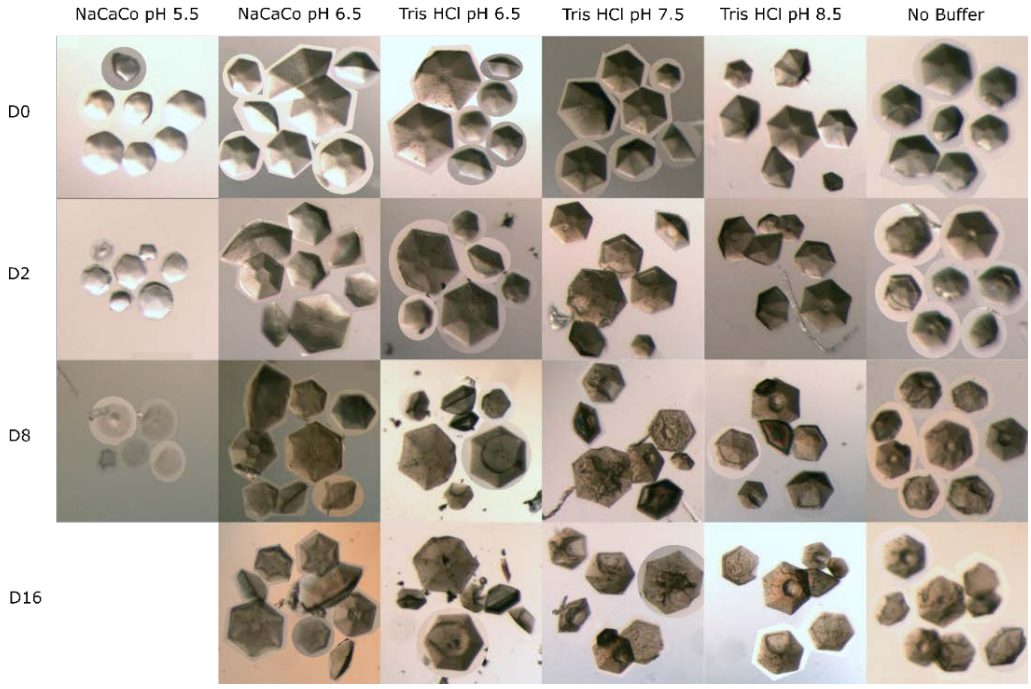

Figure 3.7. Stability of crystals with PDA coat formation at 22˚C incubated at 30˚C. Above the columns are the pH conditions are the pH conditions for PDA deposition onto the crystals, and to the left of the columns are days the images were taken. Scale bars, 70 µm.

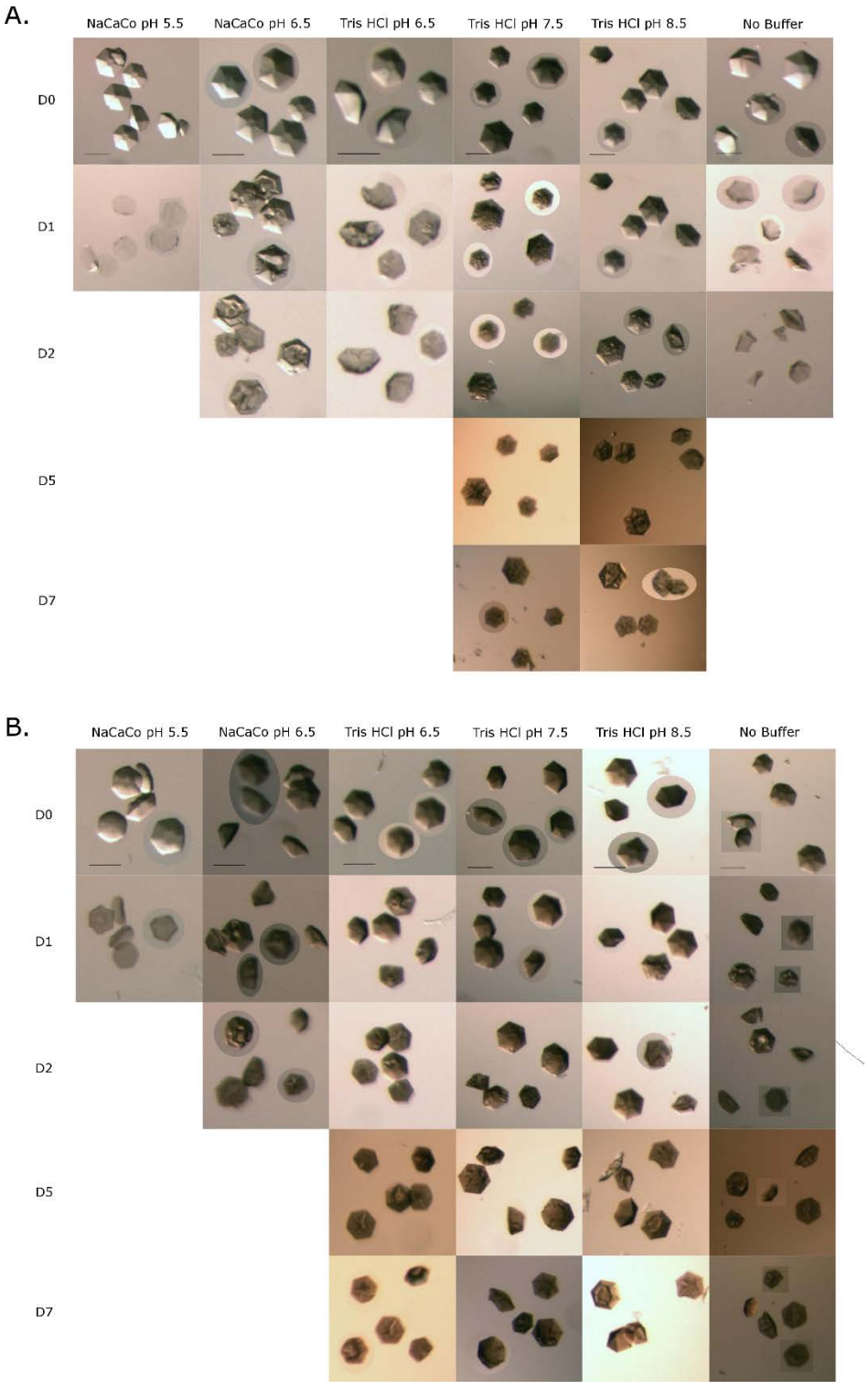

Figure 3.8. Stability of PDA-coated crystals at 37˚C. Stability of crystals with PDA coat formation **A.** at 4˚C incubated at 37˚C and **B.** at 22˚C incubated at 37˚C over time. Above the columns are the pH conditions are the pH conditions for PDA deposition the crystals, and to the left of the columns are days the images were taken. Scale bars, 70 µm.

Chapter 3.2.4: Thermal stability of polydopamine-coated crystals

In addition to evaluating the PDA-coated crystals at low magnesium concentration, we evaluated the thermal stability of the PDA-coated crystals at 30˚C and 37˚C. Similar to crosslinking results, we saw improvement in the thermal stability of the coated crystals compared to the non-coated crystals. Impressively, when the crystals were incubated at 30˚C, all the coated crystals were still present by day 16, except for the coated crystals at pH 5.5. Although most of the coated crystals have degraded in quality to some extent, yielding a mixture of empty "husks" (presumed to be PDA networks, ~ 20%), partial filled dopamine shells (~70%) or intact crystals (~10%). Crystals originally at 22˚C pH 8.5 fared the best, showing no degradation at day 2 while the crystals in the other conditions had begun to cracked, pitted or degraded (Figure 3.7). For the crystals at 37˚C, crystals initially treated with dopamine at 4˚C pH 8.5, 22˚C pH 7.5 and 22˚C pH 8.5 showed the best stability as they were unchanged at day 1 (Figure 3.8), compared to non-coated crystals that were gone within a day (Figure 2.5D). By day 7, the majority of the crystals had left behind an empty husk, except a handful of crystals from conditions 22˚C pH 7.5 and pH 8.5 while crystals at pH 5.5 were completely gone by day 1.

The conditions that led to the best improvement in thermal stability correlated to the highest maximum PDA formation measured at slightly basic conditions and 22˚C. This was in contrast to the magnesium results where dopamine formation on the crystals at pH 6.5 had shown to provide the best stabilization. This indicated intrinsic differences in how the PDA coat influenced crystal stability in different ways. The higher dopamine polymerization may have resulted in thicker coating of the PDA around the crystals, acting as a reinforcing net on the crystal.

Both the PDA coat and the NOR-treatment[38] had increased the overall durability of the crystals, but they differ in the degree they strengthen the crystals in each stability test. The stability of the crystals treated in the optimal PDA formation condition at 10 mM magnesium formate was similar to the NOR crystals, with both treatment methods showing indefinite stability compared to their respective controls. On the other hand, there were mixed results with the thermal stability data when evaluating which method was better. At 30˚C, the PDA-coated crystals had showed significant degradation or had completely dissolved (Figure 3.7) while the NOR-treated crystals had remained indefinitely stable at 33˚C (Figure 2.5B). However, at 37˚C, the NOR-treated crystals were gone within 24 hours (Figure 2.5D) while the optimal dopamine-treated crystals were still present in day 7 (Figure 3.8B).

While we know the PDA coat enhanced the overall durability of the crystal lattice, it is unclear exactly how the PDA coat was stabilizing the crystal lattice. The catechol group of dopamine and its derivatives may had played a role due to their ability to form a metal complex with magnesium. Magnesium plays a vital role in the stability of the DNA crystals by shielding the repulsion due to the closely packed negatively charged DNA backbone. The PDA coat could have acted as a net, trapping the excess magnesium that would otherwise be absent, and this would have contributed to the overall stability of the crystal.

Chapter 3.3: Conclusion

The application of the PDA coat on 3D DNA nanostructures provides an alternative, non-covalent method of improving the durability of 3D DNA crystals. We showed that changing the pH and temperature can modulate the rate of formation and the maximum formation reached which will in turn effect on how effective the PDA was in improving the durability of the DNA crystals. The optimal conditions significantly improved thermal stability and durability at

decrease low magnesium concentration. For the first time, we show here that PDA formation can act as a stabilizer of macromolecular structures.

Chapter 3.4: Materials and Methods

Chapter 3.4.1: Oligonucleotide synthesis and purification

The oligonucleotides were ordered from IDT (Integrated DNA Technologies) or synthesized on an Expedite 8090 DNA synthesizer (PerSeptive Biosystems) with reagents from Glen Research (Sterling, VA) using standard phosphoramidite synthesis and deprotection. Oligonucleotides were gel purified and electroeluted as previously described[20] before dialysis against deionized water.

Chapter 3.4.2: Crystallization

Oligonucleotides were crystallized by sitting drop vapor diffusion. 2 µL of 200 µM 13 nucleotide oligomer and 1 µL water were added to the sitting drop, followed by 1 µL of crystallization buffer (10% 2-methy-2,4-pentanediol, 120 mM magnesium formate, 50 mM lithium chloride). Drops were equilibrated against 300 µL of crystallization buffer. Crystal trays were incubated overnight at 22˚C.

Chapter 3.4.3: Polydopamine formation

1.5 mL of 10 mM Sodium cacodylate pH 5.5, 10 mM Sodium cacodylate pH 6.5, 10 mM Tris HCl pH 6.5, 10 mM Tris HCl pH 7.5, 10 mM Tris HCl pH 8.5, and no buffer solutions with 10 mM dopamine HCl and 120 mM magnesium formate in 1.7mL Eppendorf tubes were incubated overtime at 4˚C, 22˚C and 37˚C. Samples were measured at OD 600 at the designated time points.

Chapter 3.4.4: Polydopamine deposition on crystals

10 uL of 2X PDA formation (except with 60 mM magnesium formate instead of 120 mM) solutions above were added into 10 uL of 120 mM magnesium formate in 24 well crystal trays containing crystals and incubated overnight.

Chapter 3.4.5: Crystal stability measurements

PDA-coated crystals were transferred to fresh 100 uL aliquots of the equivalent buffer solutions that the crystals were initially in to wash away excess PDA. The crystals were then transferred to 15 uL of the same buffer for the stability experiments. Overall crystal stability was measured by visual observations of crystal sizes, recorded using a stereo microscope with attached CCD camera. The percent reductions over time were determined by measuring the change of crystal diameter across the hexagonal base. For all of the stability assays, a minimum of 5 crystals were used with average values reported. For divalent ion concentration stability, the crystals were initially transferred to drops containing 100 µL buffer solution at the final divalent ion concentration as a wash step before being transferred to a fresh 15 µl drop and incubated at 22˚C.

Chapter 4: Incorporation of Doxorubicin in 3D DNA Crystals

Chapter 4.1: Introduction

Doxorubicin (DOX) or Adriamycin® is one of the most effective anticancer treatment on the market and has been approved for used for more than 30 years. Derived from daunorubicin, an antibiotic produced by *Streptomyces peucetius,* it was found to be an effective treatment against acute leukemia and lymphoma[76] in the 1950s. Since then, DOX has been categorized as a broad-spectrum anti-cancer treatment, effective against a wide variety of solid tumors, multiple myeloma, and Hodgkin's and non-Hodgkin's lymphoma[77,78].

The exact mechanism of DOX's therapeutic action is unclear. One of the most accepted mechanisms is the interference with topoisomerase II (Top II)[79]. Top II relaxes DNA supercoils formed during DNA transcription by cutting a double helix and passing another double helix strand through it, and resealing the cut duplex afterwards. DOX interferes with this process by stabilizing the Top II complex after cutting, preventing the resealing with double helix, and therefore stalling DNA replication.

Despite DOX's high efficacy, DOX has poor target selectivity, which can lead to adverse side effects, such as cardiotoxicity[80]. One resolution to this issue is the encapsulation of DOX within a delivery device targeted towards the cancer site. In addition to circumventing adverse side effects, this will increase target selectivity, increase cellular uptake, and increase the half-life of DOX.[81,82]

There are drug delivery vehicles made from lipids[83,84], polymers[85], and metallic nanoparticles[86]. Devices made from lipids are in the form of liposomes, spheres with lipid bilayer membranes. Polymeric devices are largely based on poly(D,L-lactic-co-glycolic acid) (PLGA) polymers. Each of the material as a drug delivery device has their own advantages and

drawbacks. The drawback of liposomes are slow release from the lipid vehicles, thereby lowering their effectiveness [87,88]. Polymeric devices are rapidly cleared from the blood stream, therefore decreasing the effectiveness of the drug[89]. For metal nanoparticles, the drawback is the accumulation of metal particles in the body which can lead to toxicity[86].

DNA nanostructures are a prospective class of nano-delivery devices with several distinct advantages[90]. The diverse architectures that can be generated allows them to be tailored to specific applications[9,39]. For instance, rod shaped nanoparticles have better cellular uptake than spherical shape nanoparticles[37], therefore rod shaped DNA nanostructures can be specifically produced for this function. Another benefit of DNA nano-delivery devices is they are biocompatible and do not exhibit cell cytotoxicity or immunogenicity[24,91,92]. Additionally, the delivery of DOX via DNA origami has been shown to be effective against cancer cells already resistant against DOX[41]. DOX, especially, is known to induce multi-drug resistance in cancer cells[93,94] thus efficacy against drug resistant cancer cells will address one of the leading problems in cancer treatment.

Several DNA nanostructures have already been evaluated as drug delivery devices for DOX, such as the triangle-shaped DNA origami[24] and DNA icosahedra nanocages[25]. These DNA nanostructures have been shown to be successful in delivering DOX to cells or animal models[24,25]. DOX mainly associates with these DNA nanostructures via intercalation[41,95–97]; the disadvantage of incorporation via intercalation alone is that it limits the loading capacity of the DNA container. The limited loading capacity can be solved by increasing the density or sequestering the drugs in other spaces. DNA crystals provide a unique solution to this problem. Crystals would allow DOX to be incorporated within the solvent channels as well as via intercalation, thereby increasing the loading capacity.

Here, we assessed a 3D DNA crystal[31] composed of self-assembled 13 nucleotide long oligomers as a potential DNA nanostructure for drug delivery. We quantified the crystal's ability to incorporate and retain DOX using microscopy and fluorimetry and confirmed incorporation of DOX at high concentrations within the crystal lattice. Moreover, we improved the retention of DOX within the DNA crystal by transitioning the crystal lattice state into a gel state. This was achieved by partial destabilization of the crystal lattice either by soaking at high DOX concentration and/or lowering the magnesium concentration. The ability to limit diffusion of the DOX prematurely is important for restricting exposure of the drug to non-target sites before it reaches its destination, thereby also increasing the load of the cargo when the target is reached.

Chapter 4.2: Results and Discussion

Chapter 4.2.1: Incorporation of doxorubicin into 13mer crystals at room temperature

Doxorubicin was introduced into the solvent channels of the 13mer crystals via diffusion. We submerged the crystals in DOX containing solution ranging from 1.68 μM to 430 μM, and monitored them for up to 4 days. Both the NOR-treated crystals and non-treated crystals were used in order to compare the effect of crosslinking on the durability of the crystal lattice during DOX exposure. DOX contains an anthraquinone chromophore (Figure 4.1A) that gives the molecule a bright red coloration (Figure 4.1B) which aids visualization of DOX underneath the light microscope. We immediately observed bright red coloration within the crystals underneath the light microscope after 1 day, demonstrating successful DOX incorporation. Additionally, there was a positive correlation between the intensity of the red coloration and the DOX concentration the crystals were submerged in (Figure 4.2). The correlation between the DOX concentration and color intensity suggested the amount of DOX intercalated into the lattice was

concentration dependent. This was further supported by the observation that the crystals degraded as the DOX concentration increased, suggesting higher level of DOX intercalating into the lattice also induced instability.

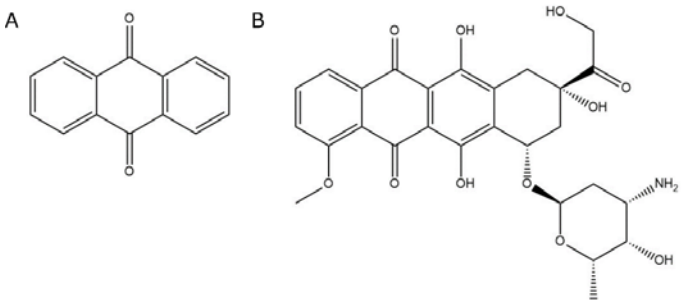

Figure 4.1. Structure of A. anthraquinone and B. doxorubicin.

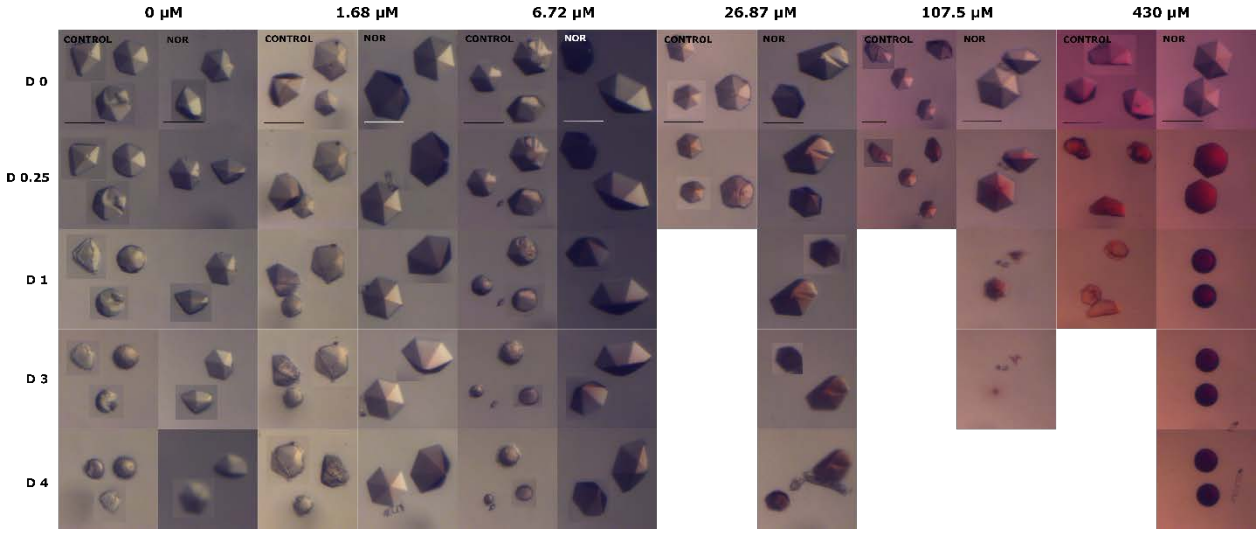

Figure 4.2. Light microscope images of crystals soaked in DOX at room temperature. We added the non-treated crystals (Control) and NOR-treated (NOR) crystals to buffer (10 mM Tris HCl pH 7.5 and120 mM magnesium formate) with DOX, concentrations above the columns, at day 0 (D0). Scale bars, 70 µm.

Crosslinking the crystals mitigated the degradation due to DOX exposure. In all the conditions, the NOR crosslinked crystals exhibited better stability in the presence of DOX relative to the non-treated crystals (Figure 4.2). For instance, the crosslinked crystals at 1.68 µM and 6.72 µM showed little or no reduction in size by day 4, while the non-treated crystals had

reduced in size significantly. The non-treated crystals at 1.68 µM showed an average percent reduction of 17.65% and became rounded, a sign of degradation, while the crosslinked crystals showed a lower average percent reduction of 4.33%. The crosslinked crystals also showed a lower average percent reduction at 6.72 µM of 6.72% while the non-treated crystals showed an average of 58.32% reduction. The trend continued at higher DOX concentration of 26.87 µM, 107. 5 µM and 430 µM where the non-treated crystals were more degraded or completely degraded than the crosslinked crystals by day 4. Interestingly, the trend in degradation broke for the crosslinked crystals at 430 µM DOX. At this high concentration, the crosslinked crystals became dark red globular structure instead of becoming completely degraded, while the non-treated crystals left behind skin-like shells.

Chapter 4.2.2: Incorporation of DOX into 13mer crystals at 4˚C

The NOR crosslinked and non-treated crystals were additionally soaked at 4˚C to evaluate whether the decrease in temperature would mitigate the degradation experienced at room temperature (Figure 4.3). It was found that soaking the crystals at 4˚C had a positive effect on crystal stability. For example, at room temperature, the non-treated crystals and the NOR crystals at 107.5 µM were completely dissolved by day 3 (Figure 4.2), except for crosslinked crystals at 430 µM DOX, but at 4˚C, the crystals in both conditions were still present at D6 with minimal degradation. Rounding of the crystals was still seen for both crystal sets at a higher concentration of 480 µM DOX.

An interesting observation was the lack of a clear border on the edge of the crystals between the crystals at 480 µM and the crystals at lower concentrations below 107.5 µM (Figure 4.4A). When the crystals without borders were broken, they smeared like jelly instead of fragmenting as the crystals normally do (Figure 4.4B), prompting us to refer to these as “gel”

crystals. When we transferred these gel crystals to a new buffer, the DOX did not visibly diffuse out, in contrast to the non-gel crystals. This gel state was seen only at higher concentrations of DOX, above 136.10 µM. In addition, varying the concentration had an effect on how fast the gel state was reached and how likely the crystals were to retain their original morphology (Figure 4.3B). Non-treated crystals incubated at DOX concentrations between 322.5 µM and 136.10 µM were able to achieve the gel state with no degradation and retained the hexagonal morphology. Interestingly, the crosslinked crystals at DOX concentration above 136.10 µM achieved this state earlier, by day 1. The non-treated crystals on the other hand reached this state anywhere between day 3 and day 9.

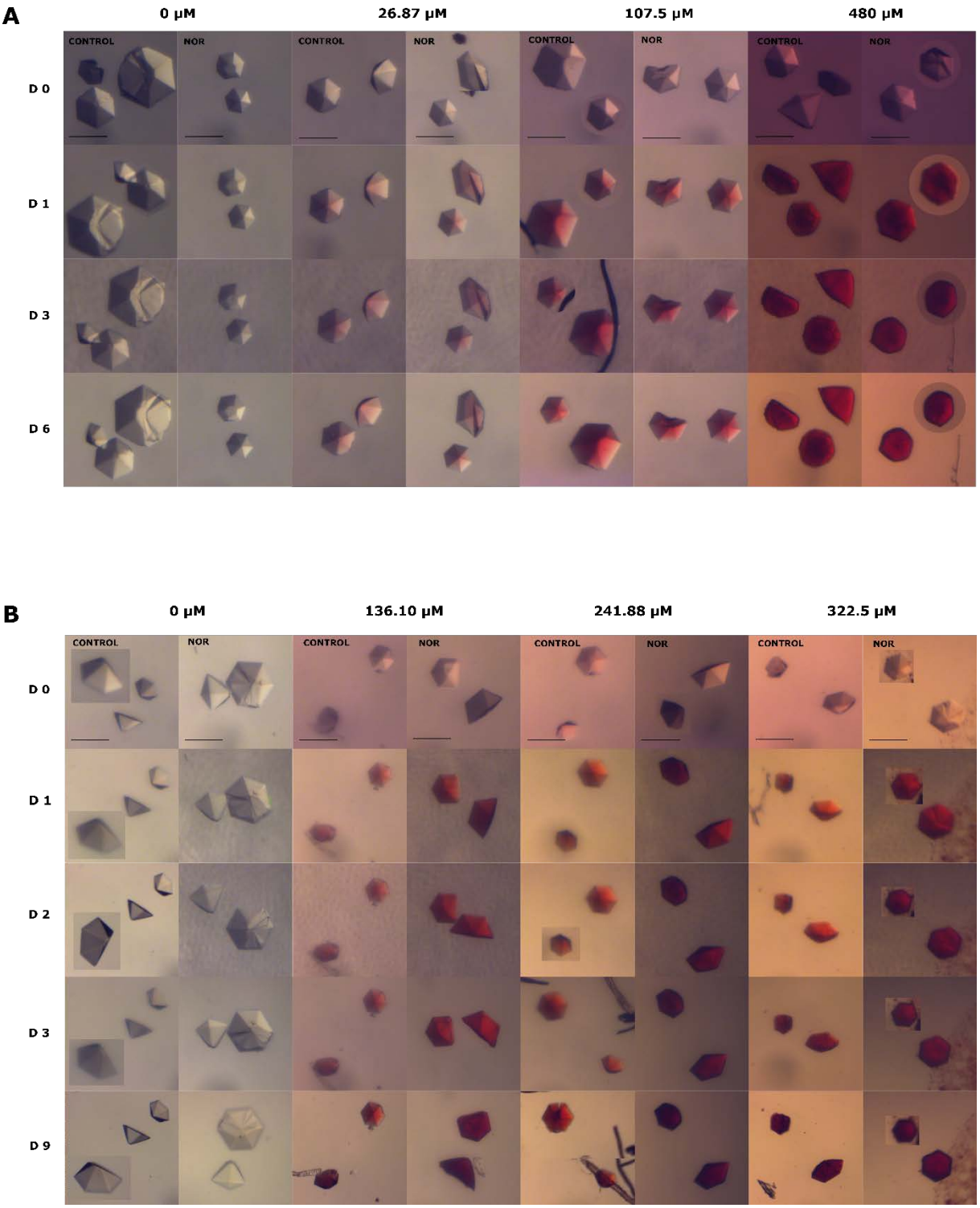

Figure 4.3. Light microscope images of crystals soaked in DOX at 4˚C. Non-treated crystals (Control) and NOR-treated (NOR) crystals to buffer (10 mM Tris HCl pH 7.5 and120 mM $C_2H_2MgO_4$) with DOX, concentrations above the columns, at day 0 (D0). **A.** Crystals were incubated DOX concentration between 0 and 480 µM. **B.** Crystals were incubated at more narrow DOX concentration range 136.10 µM- 322.5 µM, and 0 µM. Scale bars, 70 µm.

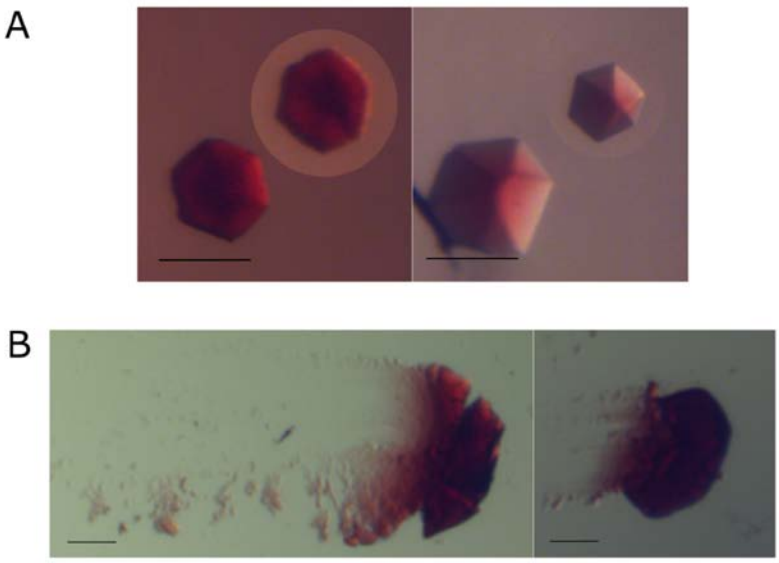

Figure 4.4. Light microscope images of gel and non-gel crystals. **A.** Gel crystals without clear borders (left) and non-gel crystals with clear borders (right), and **B.** broken gel crystals.

Chapter 4.2.3: Effect of magnesium on doxorubicin in corporation

We hypothesized that the gel state was the result of instability of the crystal lattice, because the gel state was only achieved at higher concentration of DOX. At higher DOX concentration, there would be more DOX intercalating into the crystal, leading to disruption in the stacking interactions, thereby destabilizing the overall lattice structure. Normally, instability of the crystal lattice would result in degradation until nothing was left, as seen with the crystals at DOX concentration below 107.5 µM, but the instability caused by high DOX intercalation led to the formation of the gel state.

To test this, we explored the correlation between magnesium concentration and the transition into the gel state (Figure 4.5). Magnesium plays an essential role in the stability of DNA nanostructures; the positive charge shields the negatively charged DNA phosphate backbone in order for DNA backbones to be in close proximity to one another. Therefore, an

increase in magnesium concentration would strengthen the lattice backbone interaction, and a decrease would weaken the lattice contact and facilitate the intercalation of DOX. We incubated the NOR 13-mer crystals (B7) and its complementary crystals (A2, A3 and B6), where there are permutations in the Crick-Watson base-pair (Figure 4.5A), in 322.5 µM DOX, in magnesium concentration ranging from 50 mM to 200 mM magnesium formate.

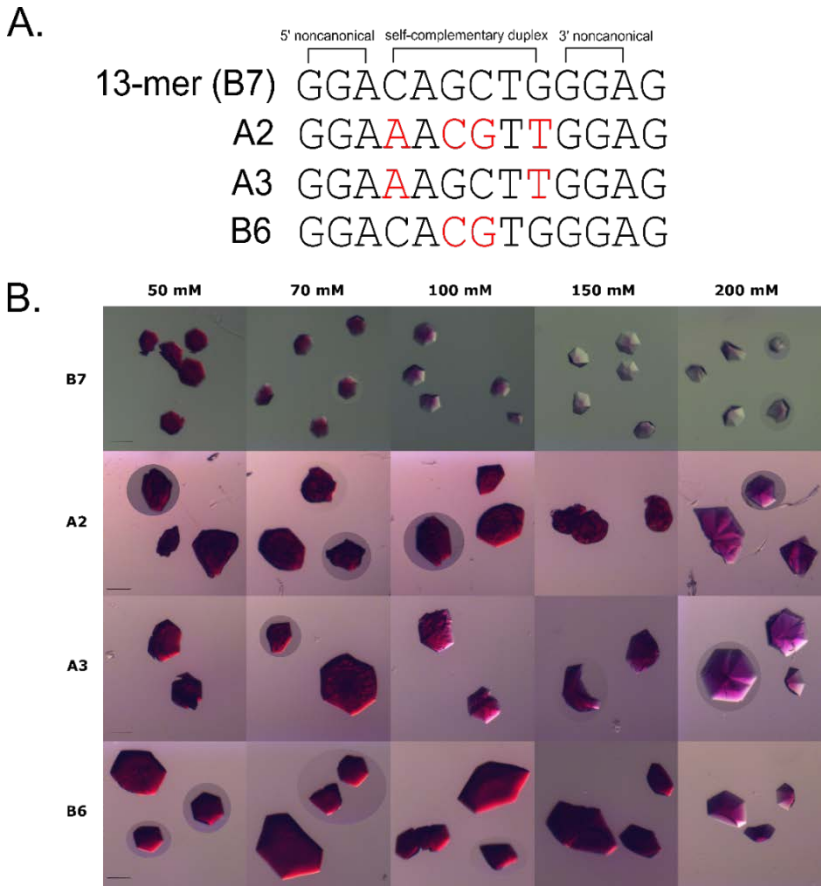

Figure 4.5. Effect of magnesium on formation of gel crystals. **A.** Sequences of oligonucleotides used in this study. Sequences are vertically aligned, with positions in red indicating sequences differences relative to the 13-mer DNA. **B.** Effect of different $C_2H_2MgO_4$ concentrations on DOX incorporation. Light microscopes images of different complementary 13-mers at different $C_2H_2MgO_4$ concentrations. Listed left of the images are the different 13-mers. The different $C_2H_2MgO_4$ concentrations are listed above the images. Scale bars, 70 µm.

We observed an inverse relationship between the level of DOX incorporated and the magnesium concentration. The level of DOX observed within the crystals gradually dropped as the magnesium concentration was increased; the crystals lost their gel state and a clear band was seen along the edge of the crystals (Figure 4.5B). For the 13-mer (B7) crystal set, we saw a gradual decline in the intensity and penetration of the DOX as the magnesium concentration increased. The complementary crystals showed a similar pattern but oddly, the gel state was reached at a higher magnesium concentration than B7. This suggests that the differences in the Crick-Watson base pairs may play a role in the stability of the crystal lattice and therefore how easily DOX intercalates into the crystal.

In conclusion, the gel state was affected by the stability of the crystal lattice as shown by the trend between DOX incorporation and magnesium concentration. The information allowed us to understand how the gel state was achieved and how to better control the onset of the gel state. The ability to control the onset of the gel state would be beneficial, because it appeared to have higher DOX incorporation than the non-gel state, allowing us to increase the load capacity of the 13-mer crystal.

Chapter 4.2.4: Loading capacity and retention of doxorubicin inside 13-mer crystal

We used confocal microscopy to confirm and further evaluate DOX incorporation and retention. The crystals at lower DOX concentration, 107.5 μM and below, showed that the incorporation of DOX was positively correlated to the initial DOX concentration the crystals were soaked in; the higher the DOX concentration, the higher the fluorescent intensity. NOR crystals incubated in 6.72 μM and 1.68 μM DOX for four days showed that the NOR crystals incubated 6.72 μM had a higher intensity than the ones soaked at 1.68 μM (Figure 4.6 C,D). Also, NOR crystals in 107.5 μM DOX at 4˚C had a higher intensity than 26.87 μM (Figure 4.7

B,C). Crosslinking the crystals also increased the intensity relative to the non-treated crystals. NOR crystals incubated at 107.5 µM at room temperature for 3 hours and 107.5 µM DOX incubated at 4˚C had a higher intensity than their non-crosslinked counterparts in the same conditions (Figure 4.6 A,B and 4.7 A,B).

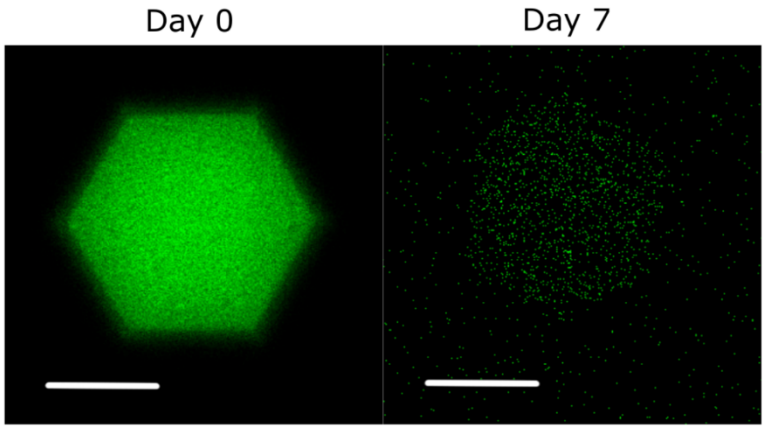

	Initial Intensity	% Intensity After 7 Days
A	87.71	5.35%
	71.74	5.05%
B	127.38	7.42%
	112.58	8.23%
C	92.01	0.34%
	66.66	0.56%
D	50.21	67.52%
	44.27	70.66%

Figure 4.6. Confocal microscopy images of non-gel crystals. The table to the right shows the initial intensity of the crystals, and the percentage of intensity that remained after 7 days for **A.** non-treated and **B.** cross-linked crystals soaked in 107.5 µM DOX for 3 hrs at RT, and cross-linked crystals soaked in **C.** 6.72 µM and at **D.** 1.68 µM incubated for 4 days. 50 µm. Day 7 image has been enhanced.

Interestingly, the non-gel crystals and the gel crystals showed different apparent levels of incorporations. Z-stack images of the non-gel crystals showed DOX was incorporated throughout the crystal (Figure 4.6 and 4.7). In contrast, the gel crystals, which had visually showed higher level of incorporation based on the intensity of the red coloration, showed uneven DOX distribution by fluorescence, including large areas within the center of the crystals that were not fluorescent (Figure 4.8). Importantly, the lack of intensity does not necessarily correlate to the absence of DOX. Quite the opposite, DOX experiences self-quenching at high concentration of >10 µM [98]. Fluorimetry data further supported that gel crystals had a higher loading capacity for DOX than the non-gel crystals. The fluorescent intensity of the dissolved gel crystals of similar dimensions was six-fold higher than the non-gel crystals (Figure 4.9). The high fluorescent

intensity of the gel crystals seen with the fluorimeter confirmed that the lack of intensity seen with confocal microscopy was due to self-quenching.

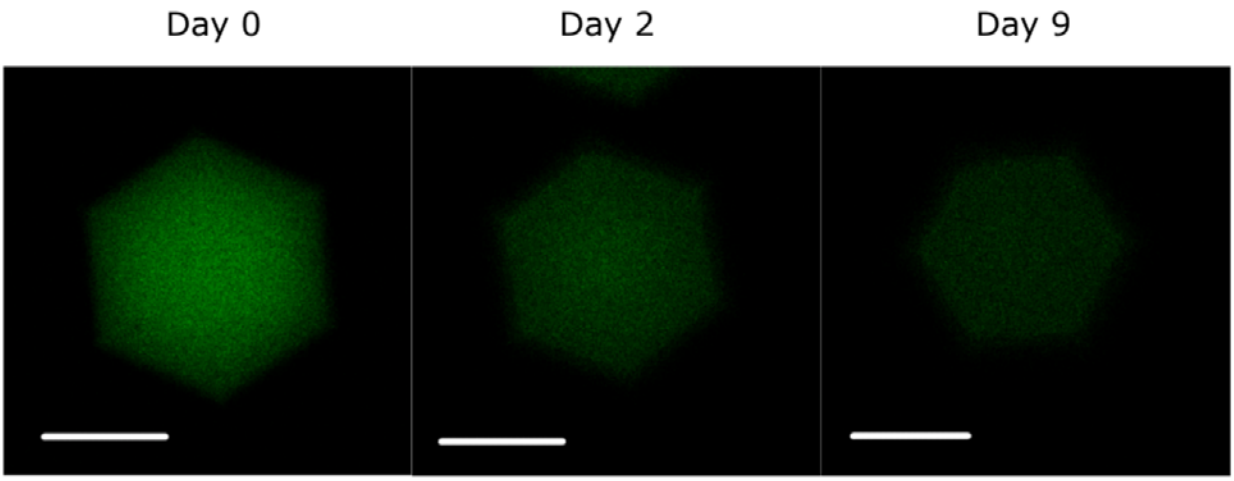

	A		B		C	
Initial Intensity	37.2	111.4	118.15	129.8	36.98	40.35
Percentage of Intensity Remaining						
D0	100%	100%	100%	100%	100%	100%
D2	53.87%	38.54%	36.85%	29.06%	41.32%	37.13%
D9	48.66%	18.75%	20.26%	19.58%	28.85%	X

Figure 4.7. Confocal microscopy of DOX diffusion of non-gel crystals. Table shows initial intensity of the crystals and percentage of intensity that remained at day 0, 2 and 9 for **A.** non-treated and **B.** NOR crystals in 107.5 µM DOX incubated at 4˚C for 7 days, and **C.** NOR crystals in 26.87 µM DOX at 4˚C for 7 days. Scale bars, 50 µm. Day 2 and day 9 images has been enhanced to show fluorescence.

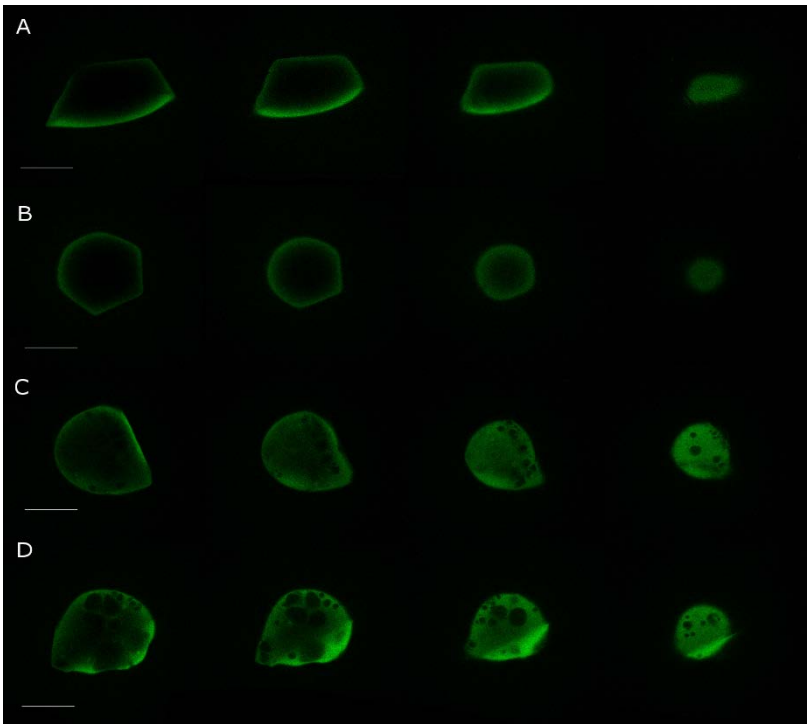

Figure 4.8. Confocal microscopy images (Z-stack) of NOR-treated gel crystals. The crystals were incubated at 322.5 µM (**A** & **B**) and 136.10 µM (**C** & **D**). Scale bars, 50 µm.

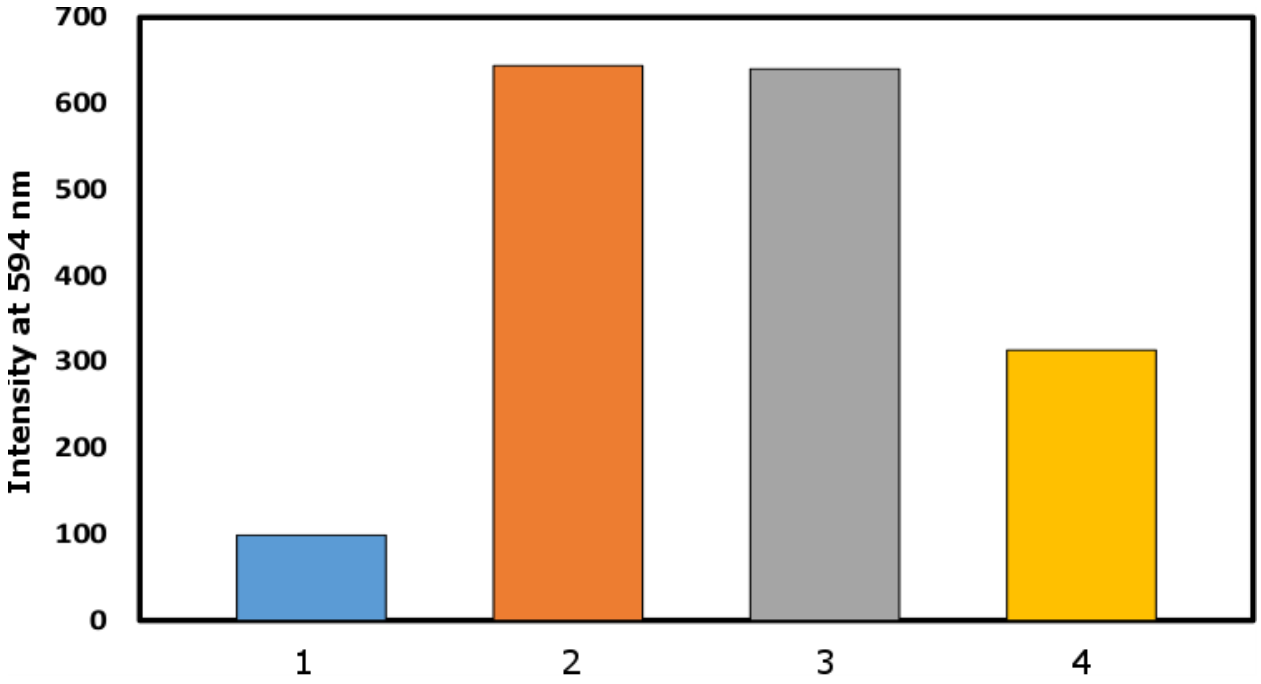

Figure 4.9. Fluorimeter measurement of DOX-incorporated crystals. Fluorescent intensity of ~25 dissolved **1**. Non-gel crystals, **2 and 3.** gel crystals and **4.** polydopamine-treated crystals.

In addition to the high load capacity, the gel crystals retained DOX better than the non-gel crystals. When both crystals were transferred to fresh buffer, we saw that the DOX in the non-gel crystals appeared to diffuse out under the light microscope while the gel crystals retained the DOX. This result is interesting, because the gel crystals may have had better retention due to instability of the crystal lattice. This could be the result of lattice deformation, which resulted in sealing off the solvent channel and trapping the DOX inside, hence, improving DOX retention.

The retention of DOX inside the non-gel crystals was evaluated using confocal microscopy, and the retention of DOX inside the gel crystals was evaluated using fluorimetry. The same crystals imaged before using confocal microscopy were imaged 7 days later in fresh buffer solution. The majority of the crystals showed more than 90% decrease in intensity (Figure 4.6). A second set of crystals that were incubated with DOX at 4˚C (Figure 4.7) showed most of the diffusion occurred early on, with an average reduction of 40% in intensity by day 2, and 70% reduction in intensity by day 9. The non-linear diffusion of the DOX out of crystal could indicate different levels of intercalation within the lattice.

Fluorimetry data showed that the DOX diffused out of the gel crystals slower than the DOX diffused out of the non-gel crystals. An average of 25 gel crystals were incubated at 4˚C overtime and samples were collected from the supernatant at day 0, day 3, day 7, day 10 and day 14 (Figure 4.10). At the end time point, we dissolved the crystals and collected the samples for measurement. The gel crystals did not indefinitely prevent the DOX from diffusing from the gel crystals, but it did reduce the amount that diffused out of the crystal lattice relative to the non-gel crystals. At day 3, an average of 26.2% of the DOX had escaped from the gel crystals. The total DOX lost plateaued off considerably afterwards, with an average of 43.62% lost at day 10 and

47.66% at day 14. Overall, the crystals retain on average, 52.34% of their original load by day 14.

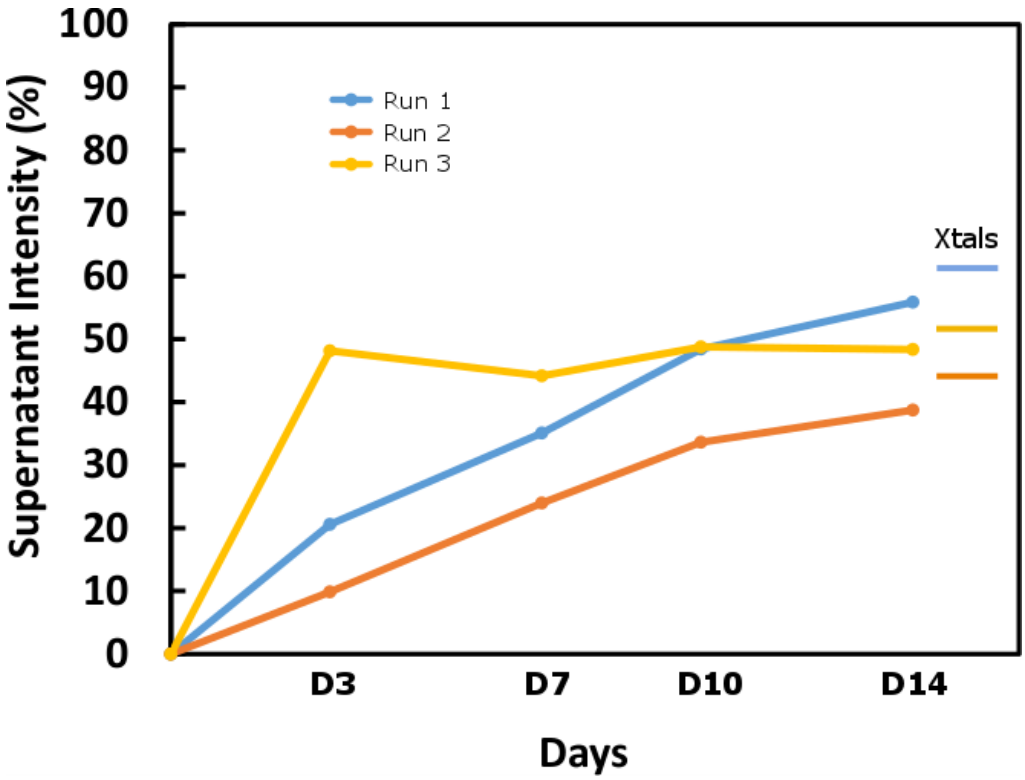

Figure 4.10. Measurement of DOX diffusion out of ~25 gel crystals over time. We collected samples from the supernatant over time and measured the intensity, shown here as the percent of the total intensity measured. The horizontal line indicates the intensity of the ~25 gel crystals dissolved after 14 days as a percent of the total intensity measured.

Chapter 4.2.5: Layer-by-layer assembly on doxorubicin-incorporated crystals

We performed layer-by-layer (LBL) assembly on the DOX-incorporated crystals to evaluate whether the addition of DOX will affect the assembly process. The non-gel and gel crystals were layered with 13-mer oligomers (with and without fluorescein attachment at 3'end) and polydopamine (PDA). A new layer formed on both crystal types. The new crystal layer differed in structure depending on how ordered the core crystal was. An ordered layer formation occurred on the non-gel crystals similar to non-DOX crystals; the DOX did not affect the ordered assembly of the new layer (Figure 4.11). On the other hand, the new layer on the gel crystals

resembled an agglomeration of the oligomers whether than an ordered crystal layer (Figure 4.12). It was not surprising that the state of the new layer reflected the level of order of the core since LBL assembly with oligomers relies on order incorporation into the existing framework of the crystals. The disordered crystal layer on the gel crystals may be a representation of how the core crystal was ordered and confirmed that the DOX had destabilized the ordered crystal lattice. Subsequently, dopamine was successfully deposited on the gel crystals, creating a dark PDA coat similar to what was seen with non-DOX crystals.

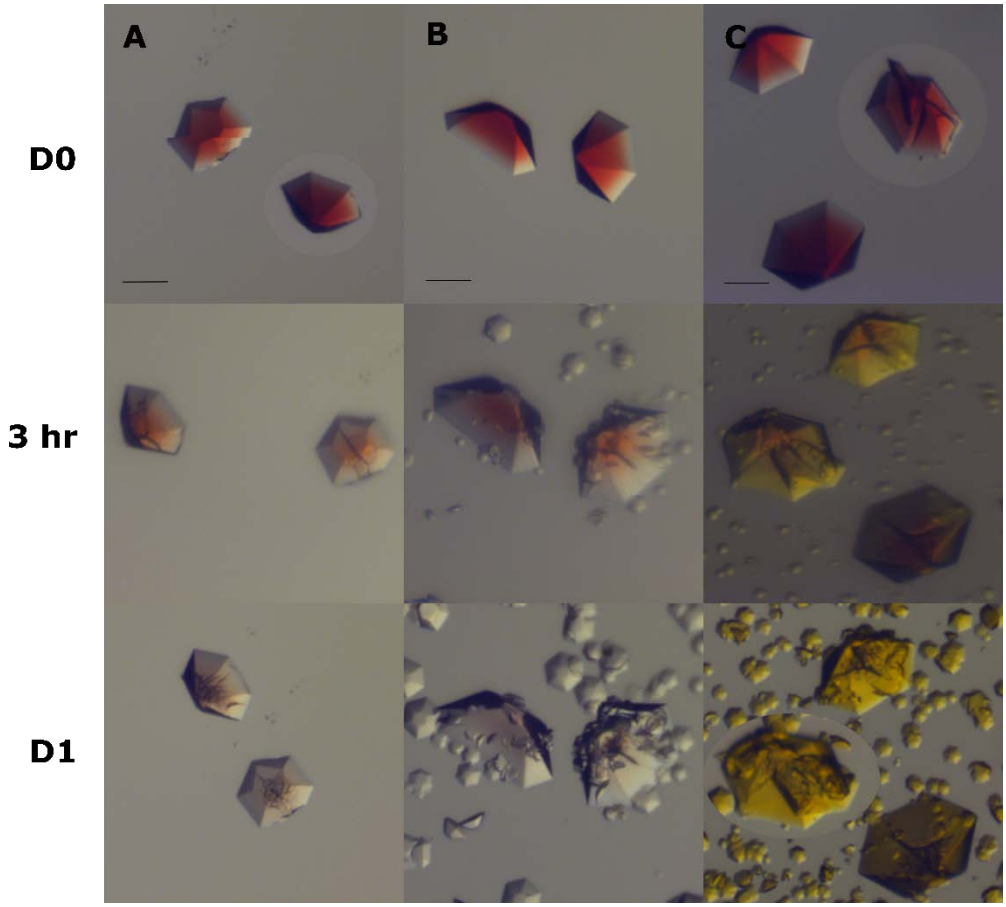

Figure 4.11. LbL assembly on non-gel crystals. Light microscope images of DOX-incorporated crystals in fresh crystallization buffer with **A.** no additional layer added, **B.** layered with 13-mer and **C.** layered with 13-mer-fluorescein. Scale bars, 70 µm.

Next, we evaluated whether the additional layer on the non-gel crystals and gel crystals would improve retention of DOX within crystals. The oligomer layer on the non-gel crystals did not have any effect on the retention. The lack of retention could be attributed to the diffusion of the DOX outpacing the layer formation or since the new layer is forming via ordered assembly, the solvent channels are continued from the core, thereby providing a route for the DOX to diffuse out. Additionally, the new PDA did not improve DOX retention of the gel crystals. The percent of DOX retained (~70%) after seven days was equivalent to the non-PDA gel crystals. Oddly, the amount of DOX measured in the PDA coated gel crystals were significantly lowered (~50 %) than the non-PDA versions (Figure 4.13). The DOX could have been stuck to the PDA coat, which did not dissolve at higher temperatures. The additional layer did not improve retention, but the demonstrability of LBL assembly on the non-gel and gel crystals provides the opportunity for specific functionalization of the crystal exterior.

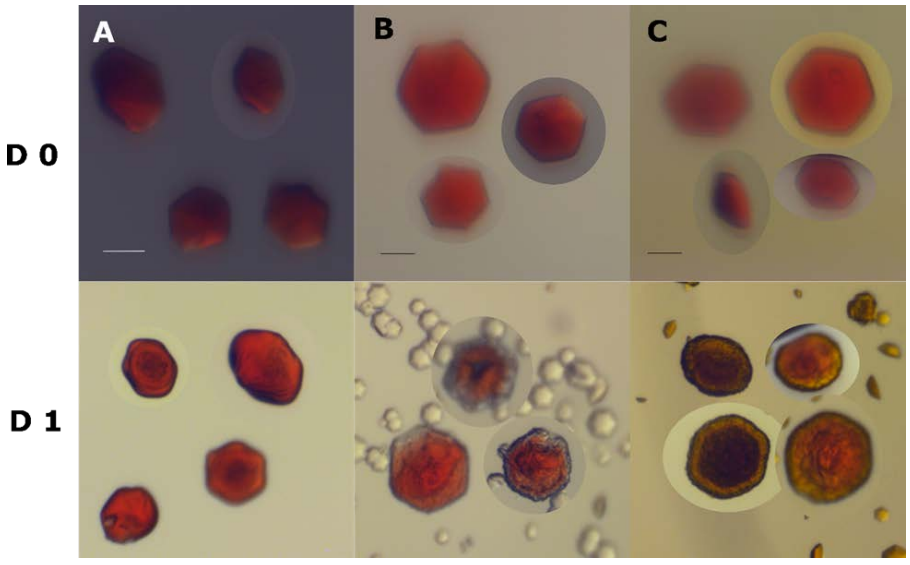

Figure 4.12. LbL assembly on gel crystals. Light microscope images of gel crystals in fresh crystallization buffer with **A.** no additional layer added, **B,** layered with 13-mer and **C.** layered with 13-mer-fluorescein. Scale bars, 70 μM.

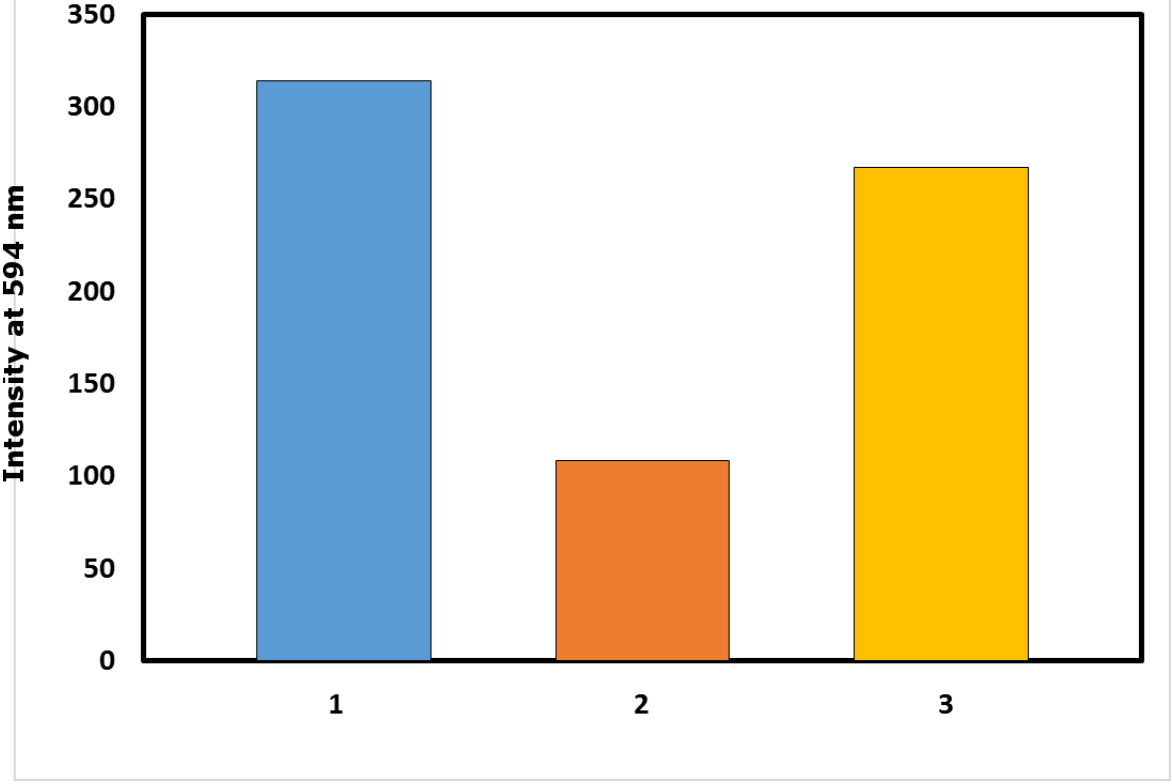

Figure 4.13. Retention of DOX in PDA coated crystals over time. Fluorimetry measurement of **1**. Dissolved ~25 PDA coat crystals at D0; **2.** Supernatant after 7 days; **3.** dissolved ~25 crystals PDA coat after 7 days. Scale bars, 70 µm.

Chapter 4.3: Conclusion

For the first time, we incorporated doxorubicin, a small drug molecule, into a 3D continuous DNA crystal. The 3D DNA crystal contains solvent channels running throughout the lattice structure. DOX can be incorporated into the crystal through intercalation and sealed within the solvent channels while most other DNA nanostructures incorporate DOX via intercalation. The instability caused by the DOX intercalation resulted in the transition of the uniform crystal structure into a gelatinous or glass-like structure instead. The solvent channels become sealed off and as a result, traps the DOX inside and therefore increasing the loading

capacity. The new gel structure increased retention of DOX and loading capacity compared to the crystal structure. Future task can focus on exploring the gel states compared to the crystal state. Tools such as atomic force microscopy (AFM) can measure the stiffness of a sample[99] and can be used to compare the difference between the crystal and gel state.

The DNA crystal is on the path as a drug delivery device or in vivo utilization. The loading of DOX into the crystal is simple, no modifications or coupling steps are necessary. Furthermore, the ability to grow an additional layer on top of the DOX crystals provides the advantage of tethering molecules[30] to the surface. The ability for secondary surface functionalization can increase target specificity and uptake. The uptake can be further improved by the ability to program the morphology of the crystal[39]. The process of loading a guest molecule into the crystals can be expanded to include fluorescent probes for bioimaging or *in vivo* labeling, or cytosine-phosphate-guanine (CpG) sequences to act as an immunostimulant.

Chapter 4.4: Materials and Methods

Chapter 4.4.1: Oligonucleotide synthesis and purification

The oligonucleotides were ordered from IDT (Integrated DNA Technologies) or were synthesized on an Expedite 8090 DNA synthesizer (PerSeptive Biosystems) with reagents from Glen Research (Sterling, VA) using standard phosphoramidite synthesis and deprotection. Oligonucleotides were gel purified and electroeluted as previously described[20] before dialysis against deionized water.

Chapter 4.4.2: Crystallization

Oligonucleotides were crystallized by sitting drop vapor diffusion. 2 µL of 200 µM 13 nucleotide oligomer and 1 µL water were added to the sitting drop, followed by 1 µL of crystallization buffer (10% 2-methy-2,4-pentanediol, 120 mM magnesium formate, 50 mM

lithium chloride). Drops were equilibrated against 300 µL of crystallization buffer. Crystal trays were incubated overnight at 22˚C.

Chapter 4.4.3: Incorporation of DOX

The crystals were washed in 100 µL of soaking buffer (10 mM Tris HCl pH 7.5 and 120 mM magnesium formate) for 5 mins. The crystals were then transferred by nylon loop to 5 uL of soaking buffer and 5 uL of DOX (272.2 µM – 960 µM).

Chapter 4.4.4: Layer-by-layer assembly

DOX crystals were washed in 100 µL crystallization buffer prior to use. DOX were transferred by nylon loop to a sitting drop containing 2 µL of crystallization buffer. 1 µL of 175 µM 13-mer oligomer supplemented with or without 25 µM fluorescein-labeled 13-mer was then added. The sitting drop was then equilibrated against 300 µL of crystallization buffer and incubated overnight at 22˚C.

Chapter 4.4.5: Dopamine Polymerization on DOX crystals

10 uL of 2x of PDA formation solution (10 mM Tris HCl pH 7.5, 60 mM magnesium formation, 10 mM dopamine HCl) solutions above were added into 10 uL of 120 mM magnesium formate in 24 well crystal trays containing DOX crystals and incubated overnight.

Chapter 4.4.6: Visualization and measurements

Light microscope crystal images were taken of the crystals in the sitting drop on a stereo microscope with an attached CCD camera. The fluorescein-incorporated layered crystals were imaged with a Leica SP5X confocal microscope. Prior to visualization, crystals were washed in 100 µL crystallization buffer and then transferred to a 200 µL crystallization buffer on a 35 mm glass bottom culture dish with 14 mm microwell. The fluorescein layer was visualized by excitation at 488 nm. Z-stack images were collected every 1 µm. Measurements and 3D

reconstructions were performed in ImageJ[100] and Leica Application Suite (LAS) AF. Intensity measurements were the mean intensity of a set region of interest (ROI).

Chapter 4.4.7: Fluorimeter measurements

~25 DOX gel crystals were transferred to 100 µL soaking buffer and then to 34 µL soaking buffer. 4 µL was removed for day 0 (D0) sample and brought up to 100 µL. 4 µL was also collected at D3, 7, 10 and 14.

At the end, the ~25 DOX gel crystals were washed with 100 µL soaking buffer. The crystals were then incubated at 37˚C until completely dissolved. Next, the solution was transferred to a cuvette and brought up to 100 µL. The sample was read on the FL-4500 Spectrophotometer (ROM Vers 4000 05). The excitation wavelength was 488.0 nm and emission was read 520 – 680 nm. The wavelength with the highest emission was determined and the intensity taken at that chosen wavelength.

Chapter 5: Designed DNA Crystal Habit Modifiers

*This chapter is derived from "Zhang, D. & Paukstelis, P. J. Designed DNA Crystal Habit Modifiers. *J. Am. Chem. Soc.* **139,** 1782–1785 (2017)."

Chapter 5.1: Introduction

A significant portion of the DNA crystal design field has been focused on altering and understanding properties in existing designs[29,31,34], or identifying new DNA motifs to expand structural diversity[35,36]. Inherently, these approaches interrogate the nanoscale properties of the crystals in the form of intermolecular contacts that enable crystallization. However, very little has been done to control macroscopic properties of existing DNA crystals.

One of the fundamental macroscopic properties of crystals are their morphologies, or crystal habits. The habit often suggests the underlying periodicity and symmetry of the crystal lattice, and many crystal forms can have more than one habit type. Crystal habit modifiers alter crystal morphology and are commonly used to enhance certain crystal features for particular applications[101–105], and are important in biomineralization processes[106,107]. Habit modifiers may act in a variety of ways, including thermodynamically by changing surface energies of selective crystal faces, or through kinetic changes that may impact prenucleation, nucleation, and growth[108]. A number of models for the mechanism of habit modification for organic and biologically-relevant inorganic crystals have been proposed[109–112]. However, in most cases, habit modifiers are found empirically through selective addition during the crystallization process. This had limited predictive power as to how the macroscopic crystal properties may change. This is compounded for macromolecular crystals where there are many more weak intermolecular lattices contacts necessary for maintaining crystal integrity[113]

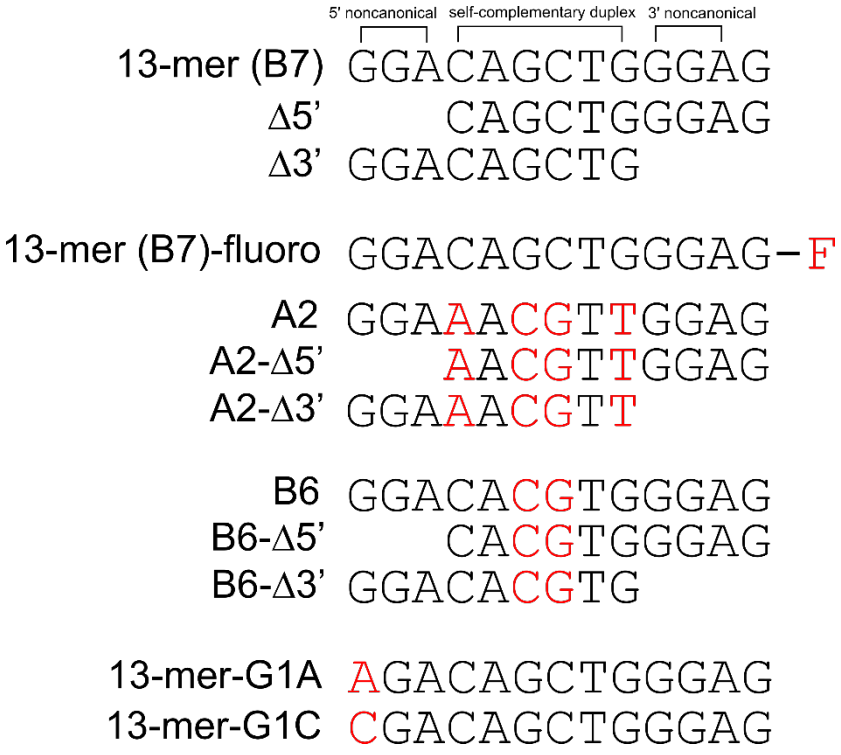

Figure 5.1. Sequences of oligonucleotides used. Sequences are vertically aligned, with positions in red indicating sequences differences relative to the 13-mer DNA. F, fluorescein.

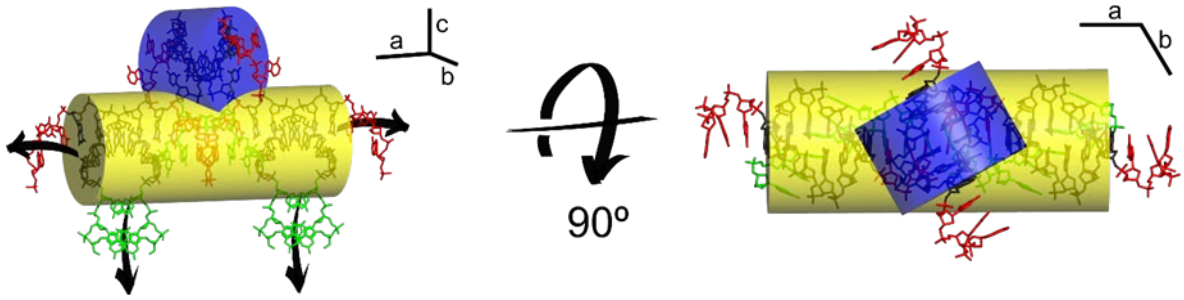

Figure 5.2. Relative orientations of the duplex segments and noncanonical base pairs in the 13-mer crystal. Duplex regions are overlayed by semi-transparent cylinders. The yellow cylinder spans two duplex segments that are coaxially stacked through noncaonical base pairs between 5' (green) and 3' (red) nucleotides. The blue cylinder spans a single duplex segment that connects to the two duplexes of the yellow cylinder through its 5' nucleotides. Arrows in the image on the left represent the direction the terminal nucleotides exit the duplex segments. All duplex helical axes are orthogonal to the c cell axis, which positions the 3' nucleotides along the a and b cell axes. The 5' nucleotides exit the duplex segments down the c cell axis.

The high resolution crystal structures of the non-canonical or 13-mer crystals and a number of closely related oligonucleotides sequences[31] allowed us to examine lattice features that could be manipulated to potentially alter the macroscopic properties of the crystals. One notable feature was that the hexameric duplex regions were aligned with their helical axes orthogonal to the *c* cell axis (Figure 5.2). This corresponds to the six-fold symmetry axis in the hexagonal crystal system, leading to the duplexes being layered perpendicular to this axis while being rotated 120º with respect to flanking layers. The ~2 nm spacing between duplexes within each layer creates a series of solvent channels that run through the crystal in multiple directions (Figure 1.1B). The 5' nucleotides involved in the noncanonical interactions (G_1-A_3) exit from the duplex helical axis down the *c* axis, while the 3' most nucleotides (G_{10}-G_{12}) extend out of the helices along the *a* and *b* cell edges (Figure 5.2). This led us to explore the possibility of disrupting either the 5' or 3' most nucleotides to influence crystal growth rates along or orthogonal to the six-fold symmetry axis. We designed 5' and 3' truncated versions of the oligonucleotide that could still form Crick-Watson base pairs with the full-length strands, but would be deficient in forming the noncanonical base pairs (Figure 5.1). We reasoned that these truncated oligonucleotides, designated Δ5' and Δ3', could selectively 'poison' crystal growth and function as crystal habit modifiers.

Chapter 5.2: Results and Discussion

Chapter 5.2.1: Crystallization of 13-mer with poison oligomers

The poison oligomers were evaluated by adding increasing concentrations of Δ5' or Δ3' to crystal drops containing the full-length 13-mer. We observed distinct concentration-dependent crystal habit changes from the starting hexagonal unipyrimidal crystal with both poison oligomers (Figure 5.3). Addition of the Δ5’ poison resulted in crystals with preferential growth orthogonal to

the *c* cell axis, resulting in a change to a tabular habit (Figure 5.3B). This transition was dependent on Δ5' concentration, with the change discernible at the lowest concentrations tested. At higher concentrations, crystals appeared as 2D hexagons, and at even higher concentrations, crystals did not grow. Addition of Δ3' also generated a new set of concentration-dependent crystal habits (Figure 5.3C). At low concentrations, crystals appeared as hexagonal pyramids with slightly elongated points. With increasing Δ3' concentration, the elongated points became discernible hexagonal growth that developed to form "bow-tie" shaped crystals. At the highest concentrations that still gave crystals, the crystals became uniform acicular hexagonal columns. Interestingly, the two poison oligomers showed different concentration dependencies. Habit changes were significantly more sensitive to presence of Δ5', possibly reflecting a greater affinity between this oligomer and the 13-mer, or different propensities for stable incorporation into the lattice. Crystals grown in the presence of both Δ5' and Δ3' favored tabular crystal formation until Δ3' concentrations were ~20-fold excess, at which time they formed crystals with intermediate morphologies that was also dependent on the relative concentration of 13-mer and poison strands (Figure 5.4). This suggests that the addition of both poison oligomers may allow fine-tuning of the crystal shapes.

To determine if partial disruption of optimal base-pairing in the non-canonical region would act as a crystal habit modifier, G_1 was converted to A (13-mer-G1A) or C (13-mer-G1C) (Figure 5.1). The alteration would disrupt base-pairing with G10 and base-stacking with C4 of a different strand (Figure 1.1A). The 13-mer crystallized with high concentration of 13-mer-G1A or 13-mer-G1C yielded tabular crystals similar to 13-mer with Δ5' (Figure 5.5), although there was a difference in the concentration required to achieve the tabular crystals between 13-mer-G1A or 13-mer-G1C and Δ5'. The 2D tabular crystals formed with Δ5' were seen only when the poison concentration was 100x lower than the 13-mer. The tabular crystals were seen with 13-mer-G1A

or 13-mer-G1C when the concentration was 1.5x higher than the 13-mer. Additionally, the tabular crystals was more elongated along the c-axis even with the higher concentration of poisons presented and were not flat 2D tabular crystals as it was with the Δ5' (Figure 5.3). The higher concentration of the G1 poisons required to bring about the same morphological changes as the Δ5' suggested that the level of disruption in the non-canonical region reflect the intensity of the habit modifying effect the poisons would have.

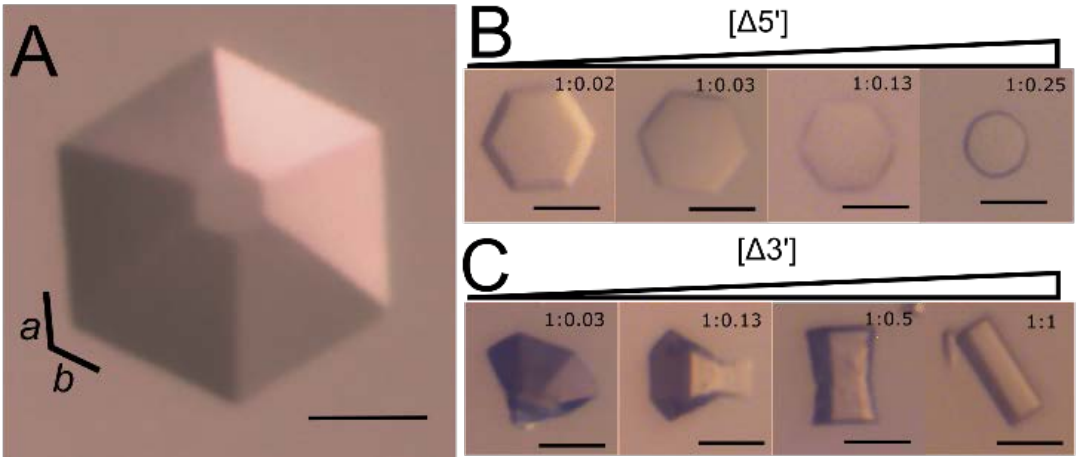

Figure 5.3. Poison oligomers as crystal habit modifiers. The ratios at the top of each corner for B and C indicates the relative concentration of the 13-mer (final concentration 100 μM) to the poison oligomer. **A**. Unipyrimidal crystals in the absence of habit modifiers. Relative orientation to unit cell axes is shown. **B.** Tabular habit modification in the presence of increasing concentration of Δ5' poison. **C.** Acicular or columnar habit modification with increasing concentration of Δ3' poison. Scale bars, 70 μm.

Several lines of analysis suggested that the ability for Δ5' and Δ3' to function as habit modifiers is dependent on their ability to base pair with the 13-mer directly, and/or their propensity to be integrated into the growing lattice. Therefore a complementary 13-mer sequence[31] with alternations made to the Crick-Watson region (Figure 5.1) should show the same habit modification trends using poison oligonucleotides with sequences complementary to its duplex region (Figure 5.6 A, D, G, J, M and P). The 13-mer complementary sequences have the same non-canonical base-pairing regions, but differ in the Crick-Watson base-pairings[31]. The

complementary sequences used were A2 and B6, with A2 having a four-nucleotide sequence difference to the B7 13-mer and the B6 having a two-nucleotide difference (Figure 5.1). If the truncations alone generated the morphology changes, crystallizing the complementary oligonucleotides with their corresponding poisons should result in similar morphological changes as the B7 set.

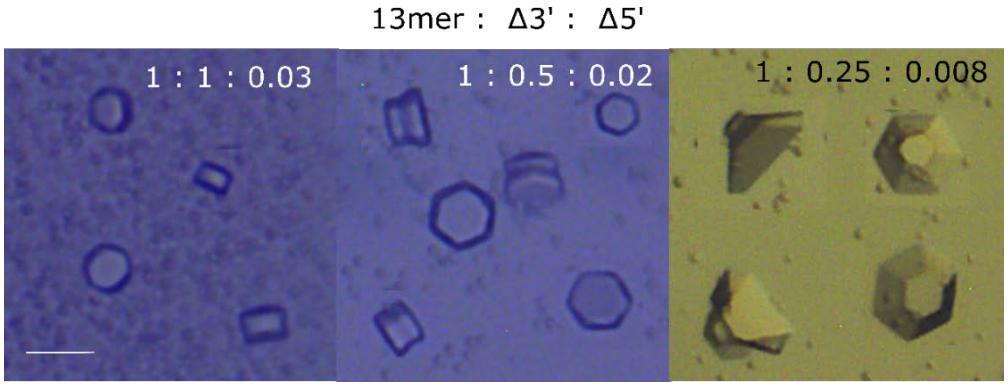

Figure 5.4. Light microscope images of 13-mer crystals grown in the presence of both Δ5' and Δ3'. The ratios indicate the relative concentration of 13-mer to Δ3' to Δ5'; the final concentration of the 13-mer was 100 µM. Scale bar, 70 µm.

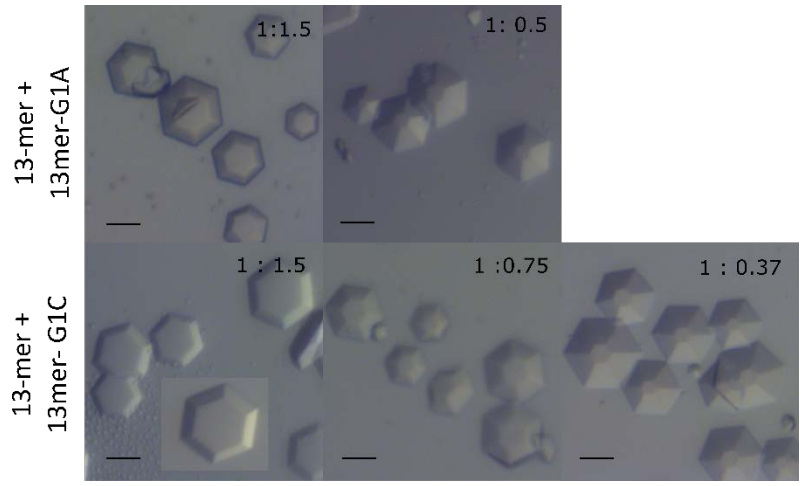

Figure 5.5. Light microscope images of 13-mer crystallized in the presence of 13-mer-G1A and 13-mer-G1C. Scale bar, 70 µm.

The A2 and B6 Δ5’ and Δ3’ truncations also acted as crystal habit modifiers on their 13-mer counterparts similar to B7 poisons (Figure 5.6A, D, G, J, M and P). Both sets of poisons likewise showed similar concentration-dependencies as the B7 poisons. Additionally, the B6 set generated a similar array of morphology as the B7 set; tabular crystals at low concentration of Δ5’ (Figure 5.6 G) and rod crystals at high concentrations of Δ3’ (Figure 5.6 J). On the other hand, the A2 set exhibited significantly different morphology pattern. At high Δ3’ concentrations, rounded rod-like crystalline structures formed that morphed into rounded hexagonal unipyramid crystals as the concentration was decreased until the sharp hexagonal unipyramid formed (Figure 5.6P). Furthermore, at high concentrations of Δ5’, spiked sphere crystals with pyramidal tips formed, and as the concentration of Δ5’ was lowered, the number of emerging tips decreased and increased in size until a single hexagonal unipyramid was formed (Figure 5.6 M). Overall, A2 and B6 Δ5’ and Δ3’ did act as crystal habit modifier on their corresponding 13-mer. However, the sequence dissimilarity in the Crick-Watson base-pairing region influenced how similar the morphology generated was relative to B7. B6 with two-nucleotide difference generated a morphology pattern similar to B7 while A2 with four-nucleotide difference was disparate to B7.

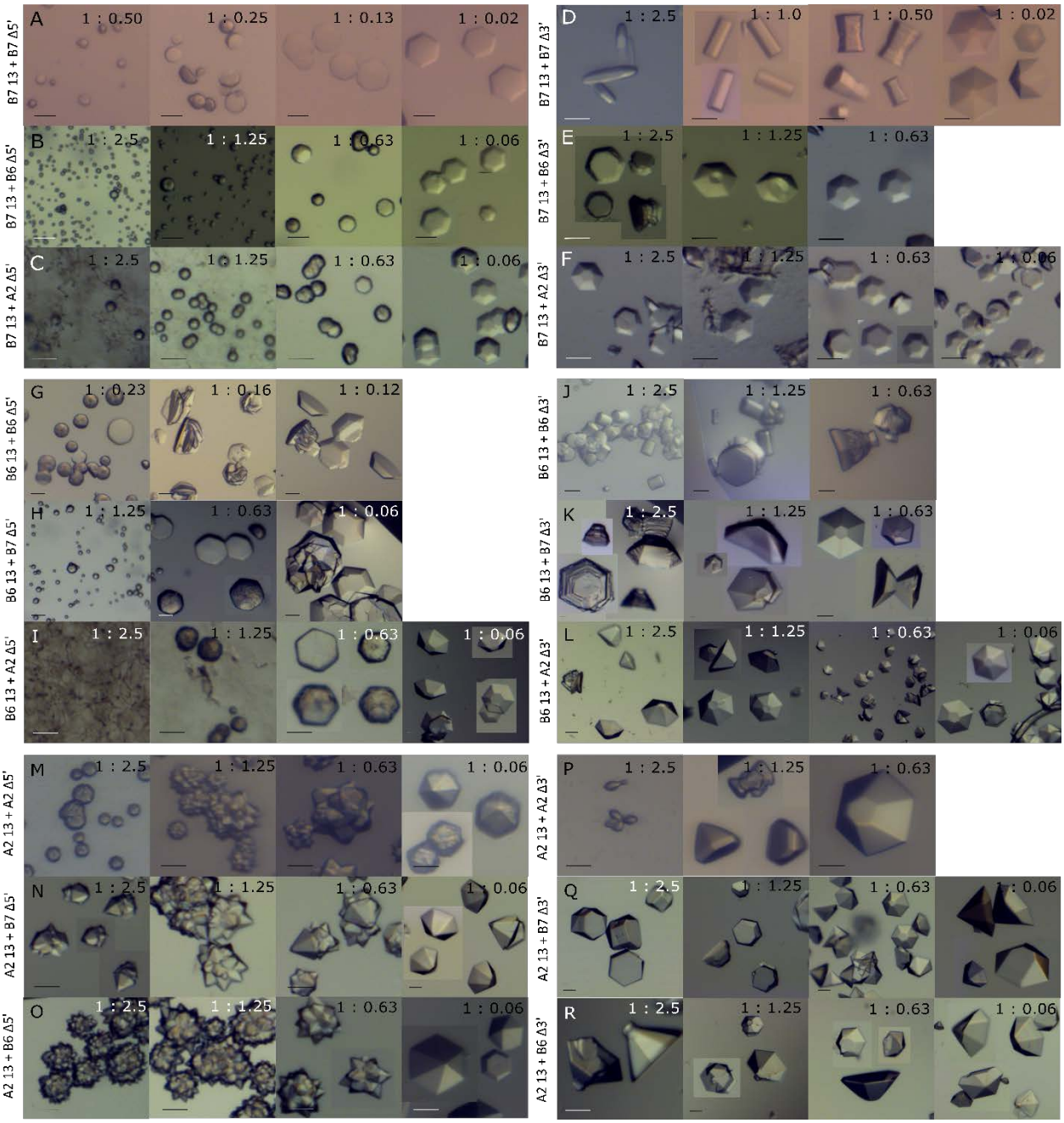

Figure 5.6. Habit modification and cross-reactivity of poison oligomers. Light microscope images of 13-mer oligomers crystallizes in the presence of their complementary and non-complementary poisons. The ratios at the top of each panel indicates the relative concentration of the 13-mer oligomer to the poison oligomer. Scale bars, 70 μm.

Next, we observed differences in cross-reactivity when using non-complementary poison strands (Figure 5.1). Δ3’ showed minimal cross-activity relative to Δ5’ (Figure 5.6 E,F,K,L,Q,R). Both (B7 13+B6-Δ3’) and (B6 13+B7-Δ3’) only showed impacts on crystal quality at high concentrations of the poison strands with no clear trends toward the formation of acicular crystals (Figure 5.6 E,K). Moreover, B7 and B6 with A2-Δ3’ showed minimum to no morphological changes at all (Figure 5.6F,L). The outlier was with A2 and its non-complementary Δ3’s; hexagon columnar crystals (Figure 5.6Q) formed with B7-Δ3’ at high concentration; and hexagonal pyramid with elongated points (similar to B7 with low concentration of B7-Δ3’) with B6-Δ3’ at high concentrations (Figure 5.6R).

Interestingly, the non-complementary Δ5’ poisons did show a trend toward tabular crystals with B7-13-mer and B6-13-mer (Figure 5.6) with the exception of A2-13-mer. Although the concentration of poisons required for the effect to be visible was at higher concentrations relative to the complementary versions. This, and the previously noted differences in concentration dependencies of Δ5’ and Δ3’ is most readily explained by their ability to integrate into the growing lattice. Because the duplex region is self-complementary, the poison strands can base pair with itself (homopaired) or base pair with the 13-mer strands (heteropaired). In the case of Δ3’, it is unlikely that homopaired poison strands could be stably integrated into the lattice, as the 3’-most residues are necessary for coaxially stacking of duplexes (Figure 5.2). Thus, higher concentrations are necessary to achieve sufficient concentrations of heteropaired duplex to observe the habit modification effects. Alternatively, both homopaired and heteropaired Δ5' species likely could both be incorporated between duplex regions, meaning lower concentrations would be required to observe habit modification. This is also consistent with the observation that non-complementary Δ5' poison strands can induce tabular habit modification, as they could be

incorporated in the homopaired form. As a control, an 11-mer with no complementary sequence to B7 was used as a poison to ensure active incorporation into the lattice via base-pairing is required to impede growth. The 11-mer did not act as a poison to B7 and its complementary sequences or had any effect on the morphology even when the concentration was 2.5x higher than the oligomer concentration (Figure 5.7).

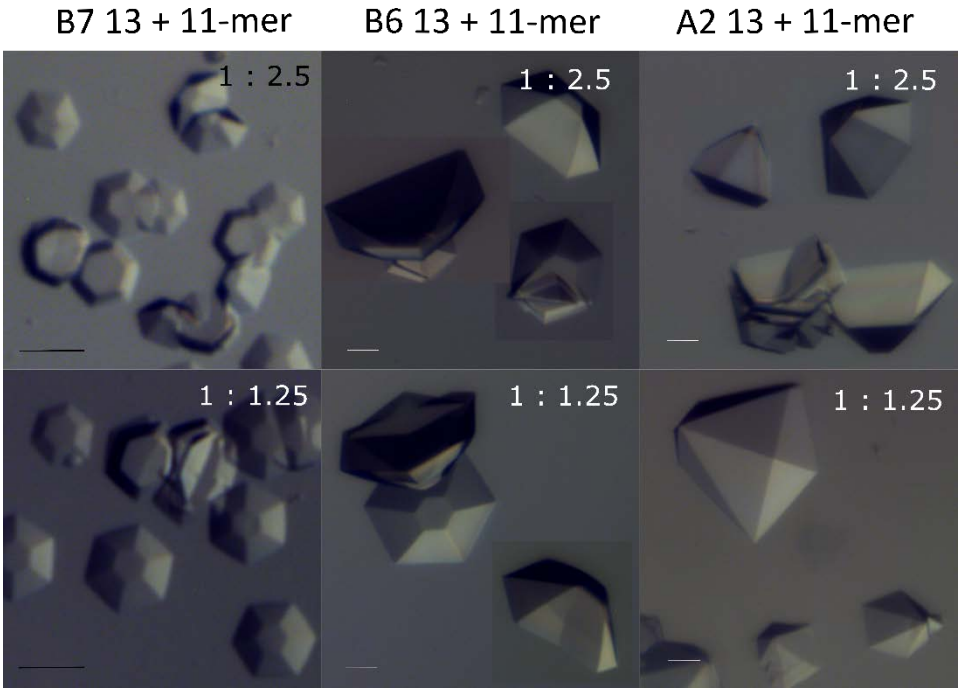

Figure 5.7. Light microscope images of 13-mer crystallized with 11-mer. Scale bars, 70 μm

Chapter 5.2.2: X-ray diffraction showed poison oligomers are only habit modifiers

Diffraction studies were consistent with the truncated oligomers functioning as habit modifiers and not as more general modifiers of crystal form. Crystals grown in the presence of Δ5' or Δ3' had similar unit cell parameters and apparent hexagonal space groups from indexing, while also having decreased diffraction limits (Figure 5.8). The decreased diffraction limit suggested the possibility that the poison strands were being incorporated into the crystal lattice, where they would likely cause local structural changes that would decrease lattice order and overall coherent diffraction.

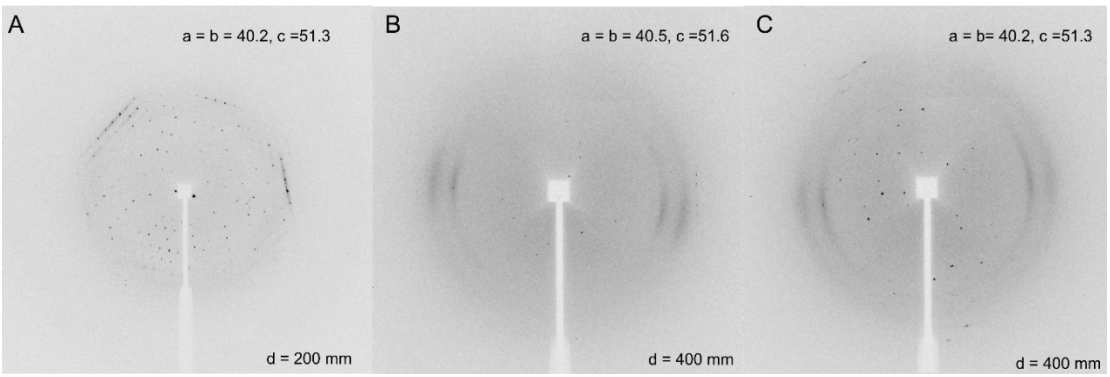

Figure 5.8. Diffraction images. **A.** Representative diffraction image from 13-mer crystals grown in the absence of poison strands. **B.** Diffraction image of a tabular crystal grown in Δ5', and **C.** diffraction from a crystal grown in the presence of Δ3'. For all images, d represents the detector distance. Unit cell dimensions determined from indexing using MOSFLM[121] are shown at the top. All diffraction images were collected at APS beamline BM-22 (SER-CAT).

Chapter 5.2.3: Incorporation of poison oligomers

Electrophoretic analysis of washed, dissolved, and radiolabeled crystals showed low-levels of an apparent 9 nt species in crystals grown in either Δ5' or Δ3' that was absent in crystals grown without the poison strands (Figure 5.9). It is unclear why Δ5' appears truncated by a single nucleotide, but we have previously observed that the 3' terminal guanosine (G13), which is unpaired in the crystal structure, is one of the more labile spots in the crystal (data not shown), and this may be exaggerated in the truncated form.

The poison incorporated was compared to the percentage of the poisons in the initial crystallization condition to determine if there was a correlation between the concentration at the initial crystallization conditions and the amount incorporated. The gel analysis of the dissolved crystals showed that that the incorporation of the poison within the crystal does not correlate to the ratio of the poisons added. The incorporation of the poisons, in terms of the band percentage (Table 5.1), did not exceed 25%, and ranged between 4% and 14% , even though the Δ3'

concentration in the initial condition was 20-fold higher than the Δ5'. The percentage of Δ5' incorporated was higher than the percentage in the initial crystallization condition, and the opposite was true for the Δ3' where the percentage of poison Δ3' incorporated was lower than the initial crystallization condition. This is likely because the concentration required for Δ3' to exert its habit modifying effect was significantly higher than for Δ5' and that the Δ5' is more stably incorporated into the lattice structure. Interestingly, B6 poison crystal set did not exhibit the same level of incorporation as B7 (Figure 5.10). The only low molecular weight band detected was the 9 nt band in the acicular crystal. Similar to the B7 set, the level of incorporation is within the range of 4%-14%. The pattern of poison incorporation was not the same as B7, even though B6 poisons had similar habit modifying effect as the B7 poisons. The only difference between B7 and B6 was the 2-nucleotide difference in the Crick-Watson pair; this suggest that the Crick-Watson pair played a part in the stable incorporation of the poison oligomers.

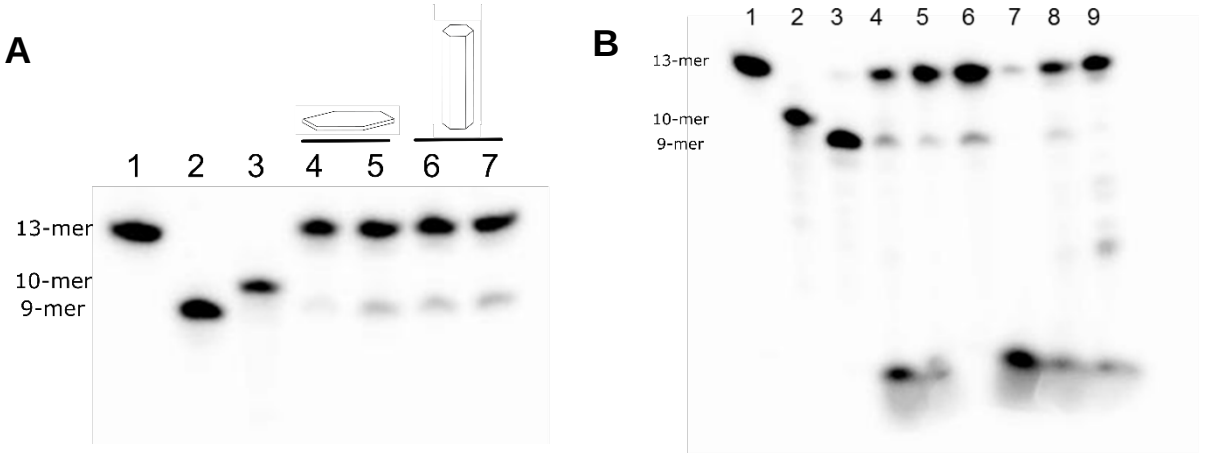

Figure 5.9. Polyacrylamide gel analysis of B7 poison crystals. **A.** Lane 1, 1 non-poison crystal; Lane 2, Δ3' alone; Lane 3, Δ5' alone; Lane 4 and 5, 2 Δ5' crystals; Lane 6 and 7, 2 Δ3' crystals. **B.** Lane 1, 1 non-poison crystal; Lane 2, Δ5' alone; Lane 3, Δ3' alone; Lane 4, 1 tabular crystal; Lane 5, 1 hexagonal unipyramid crystal grown in the presence of Δ5'; Lane 6, 1 acicular crystal; Lane 7, 1 hexagonal unipyramid crystal grown in the presence of Δ3'; Lane 8, 1 hexagon column crystal grown in the presence of Δ5' and Δ3'; Lane 9, 1 hexagon pyramid crystal grown in the presence of Δ5' and Δ3'.

	Left Gel							
	Lane 4		Lane 5		Lane 6		Lane 7	
	13-mer	Poison	13-mer	Poison	13-mer	Poison	13-mer	Poison
Band (%)	95.45	4.55	88.06	11.94	89.90	10.10	86.71	13.29
Xtal Conditions (%)	98.16	1.84	98.16	1.84	57.14	42.86	57.14	42.86
Band/Xtal Conditions	0.97	2.47	0.90	6.49	1.57	0.24	1.52	0.31
	Right Gel							
	Lane 4		Lane 5		Lane 6		Lane 8	
	13-mer	Poison	13-mer	Poison	13-mer	Poison	13-mer	Poison
Band (%)	78.19	21.81	95.06	4.94	90.50	9.50	91.09	8.91
Xtal Conditions (%)	97.71	2.29	99.77	0.23	70.67	29.33		
Band/Xtal Conditions	0.80	9.54	0.90	6.49	1.28	0.32		

Table 5.1. Analysis of **Figure 5.9** gel bands. shows percentage of gel band (Band), the percentage of B7 13 and B7 Δ3' or B7 Δ5' in original crystallization condition (Xtal Conditions) that the crystals came from and the ratio of the band to crystal conditions. Xtal = Crystal.

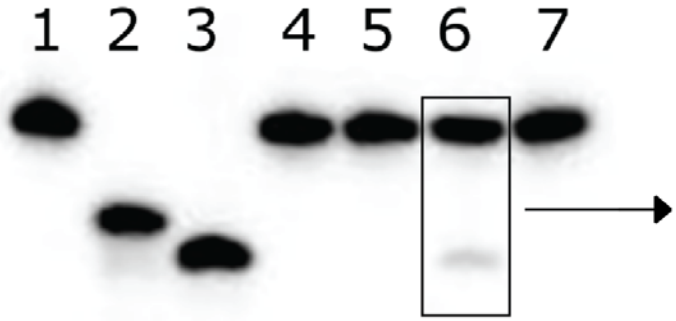

Band (%)	Xtal Conditions (%)	Band/Xtal Conditions
95.38	44.44	2.15
4.62	55.56	0.08

Figure 5.10. Polyacrylamide gel analysis of B6 poison crystals. Lane 1, non-poison crystal; Lane 2, B6 Δ5' alone; Lane 3, B6 Δ3' alone; Lane 4, tabular crystal; Lane 5, hexagonal unipyramid crystal grown in the presence of B6 Δ5'; Lane 6, acicular crystals; Lane 7, hexagonal unipyramid crystal grown in the presence of B6 Δ3'. Table of lane 6 shows percentage of gel band (Band), the percentage of B6 13 and B6 Δ3' in original crystallization condition (Xtal Conditions) that the crystals came from and the ratio of the band to crystal conditions. Xtal = Crystal.

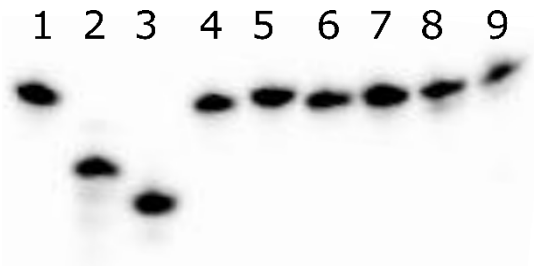

Figure 5.11. Polyacrylamide gel analysis of non-poison hexagonal unipyramid crystals soaked in poison oligomers. Lane 1, B7 non-poison crystal; Lane 2, B7 Δ5' alone; Lane 3, B7 Δ3' alone; Lane 4 hexagonal unipyramidal crystals in 300 μM Δ5'; Lane 5 hexagonal unipyramidal crystals in 1 mM Δ3'; Lane 6 hexagonal unipyramidal crystals in 1.25 μM Δ5'; Lane 7 hexagonal unipyramidal crystals in 21.25 μM Δ3'; Lane 8 poison Δ5' hexagonal unipyramidal crystal; and Lane 9 poison Δ3' hexagonal unipyramidal crystal.

Next, we passively soaked the crystals in the poisons to ensure the poisons detected in the crystals were the result of active incorporation rather than simply residing in the solvent channels. To determine if the B7 poisons in (Figure 5.9) were actively incorporated into the lattice structure (Figure 5.11), hexagonal unipyramidal crystals were soaked in either high or low concentrations of Δ5' or Δ3'. The high poison concentration used was equivalent to 2.5x the original 13-mer in the crystallization condition, and the low Δ5' or Δ3' concentrations used correlated to the poisons' concentrations when they no longer exerted their habit modifying effect. Also, hexagonal unipyramidal crystals grown with poisons present were also collected to observe whether incorporation still occurred when there was no evident morphological changes. No low molecular weight bands were seen in any of the conditions, concluding that the poisons in Figure 5.9 were actively incorporated into the lattice structure and not a result of the poisons superficially adhering to the lattice.

Chapter 5.2.4: Thermal stability of poison crystals

We compared the thermal stability of the poison crystals to the non-poison crystals to evaluate whether their incorporation of the poison oligomers caused instability in the lattice structure. The B7 and B6 poison crystals, and non-poison crystals were incubated at 33˚C and their diameters were measured over time; for the acicular crystals, the width was measure perpendicular to the c-axis. The non-poison crystals were present the longest (≥ 5 hrs), followed by the tabular crystals (4 hrs) and then the acicular crystals (3 hrs) in both the B7 and B6 set (Figure 5.12). It is not clear though whether the rate of the complete dissolution was due to the incorporation of the poison oligomers alone. The morphology, as a result of the poison oligomers, could have influenced the rate of dissolution by changing the surface area to volume ratio (SA:V) of the crystals. The larger the SA:V value was, the more it would had been affected by the temperature.

All of the crystals tested had similar diameter (including the length of the acicular), but the SA:V of the crystals would vary depending on the morphology. The hexagonal pyramidal would have the smallest SA:V and the poison crystals would have higher SA:V with the lost in either width or height in the presence of the poison oligomers (Figure 5.13). Based on the ratios of the crystals measured, the hexagonal pyramidal crystals had the smallest SA:V, followed by the acicular and tabular crystals. This showed a negative correlation between the SA:V of the crystals and the time it took for them to be completely disassembled. Therefore, the reason for the differences in the time it took for the crystals to be completely gone may not be necessarily due to the incorporation of the poison oligomers but due to the differences in SA:V between the different morphologies.

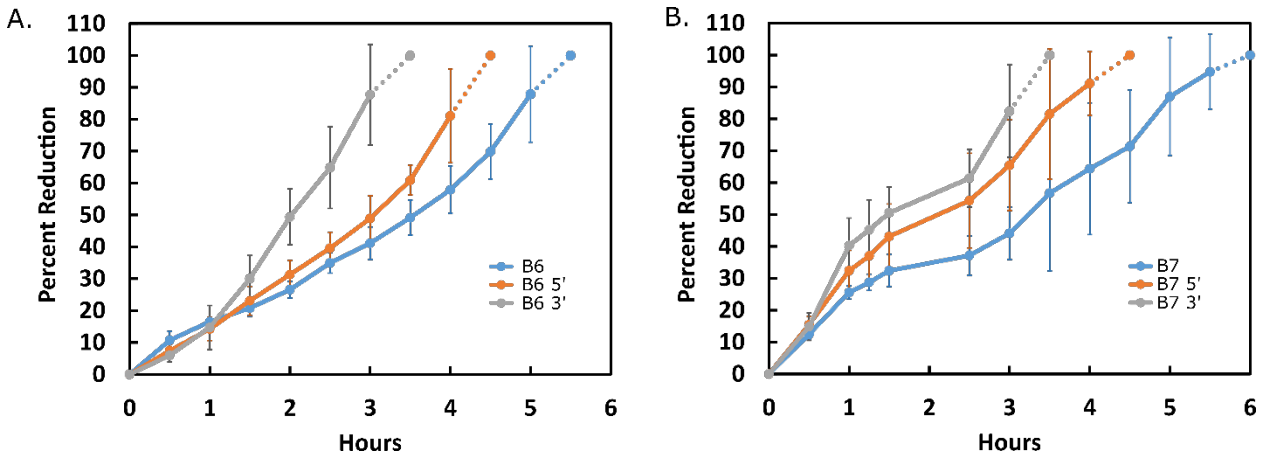

Figure 5.12. Thermal stability poison of **A.** B7 and **B.** B6 poison tabular and acicular crystals at 33˚C.

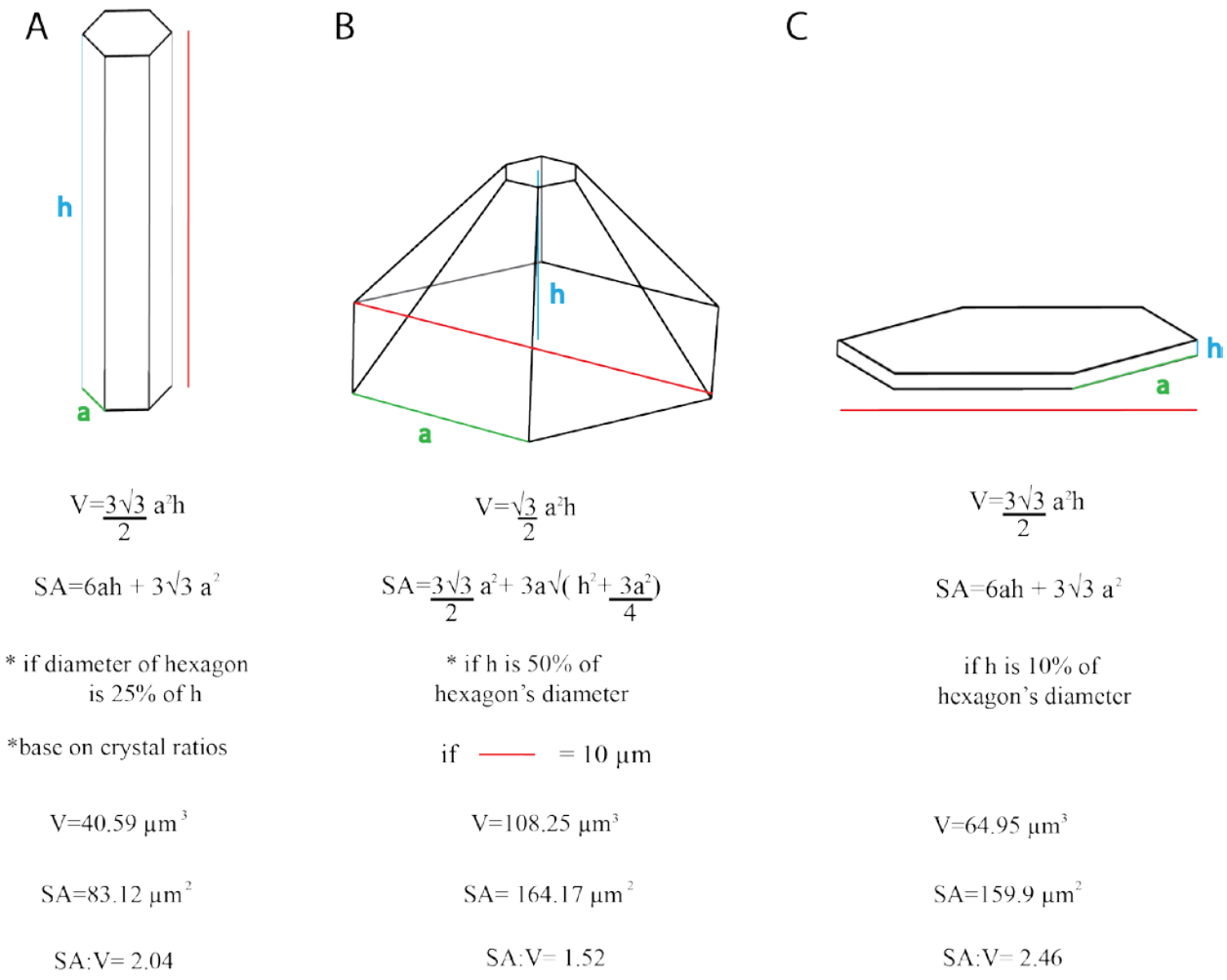

Figure 5.13. Theoretical crystal volumes (V), surface area (SA) and SA to Volume ratio of **A.** acicular crystals, **B.** hexagonal pyramid, **C.** of tabular crystals. Red lines are the same length.

Chapter 5.2.5: Layer-by-layer assembly with poison oligomers

Detecting the poison oligomers in the crystals suggested that they likely did not exhibit their effects only at crystal nucleation or prenucleation, but also during crystal growth. To directly test if the poison strands influenced crystal growth, we performed post-crystallization layering by adding fresh oligonucleotides to pre-formed crystals serving as macroseeds (see Chapter 1). A small amount of 3' fluorescein modified 13-mer (Figure 5.1) was included to track the newly grown layer by confocal microscopy. Figure 5.14 shows a series of z-axis slices and 3D reconstructions of hexagonal unipyramid macroseeds in the presence and absence of poison strands. In the absence

of poison strands, a uniform fluorescent layer grew over the pyrimidal crystal surface (Figure 5.14 A). In the presence of Δ5' the fluorescent layer showed preferential growth orthogonal to the six-fold symmetry axis, leading to a significantly enlarged hexagonal base (Figure 5.14B). In the presence of Δ3' the crystals showed preferential growth down the six-fold symmetry axis, leading to the growth of a new columnar base region capped by the pyrimidal segment as observed in the 3D reconstruction (Figure 5.14C) and in light microscope images (Figure 5.15A).

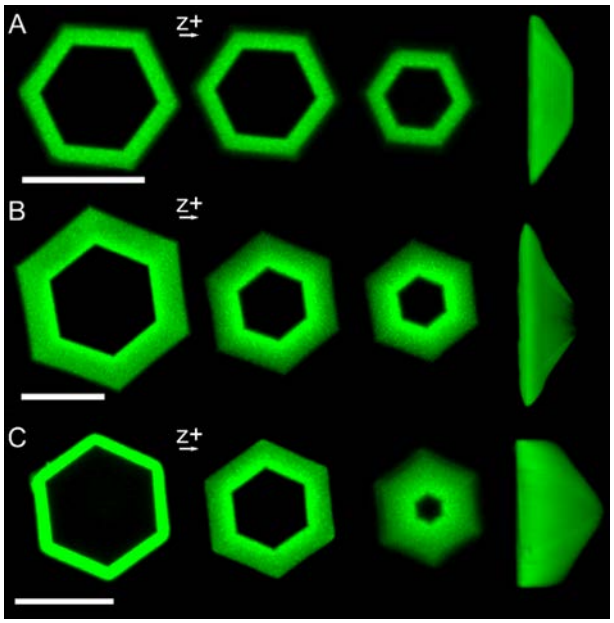

Figure 5.14. Poison oligmers function as habit modifiers during crystal growth. 13-mer crystal macroseeds were grown in the absence of habit modifiers. The fluorescently-modified 13-mer tracks the layer grown on the macroseed. For each panel, three confocal z-stack images down the *c* cell axis are shown, followed by a 3D reconstruction from all z-stack images, shown orthogonal to the *c* cell axis. **A.** Macroseed in the absence of poison displays uniform fluorescence accumulation. **B.** Shell growth in the presence of Δ5', leading to a new tabular layer that is significantly thicker along *a/b* than that in **A. C.** Layer growth in the presence of Δ3' is columnar, showing apparent increase in the thickness of the shell layer toward the 'top' of the core pyramidal crystal. Clear changes in crystal morphologies based on layer growth are seen in the 3D reconstructions. Scale bars, 50 μm.

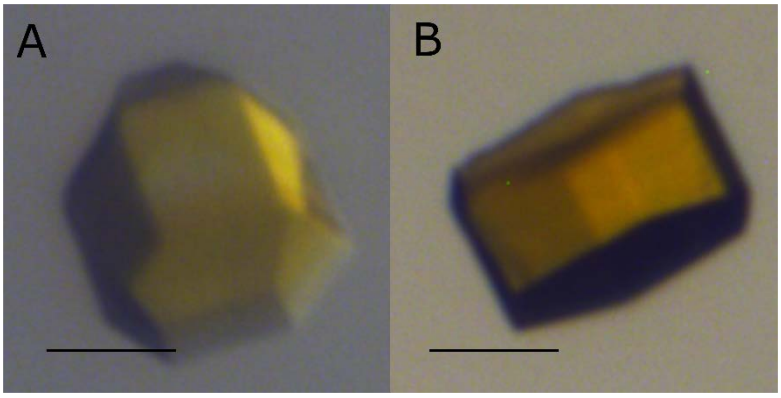

Figure 5.15. Light microscope images of crystals layered in the presence of Δ3'. **A.** Hexagon unipyramid used as macroseed. The macroseed is visible as the clear region at the center of the crystal. **B.** Tabular crystal used as macroseed. Scale bars: 70 µm.

Remarkably, this axis-dependent growth was also observed when tabular or acicular crystals were used as macroseeds (Figure 5.16). Tabular crystals initially grown in the presence of Δ5' showed uniform fluorescence layers in the absence of poison and began to grow as unipyramids (Figure 5.16A). Layer growth in the presence of Δ5' exacerbated the tabular morphology (Figure 5.16B), while the presence of Δ3' led to growth down the *c* axis, resulting in columnar growth from the tabular base (Figure 5.16C & Figure 5.15B). Similarly, acicular crystals initially grown in the presence of Δ3' showed bidirectional layer growth parallel and perpendicular to the *c* axis without poison (Figure 5.15D), only growth orthogonal to the c axis with Δ5' (Figure 5.16 E), and primarily growth down the *c* axis in the presence of Δ3' (Figure 5.16F). Using habit modifiers to control both the shape the crystal macroseed and the direction of crystal growth on that macroseed opens up the possibility for creating a highly diverse set of crystal morphologies. Significantly, it may be possible to achieve even greater levels of control by including both habit modifiers simultaneously, effectively tuning the growth characteristics.

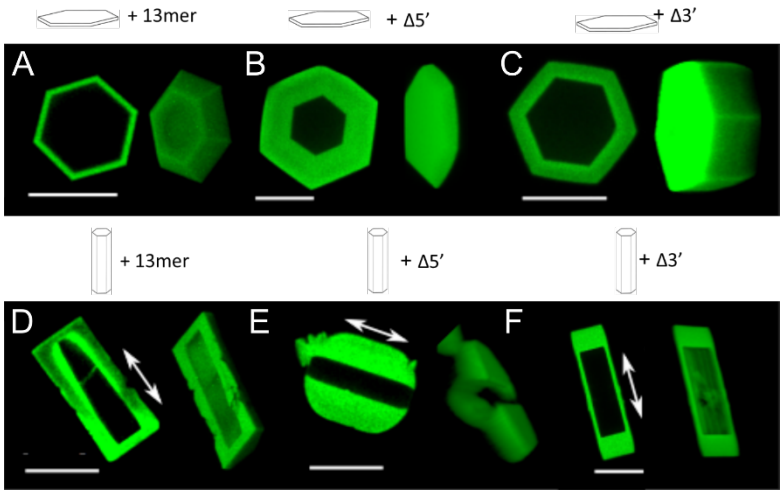

Figure 5.16 Habit-modified crystals as macroseeds. Each panel contains a confocal image to show layering and a 3D reconstruction to show overall shape. **A** Tabular crystals grown without poison strands; **B** in the presence of Δ5'; **C** in the presence of Δ3'. **D** Acicular crystals grown without poi-son strands; **E** in the presence of Δ5'; **F** in the presence of Δ3'. Arrows indicate the direction of the c cell axis. Scale bars: 50 μm.

Chapter 5.3: Conclusion

Here, we have presented an approach to altering the macroscopic properties of a DNA crystal using designed oligonucleotide habit modifiers. The change in crystal habits to a tabular form in the presence of Δ5' and to an acicular form in the presence of Δ3' is fully consistent with the relative positions of the 5' and 3' nucleotides with respect to the duplex helical axes. The ability to control macroscopic crystal properties, including morphology provides an important step toward integrated control across scales: the construction of macroscopic objects of controllable shapes, and exploitable nanoscale features, such as the solvent channels in these crystals. The ability to control shape allows for tunable crystal properties. For example, apparent mass transport effects were observed when DNA crystals containing enzymes were incubated with substrate molecules[26]. By altering crystal shape, it may be possible to control crystal permeability and diffusion through the crystal by selectively adjusting crystal habits to generate solvent channels with different aspect ratios. This demonstration provides a new branch of work in DNA crystal design through the

ability to alter both nanoscale and macroscale crystal properties. It is likely that other DNA crystal systems would be susceptible to habit modification using similar techniques. However, the relative orientation of DNA lattice contacts and crystal axes may require more involved design features than the simple truncations used here.

Chapter 5.4: Materials and Methods

Chapter: 5.4.1: Oligonucleotide synthesis and purification

The non-modified oligonucleotides were ordered from IDT (Integrated DNA Technologies) and/or the fluorescein-labeled 13-mer (Figure 5.1) was synthesized on an Expedite 8090 DNA synthesizer (PerSeptive Biosystems) with reagents from Glen Research (Sterling, VA) using standard phosphoramidite synthesis and deprotection. Oligonucleotides were gel purified and electroeluted as previously described[20] before dialysis against deionized water.

Chapter 5.4.2: Crystallization

Oligonucleotides were crystallized by sitting drop vapor diffusion. 2 µL of 200 µM 13 nucleotide oligomer and 1 µL water were added to the sitting drop, followed by 1 µL of crystallization buffer (10% 2-methy-2,4-pentanediol, 120 mM magnesium formate, 50 mM lithium chloride). Drops were equilibrated against 300 µL of crystallization buffer. Crystal trays were incubated overnight at 22˚C.

Crystals grown in the presence of poison oligomers were performed as described with the addition of 1 µL of the poison oligonucleotide (1 µM-2 mM) added in place of the water.

Chapter 5.4.3: Macroseed layer growth

Macroseed crystals were washed in 100 µL crystallization buffer prior to use. Macroseeds were transferred by nylon loop to a sitting drop containing 2 µL of crystallization buffer. 1 µL of 175 µM 13-mer oligomer supplemented with 25 µM fluorescein-labeled 13-mer were mixed with 1

µL of poison oligonucleotides (1 µM-1 mM) in the drop. The sitting drop was equilibrated against 300 µL of crystallization buffer and incubated overnight at 22˚C.

Chapter 5.4.4: Visualization and measurements

Light microscope crystal images were taken of the crystals in the sitting drop on a stereo microscope with an attached CCD camera. The fluorescein-incorporated layered crystals were imaged with a Leica SP5X confocal microscope. Prior to visualization, crystals were washed in 100 µL crystallization buffer and then transferred to a 200 µL crystallization buffer on a 35 mm glass bottom culture dish with 14 mm microwell. The fluorescein layer was visualized by excitation at 480 nm. Z-stack images were collected every 1 µm. Measurements and 3D reconstructions were performed in ImageJ[100].

Chapter 5.4.5: Crystal radiolabeling

Crystals were washed in 100 µL crystallization buffer for 5', dipped briefly in 100 µL water before being transferred to 7.6 µL water to allow the crystals to dissolve. 1 µL 10X T4PNK Reaction Buffer, 0.4 µL T4 polynucleotide kinase (New England Biolabs),and 1 µL of 50 pmol [γ-32P] ATP (PerkinElmer) were added and incubated at 37˚C for 30'. Reactions were terminated at 65˚C for 20'. Samples were mixed with denaturing loading buffer and loaded onto a 20% denaturing polyacrylamide gel (19:1). The gel was exposed onto a phosphor screen and the screen was scanned on a phosphoimager.

Chapter 6: Conclusion and Future Prospects

My Ph.D work has contributed methods and tools to facilitate and improve the utilization of 3D DNA crystals. One of the milestones was to increase the stability of the crystals by treating the 13-mer DNA crystals with a chemical cross-linker and/or the deposition of PDA. The chemical cross-linker, NOR, stabilized the crystal lattice directly through the formation of an interstrand crosslink using the free terminal nucleotides. The deposition of PDA onto/into the crystals was an alternative method discovered to stabilize the crystals. Although, it is unclear exactly how PDA stabilizes the crystal lattice, it is believed that the PDA can potentially act as a net for magnesium, therefore trapping the positively charged divalent cation essential for DNA nanostructure stability. Both treatments have successfully improved the thermal stability, stability at low magnesium concentration, and/or stability in simulated biological conditions. The development of these methods to increase the overall durability of 3D DNA crystals will facilitate the transition of DNA crystals for utilization for certain applications. For example, the increased durability could potentially allow the crystals to be repurposed as a drug delivery device where they would be exposed to an environment of low magnesium concentration, relatively higher temperatures and attacks from phosphodiesterase.

My work with stabilizing the DNA crystals has helped other projects in our lab and has the potential to be applied to other DNA nanostructures to improve their overall stability. In our lab, the use of NOR has decreased the degradation of the crystals during multiple manipulation with guest molecules that are to be incorporated into the solvent channels; specifically the incorporation of gold nanoparticles into a version of the 13-mer crystals with expanded solvent channels. NOR treatment has the potential to increase stability of other DNA nanostructure through the introduction of free terminal guanine nucleotides into the sequence. The concept of

using a chemical crosslinker can be further explored by testing other chemical crosslinkers, such as crotoaldehyde[114], which may improve durability further or stabilize the structure without the requirement of free terminal nucleotides. Furthermore, PDA provides an alternative, more passive method for stabilizing DNA nanostructures where no changes are made to the original sequence and only requires a simple single-step deposition method to coat the DNA nanostructure.

Additionally, my work in predictably modifying DNA crystal morphology is the first example of its kind in the nanotechnology field. I accomplished this by designing habit modifiers based on the structural information given by the X-ray diffraction of the 3D DNA crystal. The habit modifiers acted as poisons on the crystallization process and inhibited the growth in certain directions resulting in acicular and tabular versions of the original morphology. Furthermore, the habit modifiers can also be combined, allowing us to further modulate between the acicular and tabular morphologies. In addition, the habit modifiers' action are not limited at nucleation and can act upon the macroseed during layer-by-layer assembly[30]. Being able to change the morphology of crystals can potentially improve the permeability and diffusion of the substrate into or out of the solvent channels, and uptake by cells[24]. Therefore, this has the potential to improve the DNA crystals for nanotechnological applications, such as for drug delivery.

The ability to increase the durability and change the morphology of the 3D DNA crystals widens the application possible for this class of DNA nanostructure. Some of the potential applications made possible are the usage of the 3D DNA crystal as potential drug delivery device and the alignment of nanoparticles within the solvent channels. Our lab has taken the first step towards exploring the crosslinked 3D crystals as a drug delivery device by testing the incorporation of DOX within the solvent channels. I used confocal microscopy to confirm that

DOX was extensively incorporated within the crystal lattice. Interestingly, the crosslinked crystals showed added benefits of increasing the load capacity and retention of the DOX inside the crystal compared to the non-crosslinked crystals. This is believed to be possible due to the transition of the crystal lattice into a gel matrix upon addition of DOX, although the mechanism behind how this was occurred in the crosslinked is unclear.

The next step should be to focus on controlling the growth of the crystals, thus the size, which will further improve the feasibility of 3D DNA crystals for nanotechnological applications. The size of the 3D DNA crystals needs to be in the nanosize range in order for it to be probable as a vesicles for drug delivery, but the 3D DNA crystals normally range in size between 50 μm - 100 μm. Nanoparticles for drug delivery needs to be large enough in order to avoid rapid elimination by the kidneys[115] and small enough to avoid accumulation in the spleen and liver[116]. The effective range for a drug delivery device would be between 30 and 200 nm. Potential methods for controlling the size would be to either focus on the crystallization condition or mechanically breaking the microsize crystals into nanosize crystals. Additionally, a technique would be needed to separate the crystals by size in order to get the ideal range for drug delivery. Rate-zonal centrifugation has proven to be effective for purification of DNA origami[117] and may be possibly optimized for DNA crystals.

Once nanosized crystals are obtained, the DOX crystals can be tested for efficacy through tissue cultures or animal models. The efficacy of the DOX-incorporated can be compared to DOX alone, with other DNA nanostructures such as DNA origami or DNA icosahedra which have been tested in tissue cultures and mice[24,25]. Additionally, we can vary the shape and see how that affects the efficacy and distribution since previous studies with DNA nanostructures had shown that shape can have an effect[24]. Furthermore, the layer-by-layer assembly allows

customization of the outer layer with guest molecules[30] that could potentially increase efficacy such as attaching antibodies targeted towards specific surface proteins of the intended cells.

Overall, my Ph.D work with DNA crystals has the potential to advance its usage for nanotechnological applications by overcoming limitations inherent to these structures. The simple methods of using NOR or PDA deposition to increase overall durability has improved the integrity of the 3D DNA crystals in our lab during their utilization, such as the incorporation of DOX. Likewise, the principles of using a simple chemical crosslinker or PDA deposition method to stabilize structures may be broadly applicable to other types of DNA nanostructures as well. Additionally, the design of habit modifiers that can predictably control the shape for the first time offers a new way to design DNA crystals at the nano- and macroscale level.

Bibliography

1. Jones, M. R., Seeman, N. C. & Mirkin, C. A. Programmable materials and the nature of the DNA bond. *Science* **347,** 1260901 (2015).
2. Hagerman, P. J. Flexibility of DNA. *Annu. Rev. Biophys. Biophys. Chem.* **17,** 265–286 (1988).
3. Chen, J. H. & Seeman, N. C. Synthesis from DNA of a molecule with the connectivity of a cube. *Nature* **350,** 631–3 (1991).
4. Shih, W. M., Quispe, J. D. & Joyce, G. F. A 1.7-kilobase single-stranded DNA that folds into a nanoscale octahedron. *Nature* **427,** 618–21 (2004).
5. Winfree, E., Liu, F., Wenzler, L. A. & Seeman, N. C. Design and self-assembly of two-dimensional DNA crystals. *Nature* **394,** 539–44 (1998).
6. Rothemund, P. W. K., Ekani-Nkodo, A., Papadakis, N., Kumar, A., Fygenson, D.K. & Winfree, E. Design and characterization of programmable DNA nanotubes. *J. Am. Chem. Soc.* **126,** 16344–52 (2004).
7. Rothemund, P. W. K. Folding DNA to create nanoscale shapes and patterns. *Nature* **440,** 297–302 (2006).
8. Douglas, S. M., Dietz, H., Liedl, T., Högberg, B., Graf, F. & Shih, W.M. Self-assembly of DNA into nanoscale three-dimensional shapes. *Nature* **459,** 414–418 (2009).
9. Dietz, H., Douglas, S. M. & Shih, W. M. Folding DNA into Twisted and Curved Nanoscale Shapes. *Science* **325,** 725–730 (2009).
10. Han, D., Pal, S., Nangreave, J., Deng, Z., Liu, Y. & Yan, H.. DNA origami with complex curvatures in three-dimensional space. *Science* **332,** 342–346 (2011).
11. Han, D., Pal, S., Yang, Y., Jiang, S., Nangreave, J., Liu, Y. & Yan, H. DNA gridiron nanostructures based on four-arm junctions. *Science* **339,** 1412–1415 (2013).

12. Zhang, F., Nangreave, J., Liu, Y. & Yan, H. Structural DNA nanotechnology: state of the art and future perspective. *J. Am. Chem. Soc.* **136,** 11198–11211 (2014).

13. Andersen, E. S., Dong, M., Nielsen, M.M., Jahn, K., Lind-Thomsen, A., Mamdouh, W., Gothelf, K.V., BesenbacheR, F., & Kjems, J.. DNA Origami Design of Dolphin-Shaped Structures with Flexible Tails. *ACS Nano* **2,** 1213–1218 (2008).

14. Andersen, E. S., Dong, M., Nielsen, M.M, Jahn, K., Subramani, R., Mamdouh, W., Golas, M.M., Sander, B., Stark, H., Oliveira, C.L.P., Pedersen, J.S., Birkedal, V., Besenbacher, F., Gothelf, K.V., & Kjems, J. Self-assembly of a nanoscale DNA box with a controllable lid. *Nature* **459,** 73–76 (2009).

15. Tian, C., Li, X., Liu, Z., Jiang, W., Wang, G. & Mao, C. Directed Self-Assembly of DNA Tiles into Complex Nanocages. *Angew. Chem. Int. Ed.* **53,** 8041–8044 (2014).

16. Ke, Y., Ong, L. L., Shih, W. M. & Yin, P. Three-Dimensional Structures Self-Assembled from DNA Bricks. *Science* **338,** 1177–1183 (2012).

17. Zheng, J., Birktoft, J.J, Chen, Y., Wang, T., Sha, R., Constantinou, P.E., Ginell, S.L., Mao, C. & Seeman, N.C. From molecular to macroscopic via the rational design of a self-assembled 3D DNA crystal. *Nature* **461,** 74–77 (2009).

18. Caruthers, M. H. Gene synthesis machines: DNA chemistry and its uses. *Science* **230,** 281–285 (1985).

19. Um, S. H., Lee, J.B., Park, N., Kwon, S.Y., Umbach, C.C. & Luo, D. Enzyme-catalysed assembly of DNA hydrogel. *Nat. Mater.* **5,** 797–801 (2006).

20. Paukstelis, P. J., Nowakowski, J., Birktoft, J. J. & Seeman, N. C. Crystal structure of a continuous three-dimensional DNA lattice. *Chem. Biol.* **11,** 1119–1126 (2004).

21. Buckhout-White, S., Spillmann, C.M., Algar, W.R., Khachatrian, A., Melinger, J.S., Goldman, E.R., Ancona, M.G. & Medintz, I.L. Assembling programmable FRET-based photonic networks using designer DNA scaffolds. *Nat. Commun.* **5,** 5615 (2014).

22. Chao, J., Zhu, D., Zhang, Y., Wang, L. & Fan, C. DNA nanotechnology-enabled biosensors. *Biosens. Bioelectron.* **76,** 68–79 (2016).

23. Perrault, S. D. & Shih, W. M. Virus-Inspired Membrane Encapsulation of DNA Nanostructures To Achieve In Vivo Stability. *ACS Nano* **8,** 5132–5140 (2014).

24. Zhang, Q., Jiang, Q., Li, N., Dai, L., Liu, Q., Song, L., Wang, J., Li, Y., Tian, J., Ding, B. & Du, Y. DNA Origami as an In Vivo Drug Delivery Vehicle for Cancer Therapy. *ACS Nano* **8,** 6633–6643 (2014).

25. Chang, M., Yang, C.-S. & Huang, D.-M. Aptamer-Conjugated DNA Icosahedral Nanoparticles As a Carrier of Doxorubicin for Cancer Therapy. *ACS Nano* **5,** 6156–6163 (2011).

26. Geng, C. & Paukstelis, P. J. DNA crystals as vehicles for biocatalysis. *J. Am. Chem. Soc.* **136,** 7817–7820 (2014).

27. Paukstelis, P. J. Three-dimensional DNA crystals as molecular sieves. *J. Am. Chem. Soc.* **128,** 6794–5 (2006).

28. Seeman, N. C. Nucleic acid junctions and lattices. *J. Theor. Biol.* **99,** 237–47 (1982).

29. Wang, T., Sha, R., Birktoft, J., Zheng, J., Mao, C. & Seeman, N.C. A DNA crystal designed to contain two molecules per asymmetric unit. *J. Am. Chem. Soc.* **132,** 15471–15473 (2010).

30. McNeil, R. & Paukstelis, P. J. Core–Shell and Layer-by-Layer Assembly of 3D DNA Crystals. *Adv. Mater.* **29,** 1701019 (2017).

31. Saoji, M., Zhang, D. & Paukstelis, P. J. Probing the role of sequence in the assembly of three-dimensional DNA crystals. *Biopolymers* **103,** 618–626 (2015).

32. Castro, C. E., Kilchherr, F., Kim, D., Shiao, E.L., Wauer, T., Wortmann, P., Bathe, M. & Dietz, H. A primer to scaffolded DNA origami. *Nat. Methods* **8,** 221–229 (2011).

33. Wei, X., Nangreave, J., Jiang, S., Yan, H. & Liu, Y. Mapping the Thermal Behavior of DNA Origami Nanostructures. *J. Am. Chem. Soc.* **135,** 6165–6176 (2013).

34. Stahl, E., Praetorius, F., de Oliveira Mann, C. C., Hopfner, K.-P. & Dietz, H. Impact of Heterogeneity and Lattice Bond Strength on DNA Triangle Crystal Growth. *ACS Nano* **10,** 9156–9164 (2016).

35. Muser, S. E. & Paukstelis, P. J. Three-dimensional DNA crystals with pH-responsive noncanonical junctions. *J. Am. Chem. Soc.* **134,** 12557–12564 (2012).

36. Tripathi, S. & Paukstelis, P. J. Structural Implications of Homopyrimidine Base Pairs in the Parallel-Stranded d(YGA) Motif. *ChemBioChem* **17,** 1177–1183 (2016).

37. Albanese, A., Tang, P.S. & Chan, W.C. The Effect of Nanoparticle Size, Shape, and Surface Chemistry on Biological Systems. *Annu. Rev. Biomed. Eng.* **14,** 1–16 (2012).

38. Zhang, D. & Paukstelis, P. J. Enhancing DNA Crystal Durability through Chemical Crosslinking. *ChemBioChem* **17,** 1163–1170 (2016).

39. Zhang, D. & Paukstelis, P. J. Designed DNA Crystal Habit Modifiers. *J. Am. Chem. Soc.* **139,** 1782–1785 (2017).

40. Linko, V., Ora, A. & Kostiainen, M. A. DNA Nanostructures as Smart Drug-Delivery Vehicles and Molecular Devices. *Trends Biotechnol.* **33,** 586–594 (2015).

41. Jiang, Q., Song, C., Nangreave, J., Liu, X., Lin, L., Qiu, D., Wang, Z.G., Zou, G., Liang, X., Yan, H. & Ding, B. DNA origami as a carrier for circumvention of drug resistance. *J. Am. Chem. Soc.* **134,** 13396–13403 (2012).

42. Quiocho, F. A. & Richards, F. M. Intermolecular Cross Linking of a Protein in the Crystalline State: Carboxypeptidase-A. *Proc. Natl. Acad. Sci. U. S. A.* **52,** 833–839 (1964).

43. Lusty, C. J. A gentle vapor-diffusion technique for cross-linking of protein crystals for cryocrystallography. *J. Appl. Crystallogr.* **32,** 106–112 (1999).

44. Salem, M., Mauguen, Y. & Prangé, T. Revisiting glutaraldehyde cross-linking: the case of the Arg–Lys intermolecular doublet. *Acta Crystallograph. Sect. F Struct. Biol. Cryst. Commun.* **66,** 225–228 (2010).

45. Rajendran, A., Endo, M., Katsuda, Y., Hidaka, K. & Sugiyama, H. Photo-Cross-Linking-Assisted Thermal Stability of DNA Origami Structures and Its Application for Higher-Temperature Self-Assembly. *J. Am. Chem. Soc.* **133,** 14488–14491 (2011).

46. Cassinelli, V., Oberleitner, B., Sobotta, J., Nickels, P., Grossi, G., Kempter, S., Frischmuth, T., Liedl, T. & Manetto, A. One-Step Formation of 'Chain-Armor'-Stabilized DNA Nanostructures. *Angew. Chem. Int. Ed.* **54,** 7795–7798 (2015).

47. Hemminki, K. DNA-binding products of nornitrogen mustard, a metabolite of cyclophosphamide. *Chem. Biol. Interact.* **61,** 75–88 (1987).

48. Malayappan, B., Johnson, L., Nie, B., Panchal, D., Matter, B., Jacobson, P. & Tretyakova, N. Quantitative High-Performance Liquid Chromatography−Electrospray Ionization Tandem Mass Spectrometry Analysis of Bis-N7-Guanine DNA−DNA Cross-Links in White Blood Cells of Cancer Patients Receiving Cyclophosphamide Therapy. *Anal. Chem.* **82,** 3650–3658 (2010).

49. Hartley-Asp, B. & Hyldig-Nielsen, F. Comparative genotoxicity of nitrogen mustard and nor-nitrogen mustard. *Carcinogenesis* **5,** 1637–1640 (1984).

50. Balcome, S., Park, S., Quirk Dorr, D.R., Hafner, L., Phillips, L. & Tretyakova, N. Adenine-Containing DNA−DNA Cross-Links of Antitumor Nitrogen Mustards. *Chem. Res. Toxicol.* **17,** 950–962 (2004).

51. Osborne, M. R., Wilman, D. E. V. & Lawley, P. D. Alkylation of DNA by the Nitrogen Mustard Bis-(2-chloroethyl)methylamine. *Chem. Res. Toxicol.* **8,** 316–320 (1995).

52. Hemminki, K., Alhonen, A., Linkola, E. & Hesso, A. Kinetics of hydrolysis in vitro of nornitrogen mustard, a metabolite of phosphoramide mustard and cyclophosphamide. *Arch. Toxicol.* **61,** 126–130 (1987).

53. Lillehaug, J. R., Kleppe, R. K. & Kleppe, K. Phosphorylation of double-stranded DNAs by T4 polynucleotide kinase. *Biochemistry Mosc.* **15,** 1858–1865 (1976).

54. Meyers, R.A. *Encyclopedia of molecular cell biology and molecular medicine.* (Wiley-VCH Verlag, 2004).

55. Zhao, J., Chandrasekaran, A.R., Li, Q., Li, X., Sha, R., Seeman, N.C. & Mao, C. Post-Assembly Stabilization of Rationally Designed DNA Crystals. *Angew. Chem. Int. Ed.* **54,** 9936–9939 (2015).

56. Hahn, J., Wickham, S. F. J., Shih, W. M. & Perrault, S. D. Addressing the Instability of DNA Nanostructures in Tissue Culture. *ACS Nano* **9,** 8765-8775 (2014).

57. Melgar, E. & Goldthwait, D. A. Deoxyribonucleic acid nucleases. II. The effects of metals on the mechanism of action of deoxyribonuclease I. *J. Biol. Chem.* **243,** 4409–4416 (1968).

58. Keum, J.-W. & Bermudez, H. Enhanced resistance of DNA nanostructures to enzymatic digestion. *Chem. Commun.* **45,** 7036–7038 (2009).

59. Prakash, A. S., Tran, H.-P., Peng, C., Koyalamudi, S. R. & Dameron, C. T. Kinetics of DNA alkylation, depurination and hydrolysis of anti diol epoxide of benzo(a)pyrene and the effect of cadmium on DNA alkylation. *Chem. Biol. Interact.* **125,** 133–150 (2000).

60. Chung, M. H., Kiyosawa, H., Ohtsuka, E., Nishimura, S. & Kasai, H. DNA strand cleavage at 8-hydroxyguanine residues by hot piperidine treatment. *Biochem. Biophys. Res. Commun.* **188,** 1–7 (1992).

61. Lee, H., Dellatore, S. M., Miller, W. M. & Messersmith, P. B. Mussel-Inspired Surface Chemistry for Multifunctional Coatings. *Science* **318,** 426–430 (2007).

62. Haemers, S., Koper, G. J. M. & Frens, G. Effect of Oxidation Rate on Cross-Linking of Mussel Adhesive Proteins. *Biomacromolecules* **4,** 632–640 (2003).

63. Wei, Q., Zhang, F., Li, J., Li, B. & Zhao, C. Oxidant-induced dopamine polymerization for multifunctional coatings. *Polym. Chem.* **1,** 1430–1433 (2010).

64. Ye, Q., Zhou, F. & Liu, W. Bioinspired catecholic chemistry for surface modification. *Chem. Soc. Rev.* **40,** 4244–4258 (2011).

65. Postma, A., Yan, Y., Wang, Y., Zelikin, A.N., Tjipto, E., & Caruso, F. Self-Polymerization of Dopamine as a Versatile and Robust Technique to Prepare Polymer Capsules. *Chem. Mater.* **21,** 3042–3044 (2009).

66. Arzillo, M., Pezzella, A., Crescenzi, O., Napolitano, A., Land, E.J., Barone, V. & d'Ischia, M. Cyclic Structural Motifs in 5,6-Dihydroxyindole Polymerization Uncovered: Biomimetic Modular Buildup of a Unique Five-Membered Macrocycle. *Org. Lett.* **12,** 3250–3253 (2010).

67. Bisaglia, M., Mammi, S. & Bubacco, L. Kinetic and Structural Analysis of the Early Oxidation Products of Dopamine Analysis of the Interactions with α-Synuclein. *J. Biol. Chem.* **282,** 15597–15605 (2007).

68. Adhyaru, B. B., Akhmedov, N. G., Katritzky, A. R. & Bowers, C. R. Solid-state cross-polarization magic angle spinning 13C and 15N NMR characterization of Sepia melanin, Sepia melanin free acid and Human hair melanin in comparison with several model compounds. *Magn. Reson. Chem.* **41,** 466–474 (2003).

69. Hong, S., Na, Y., Choi, S., Song, I., Kim, W. & Lee, H. Non-Covalent Self-Assembly and Covalent Polymerization Co-Contribute to Polydopamine Formation. *Adv. Funct. Mater.* **22,** 4711–4717 (2012).

70. Yu, B., Wang, D. A., Ye, Q., Zhou, F. & Liu, W. Robust polydopamine nano/microcapsules and their loading and release behavior. *Chem. Commun.* 6789–6791 (2009).

71. Liu, K., Wei, W.-Z., Zeng, J.-X., Liu, X.-Y. & Gao, Y.-P. Application of a novel electrosynthesized polydopamine-imprinted film to the capacitive sensing of nicotine. *Anal. Bioanal. Chem.* **385,** 724–729 (2006).

72. He, H., Xie, Q. & Yao, S. An electrochemical quartz crystal impedance study on anti-human immunoglobulin G immobilization in the polymer grown during dopamine oxidation at an Au electrode. *J. Colloid Interface Sci.* **289,** 446–454 (2005).

73. Holten-Andersen, N., N., Mates, T.E., Toprak, M.S., Stucky, G.D., Zok, F.W. & Waite, J.H. Metals and the Integrity of a Biological Coating. *Langmuir ACS J. Surf. Colloids* **25,** 3323–3326 (2009).

74. Lebedev, A. V., Ivanova, M. V., Timoshin, A. A. & Ruuge, E. K. Effect of Group II Metal Cations on Catecholate Oxidation. *ChemPhysChem* **8,** 1863–1869 (2007).

75. Zahid, M., Saeed, M., Yang, L., Beseler, C., Rogan, E. & Cavalieri, E.L. Formation of dopamine quinone-DNA adducts and their potential role in the etiology of Parkinson's disease. *IUBMB Life* **63,** 1087–1093 (2011).

76. Arcamone, F., Cassinelli, G., Fantini, G., Grein, A., Orezzi, P., Pol, C. & Spalla, C. Adriamycin, 14-Hydroxydaunomycin, a new antitumor antibiotic from S. peucetius var. caesius. *Biotechnol. Bioeng.* **67,** 704–713 (2000).

77. Edmonson, J. H., Petersen, I.A., Shives, T.C., Mahoney, M.R., Rock, M.G., Haddock, M.G., Sim, F.H., Maples, W.J., O'Connor, M.I., Gunderson, L.L., Foo, M.L., Pritchard, D.J., Buckner, J.C. & Stafford S.L. Chemotherapy, irradiation, and surgery for function-preserving therapy of primary extremity soft tissue sarcomas. *Cancer* **94,** 786–792 (2002).

78. Mishima, Y., Nagasaki, E., Terui, Y., Irie, T., Takahashi, S., Ito, Y., Oguchi, M., Kawabata, K., Kamata, S. & Hatake, K. Combination chemotherapy (cyclophosphamide, doxorubicin, and vincristine with continuous-infusion cisplatin and etoposide) and radiotherapy with stem cell support can be beneficial for adolescents and adults with estheisoneuroblastoma. *Cancer* **101,** 1437–1444 (2004).

79. Tewey, K. M., Rowe, T. C., Yang, L., Halligan, B. D. & Liu, L. F. Adriamycin-induced DNA damage mediated by mammalian DNA topoisomerase II. *Science* **226,** 466–468 (1984).

80. Singal, P. K. & Iliskovic, N. Doxorubicin-Induced Cardiomyopathy. *N. Engl. J. Med.* **339,** 900–905 (1998).

81. Petros, R. A. & DeSimone, J. M. Strategies in the design of nanoparticles for therapeutic applications. *Nat. Rev. Drug Discov.* **9,** 615–627 (2010).

82. Wang, A. Z., Langer, R. & Farokhzad, O. C. Nanoparticle Delivery of Cancer Drugs. *Annu. Rev. Med.* **63,** 185–198 (2012).

83. Torchilin, V. P. Recent advances with liposomes as pharmaceutical carriers. *Nat. Rev. Drug Discov.* **4,** 145–160 (2005).

84. Hofheinz, R., Gnad-vogt, S. U., Beyer, U. & Hochhaus, A. Liposomal encapsulated anti-cancer drugs. *Anticancer. Drugs* **16,** 691–707

85. Kim, S. H., Jeong, J. H., Chun, K. W. & Park, T. G. Target-Specific Cellular Uptake of PLGA Nanoparticles Coated with Poly(l-lysine)−Poly(ethylene glycol)−Folate Conjugate. *Langmuir* **21,** 8852–8857 (2005).

86. Minelli, C., Lowe, S. B. & Stevens, M. M. Engineering Nanocomposite Materials for Cancer Therapy. *Small* **6,** 2336–2357 (2010).

87. Bandak, S., Goren, D., Horowitz, A., Tzemach, D. & Gabizon, A. Pharmacological studies of cisplatin encapsulated in long-circulating liposomes in mouse tumor models. *Anticancer Drugs* **10,** 911–920 (1999).

88. Allen, T. M., Mumbengegwi, D. R. & Charrois, G. J. R. Anti-CD19-Targeted Liposomal Doxorubicin Improves the Therapeutic Efficacy in Murine B-Cell Lymphoma and Ameliorates the Toxicity of Liposomes with Varying Drug Release Rates. *Clin. Cancer Res.* **11,** 3567–3573 (2005).

89. Breton, P., Guillon, X., Roy, D., Lescure, F., Riess, G., Bru, N. & Roques-Carmes, C. Physico-chemical characterization, preparation and performance of poly (methylidene malonate 2.1.2) nanoparticles. *Biomaterials* **19,** 271–281 (1998).

90. Pinheiro, A. V., Han, D., Shih, W. M. & Yan, H. Challenges and opportunities for structural DNA nanotechnology. *Nat. Nanotechnol.* **6,** 763–772 (2011).

91. Li, J., Pei, H., Zhu, B., Liang, L., Wei, M., He, Y., Chen, N., Li, D., Huang, Q. & Fan, C. Self-Assembled Multivalent DNA Nanostructures for Noninvasive Intracellular Delivery of Immunostimulatory CpG Oligonucleotides. *ACS Nano* **5,** 8783–8789 (2011).

92. Douglas, S. M., Bachelet, I. & Church, G. M. A logic-gated nanorobot for targeted transport of molecular payloads. *Science* **335,** 831–834 (2012).

93. Pastan, I. & Gottesman, M. M. Multidrug Resistance. *Annu. Rev. Med.* **42,** 277–284 (1991).

94. Gottesman, M. M. Mechanisms of cancer drug resistance. *Annu. Rev. Med.* **53,** 615–627 (2002).

95. Wang, J. Y.-T., Chao, M. & Wang, A. H.-J. Adducts of DNA and Anthracycline Antibiotics. in *Anthracycline Antibiotics* **574,** 168–182. (1994).

96. Perez-Arnaiz, C., Busto, N., Leal, J. M. & Garcia, B. New insights into the mechanism of the DNA/doxorubicin interaction. *J. Phys. Chem. B* **118,** 1288–1295 (2014).

97. Yang, X.-L. & Wang, A. H.-J. Structural studies of atom-specific anticancer drugs acting on DNA. *Pharmacol. Ther.* **83,** 181–215 (1999).

98. Karukstis, K. K., Thompson, E. H. Z., Whiles, J. A. & Rosenfeld, R. J. Deciphering the fluorescence signature of daunomycin and doxorubicin. *Biophys. Chem.* **73,** 249–263 (1998).

99. Salerno, M., Dante, S., Patra, N. & Diaspro, A. AFM measurement of the stiffness of layers of agarose gel patterned with polylysine. *Microsc. Res. Tech.* **73,** 982–990 (2010).

100. Schneider, C. A., Rasband, W. S. & Eliceiri, K. W. NIH Image to ImageJ: 25 years of image analysis. *Nat. Methods* **9,** 671–675 (2012).

101. El-Shall, H., Abdel-Aal, E. A. & Moudgil, B. M. Effect of Surfactants on Phosphogypsum Crystallization and Filtration during Wet-Process Phosphoric Acid Production. *Sep. Sci. Technol.* **35,** 395–410 (2000).

102. Titiz-Sargut, S., Sayan, P. & Avcı, B. Influence of citric acid on calcium sulfate dihydrate crystallization in aqueous media. *Cryst. Res. Technol.* **42,** 119–126 (2007).

103. Fang, X.-L., Chen, C., Jin, M., Kuang, Q., Xie, Z., Xie, S., Huanga, R. & Zhenga, L. Single-crystal-like hematite colloidal nanocrystal clusters: synthesis and applications in gas sensors, photocatalysis and water treatment. *J. Mater. Chem.* **19,** 6154–6160 (2009).

104. Lee, J. Y., Hong, B.H., Kim, W.Y., Min, S.K., Kim, Y., Jouravlev, M.V., Bose, R., Kim, K.S., Hwang, I., Kaufman, L.J., Wong, C.W., Kim, P. & Kim, K.S. Near-field focusing and magnification through self-assembled nanoscale spherical lenses. *Nature* **460,** 498–501 (2009).

105. Mahal, A., Tandon, L., Khullar, P., Ahluwalia, G. K. & Bakshi, M. S. pH Responsive Bioactive Lead Sulfide Nanomaterials: Protein Induced Morphology Control, Bioapplicability, and Bioextraction of Nanomaterials. *ACS Sustain. Chem. Eng.* **5,** 119–132 (2016).

106. Ndao, M., Keene, E., Amos, F.F., Rewari, G., Ponce, C.B., Estroff, L. & Evans, J.S. Intrinsically disordered mollusk shell prismatic protein that modulates calcium carbonate crystal growth. *Biomacromolecules* **11,** 2539–2544 (2010).

107. Nancollas, G. H., Tang, R., Phipps, R.J., Henneman, Z., Gulde, S., Wu, W., Mangood, A., Russell, R.G. & Ebetino, F.H. Novel insights into actions of bisphosphonates on bone: differences in interactions with hydroxyapatite. *Bone* **38,** 617–627 (2006).

108. Xu, A.-W., Ma, Y. & Cölfen, H. Biomimetic mineralization. *J. Mater. Chem.* **17,** 415–449 (2007).

109. Volkmer, D., Fricke, M., Huber, T. & Sewald, N. Acidic peptides acting as growth modifiers of calcite crystals. *Chem. Commun.* 1872–1873 (2004).

110. Sizemore, J. P. & Doherty, M. F. A New Model for the Effect of Molecular Imposters on the Shape of Faceted Molecular Crystals. *Cryst. Growth Des.* **9,** 2637–2645 (2009).

111. Han, G., Chow, P. S. & Tan, R. B. H. Growth Behaviors of Two Similar Crystals: The Great Difference. *Cryst. Growth Des.* **15,** 1082–1088 (2015).

112. Chung, J., Granja, I., Taylor, M.G., Mpourmpakis, G., Asplin, J.R. & Rimer, J.D. Molecular modifiers reveal a mechanism of pathological crystal growth inhibition. *Nature* **536,** 446–450 (2016).

113. Heijna, M. C. R., Enckevort, W. J. P. van & Vlieg, E. Growth Inhibition of Protein Crystals: A Study of Lysozyme Polymorphs. *Cryst. Growth Des.* **8,** 270–274 (2008).

114. Stone, M. P., Cho, Y.J., Huang, H., Kim, H.Y., Kozekov, I.D., Kozekova, A., Wang, H., Minko, I.G., Lloyd, R.S., Harris, T.M. & Rizzo, C.J. Interstrand DNA Cross-Links Induced by α,β-Unsaturated Aldehydes Derived from Lipid Peroxidation and Environmental Sources. *Acc. Chem. Res.* **41,** 793–804 (2008).

115. Choi, H. S., Liu, W., Misra, P., Tanaka, E., Zimmer, J.P., Itty, Ipe, B., Bawendi, M.G., Frangioni, J.V. Renal clearance of quantum dots. *Nat. Biotechnol.* **25,** 1165 (2007).

116. Jain, R. K. & Stylianopoulos, T. Delivering nanomedicine to solid tumors. *Nat. Rev. Clin. Oncol.* **7,** 653–664 (2010).

117. Lin, C., Perrault, S. D., Kwak, M., Graf, F. & Shih, W. M. Purification of DNA-origami nanostructures by rate-zonal centrifugation. *Nucleic Acids Res.* **41,** 40 (2013).